PROTOPLANETARY DISK DEMOGRAPHICS WITH ALMA

A DISSERTATION SUBMITTED TO THE GRADUATE DIVISION OF THE
UNIVERSITY OF HAWAIʻI AT MĀNOA IN PARTIAL FULFILLMENT OF THE
REQUIREMENTS FOR THE DEGREE OF

DOCTOR OF PHILOSOPHY

IN

ASTRONOMY

MAY 2017

By
Megan C. Ansdell

Dissertation Committee:

Jonathan Williams, Chairperson
Andrew Howard
Eric Gaidos
Shadia Habbal
Michael Liu
Gary Huss

Acknowledgements

Prior to this dissertation, I had never worked with Jonathan and had almost no experience with wavelengths longer than a few microns. Some would say that I took a gamble on this dissertation, and everyone would say that Jonathan took a gamble on me. Speaking only for myself, I do believe it turned out rather well. Jonathan brought me into the field of planet formation at a special time: ALMA is advancing our understanding of protoplanetary disks at an unprecedented pace, yet much remains to be learned, which keeps us on our toes. Jonathan also provided a balance of support, freedom, and challenge that has indisputably made me a better scientist; I cannot thank him enough for this.

I also thank those who were critical in keeping me afloat in my academic life during the past five years: the IfA secretaries and custodians, without whom the IfA would surely (and literally) crumble; Andrew Mann and Eric Gaidos, whose consistent guidance, encouragement, and patience has been fundamental in my progress as a scientist; Larissa Nofi and Kelly Blumenthal, who are both perpetual reminders of what strong women scientists look like; Zach Gazak, who taught me how to code in IDL, then promptly left astronomy just in time for IDL to fall out of fashion in favor of Python; Colin Aspin and John Rayner, whose support of students on Maunakea telescopes is so greatly appreciated; and especially my mother, who always listened to my academic highs and lows, even though she likely had no idea what I was talking about, and who kept me and the rest of the IfA very well fed.

Abstract

The recent successes of exoplanet surveys have resulted in thousands of planetary systems being discovered and characterized. Yet exactly how these planets formed remains unclear, as similar demographic surveys of the preceding protoplanetary disks were, until recently, hindered by the limited sensitivity and resolution of (sub-)mm telescopes. The revolutionary Atacama Large Millimeter/sub-millimeter Array (ALMA) has overcome these observational barriers, freeing observers from the need to focus on only the brightest disks, which likely do not represent the typical pathways to planet formation. This work leverages the power of ALMA to conduct the first large-scale, high-sensitivity surveys of (sub-)mm continuum and line emission for complete samples of protoplanetary disks at distinct stages of disk evolution. These observations are capable of placing statistical constraints on the evolution of fundamental disk properties, thereby providing new insights into how protoplanetary disks evolve into the observed exoplanet population. We focus on obtaining bulk disk masses in both dust and gas, as these fundamental properties are thought to strongly influence subsequent planetary architectures, yet remain poorly understood on a population level. We utilize a well-established method of translating (sub-)mm continuum flux into dust mass, and apply a recently developed technique for efficiently inferring gas mass from CO isotopologue line emission. Our ALMA surveys reveal a clear decline in disk dust mass with age, along with a potentially swifter decline in gas mass, both of which indicate that giant planet formation is either rare or rapid—the former being more consistent with exoplanet trends. We also find that in OB clusters external photoevaporation driven by the highest-mass stars enhances both dust and gas depletion much more severely than

previously thought. Our surveys illustrate the power of disk population studies in furthering our understanding of "typical" disk evolution and ultimately the most common pathways to planet formation.

Table of Contents

List of Tables

List of Figures

Chapter 1

Introduction

The recent successes of large-scale and long-term exoplanet surveys have opened the field of exoplanet statistics, revealing characteristic trends in the exoplanet population as well as diverse exoplanetary systems that often differ in striking ways from our own solar system. Yet exactly how these planets were formed has remained unclear due to our still incomplete understanding of the evolution of the proceeding protoplanetary disks. We know that protoplanetary disks disperse within $\sim$5–10 Myr, but uncovering exactly how fundamental disk properties change over this timescale—information that is critical to constraining planet formation theory—has been hindered by the limited resolution and sensitivity of (sub-)mm arrays. The recently commissioned Atacama Large Millimeter/sub-millimeter Array (ALMA) is overcoming these observational barriers, enabling large-scale disk surveys that are capable of revealing the "typical" evolutionary pathways from protoplanetary disks to exoplanet systems.

1.1 Motivation: Protoplanetary Disks to Exoplanet Systems

1.1.1 Protoplanetary Disks: Characteristics & Evolution

Circumstellar disks of gas and dust are ubiquitous around young stars, being natural consequences of collapsing molecular clouds conserving angular momentum while contracting roughly two orders of magnitude in size to form protostars. Circumstellar disks

evolve significantly over ∼5–10 Myr timescales, initially consisting of gas-rich material, but ending as dusty debris disks that presumably host newly formed planetary systems (see review in Williams & Cieza 2011). The evolutionary stage of a circumstellar disk can be identified by the slope of its spectral energy distribution (SED) at infrared (IR) wavelengths (Lada 1987; Lada et al. 2006). This is because thermal IR emission traces the existence and distribution of small (μm-sized) dust grains coupled to the gaseous disk.

Figure 1.1 provides a schematic view of this IR spectral index classification scheme. The first panel depicts Class 0 sources, which are highly embedded protostars surrounded by massive in-falling envelopes of circumstellar matter extending to ∼10^4 AU; Class 0 sources therefore emit strongly at (sub-)mm wavelengths, but lack both optical and IR emission in their SEDs. The second panel illustrates Class I sources, which are still optically obscured but now exhibit large IR excesses as strong outflows begin to clear their surrounding envelopes, resulting in the rising IR slope in their SEDs. These embedded Class 0/I phases are relatively short, with a combined median lifetime of just ∼0.5 Myr (Evans et al. 2009). Class II sources, shown in the third panel, are now optically visible pre-main sequence (PMS) stars that are no longer embedded and have essentially reached their final mass. The surrounding accretion disks contain only ∼0.01 $M_\odot$ of gas and dust spread over ∼100 AU, and are aptly referred to as "protoplanetary" disks, as they are believed to be the sites of ongoing planet formation. Class II sources are identified by the flat or declining IR slopes in their SEDs, characteristic of thermal emission from dust grains in circumstellar disks that are primarily heated by their central stars; some sources at this stage, known as "transition disks" (TDs), show mid-infrared dips in their SEDs due to clearings in their inner disk regions (e.g., due to planet formation, photoevaporation, or grain growth; see Espaillat et al. 2014 for a review). Class II sources represent the longest disk phase, with a median lifetime of several Myr (e.g., Mamajek 2009). Finally, the bottom panel depicts Class III sources that are at the end stages of disk evolution, marked by passive debris disks with little-to-no signs of accretion or excess emission at IR wavelengths. These sources presumably host newly formed planetary systems.

2
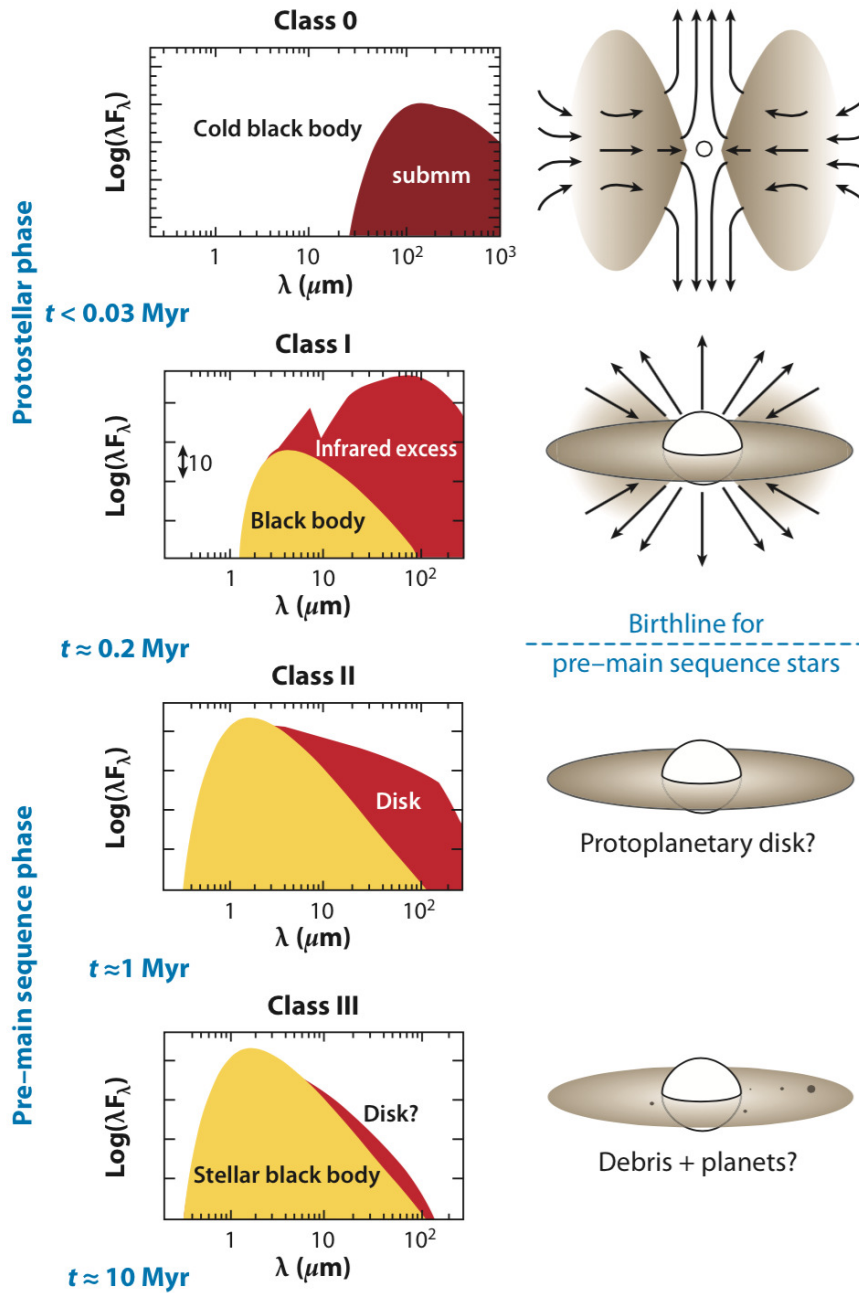
Figure 1.1 Schematic view of the commonly used IR-based disk classification scheme (taken from Dauphas & Chaussidon 2011). SEDs for each disk class are shown on the left, while corresponding illustrations of the disks are shown on the right. Embedded Class 0/I sources quickly evolve to optically visible pre-main sequence stars known as Class II sources, which are surrounded by so-called "protoplanetary" disks where planets are thought to assemble over several Myr. In the final stages of disk evolution, passive debris disks around Class III sources exhibit little-to-no excess at long wavelengths.

3

In this work, we focus on protoplanetary disks around Class II sources. Protoplanetary disks are cold (T $\sim$ 20 K) and compact (R $\sim$ 100 AU) objects that radiate predominately at IR and sub-mm wavelengths, making them difficult to observe from the ground. However, the development of space-based IR missions (e.g., *IRAS*, *Spitzer*, *Herschel*) enabled the first large-scale surveys of protoplanetary disks, revealing both their ubiquity around very young ($\lesssim$ 1 Myr) stars as well as their exponential decrease in occurrence over $\sim$5–10 Myr timescales. This is illustrated in Figure 1.2, which presents a version of the "Haisch-Lada" plot, named after the authors who first showed the declining fraction of disk-hosting sources in clusters as a function of age (Haisch et al. 2001; see also Hernández et al. 2007 and Mamajek 2009). In this version of the Haisch-Lada plot, only Class II sources identified via *Spitzer* IR excess are considered in order to reduce uncertainties from the application of different observational criteria. However, Figure 1.2 remains complicated by the usual caveats regarding absolute cluster age estimates (e.g., dependence on choice of model PMS evolutionary tracks; Hillenbrand et al. 2008) as well as the observed dependence of disk fraction on spectral type as a function of age (i.e., disks around late-type stars appear to survive longer than those around early-type stars; Hernández et al. 2009; Lada et al. 2006). Nevertheless, the rapid decline in disk occurrence with age is clear.

An exponential fit to the data in Figure 1.2 gives a very short characteristic (*e*-folding) disk lifetime of just $\sim$2.7 Myr, with $\sim$80% of stars losing their disks by $\sim$5 Myr. Our estimate of the characteristic disk lifetime is consistent with the $\sim$2.5 Myr value found in Mamajek (2009), who considered disks identified by *Spitzer* IR excess, *L*-band IR excess, or Hα emission (whereas Figure 1.2 only uses *Spitzer* IR excess, for reasons described above). This short disk dispersal timescale, combined with the prevalence of planet-hosting stars (see §1.1.3), implies very rapid planet growth. However, absolute cluster ages are highly uncertain and may be underestimated: Bell et al. (2013) found that a detailed treatment of PMS isochrone fitting results in cluster ages up to twice the typical ages adopted in the literature; using their revised ages and disk fractions based *Spitzer* IR excess, Bell et al. (2013) found that $\sim$80% of stars lose their disks by $\sim$10 Myr rather than $\sim$5 Myr.
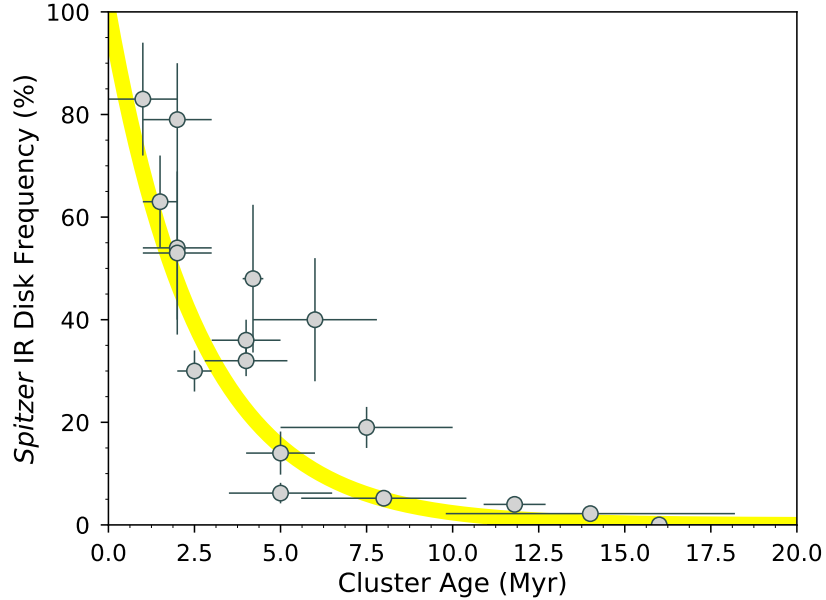
Figure 1.2 "Haisch-Lada" plot showing the fraction of cluster members hosting protoplanetary disks (identified by *Spitzer* IR excess) as a function of cluster age. Values are from the literature and a disk frequency of 100% is assumed at age zero. The best-fit exponential (yellow line) gives an *e*-folding disk lifetime of ∼2.7 Myr (where the *e*-folding time is the time interval over which an exponential function changes by a factor of *e*).

1.1.2   (sub-)mm Observations of Protoplanetary Disks

Disk lifetimes estimated from IR excess emission (§1.1.1; Figure 1.2) provide important constraints on the time available for planet formation. However, disk emission at wavelengths $\lesssim 100$ μm is generally optically thick, saturating at less than a lunar mass of dust spread over ∼100 AU. Moreover, IR emission is particularly sensitive to the temperature and density distribution of the circumstellar material, probing only the warmest and densest regions very close ($\lesssim 1$ AU) to the host star. This means that IR emission is an effective indicator of the *presence* of disks, but provides little information on the amount of material in disks and thus their *capacity* to form planets.

In contrast, (sub-)mm emission can be used as a proxy for the total amount of material in disks, and thus the capacity of disks to form planets. This is because 1) disk dust emission is optically thin in the (sub-)mm, as most dust grains are much smaller ($\ll \mu$m) than this
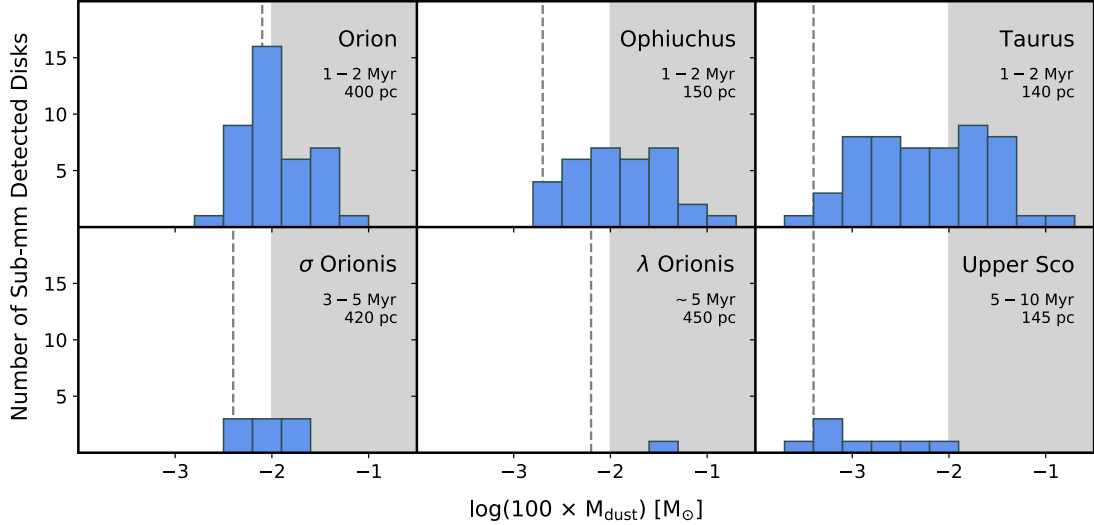
Figure 1.3 Mass distributions of protoplanetary disk populations at different ages and distances. Dust masses are taken from pre-ALMA (sub-)mm continuum surveys (Andrews & Williams 2007, 2005; Mann & Williams 2010; Mathews et al. 2012b; Williams et al. 2013; Ansdell et al. 2015) and scaled to total disk mass using the ISM gas-to-dust ratio, such that $M_{\mathrm{disk}} \approx 100\ M_{\mathrm{dust}}$. Dashed gray lines show survey completenesses and shaded regions highlight MMSN disks, which decrease by a factor of $\sim$20 over several Myr.

wavelength and 2) these longer wavelengths probe larger (μm- to cm-size) dust grains in the cooler/outer regions of the disk, which contain the bulk of the dust mass (Wyatt & Dent 2002; Draine 2006). Consequently, (sub-)mm continuum flux can be directly related to the total mass of the emitting dust, as described in Hildebrand (1983) (see §2.1.1 for details). To obtain the total disk mass (gas + dust), the interstellar medium (ISM) gas-to-dust ratio of $\sim$100 (Bohlin et al. 1978) is typically used, such that $M_{\mathrm{disk}} \approx 100\ M_{\mathrm{dust}}$. These disk masses are often compared to the minimum mass solar nebula (MMSN), which is an estimate of the least massive primordial disk that could have formed the solar system ($\sim 0.01 M_\odot$ or $\sim 10 M_{\mathrm{Jup}}$), assuming cosmic abundances. The pioneering study by Beckwith et al. (1990) found that disks in the Taurus star-forming region have masses greater than the MMSN on average, an early observational indication that exoplanet systems are common.

Pre-ALMA studies expanded upon this initial work by conducting larger and more sensitive (sub-)mm continuum surveys of star-forming regions at different ages, using facilities such as the SMA, JCMT, and IRAM (Andrews & Williams 2005; Williams et al.

2005; Andrews & Williams 2007; Mann & Williams 2009, 2010; Lee et al. 2011; Mathews et al. 2012a; Williams et al. 2013; Mann et al. 2014; Ansdell et al. 2015). As shown in Figure 1.3, these studies confirmed that many young ($\sim$1–2 Myr) disks are more massive than the MMSN, but also that disk masses decrease rapidly, with very few MMSN disks remaining after several Myr. This apparent depletion of disk mass reflects disk dispersal as well as the growth of dust grains to sizes larger than a few cm, at which point solids no longer efficiently emit at (sub-)mm wavelengths (Draine 2006). This interpretation is supported by the observed flattening of the (sub-)mm spectral index in young disks when compared to the ISM, which points to significant grain growth occurring over just a few Myr (e.g., Andrews & Williams 2005). It is also consistent with the ages of chondrules found inside meteorites, which indicate that the first $\sim$mm-sized solids in our solar system formed on similar timescales (e.g., Connelly et al. 2008). However, as illustrated by the bottom panels of Figure 1.3, stronger constraints on disk dissipation timescales will require more sensitive measurements that are capable of probing the fainter disks in older and/or more distant star-forming regions. Pre-ALMA facilities lacked the sensitivity to obtain these measurements for large samples of disks within reasonable integration times.

The major caveat to the disk masses shown in Figure 1.3 is that they are extrapolated from the dust masses using the ISM gas-to-dust ratio of $\sim$100. Extrapolating total disk mass from dust mass has been a standard practice, as converting line emission to gas mass is complicated by disk chemistry and optical depth effects (see §2.1.2). Yet this extrapolation of two orders of magnitude is not only large, but also highly uncertain: although disks are thought to form with an inherited ISM gas-to-dust ratio of $\sim$100, they rapidly evolve to the opposite extreme of dusty debris disks with negligible gas on timescales of $\sim$5–10 Myr via processes that are not yet fully understood (§1.1.1). Indeed, using a recently developed technique to independently measure gas masses from CO isotopologue emission, Williams & Best (2014) found that the gas-to-dust ratios of nine protoplanetary disks in the young ($\sim$1–2 Myr) Taurus star-forming region may be significantly lower than in the ISM, while also varying substantially from disk to disk. This suggests that disk masses are over-estimated

when assuming $M_{\mathrm{disk}} \approx 100\ M_{\mathrm{dust}}$, a result that would have significant implications for predicted planet formation timescales. Their results also indicate the need for more CO isotopologue observations in order to better understand disk gas masses and gas-to-dust ratios on a population level. However CO isotopologue emission is typically faint (due to the rarity of the molecules) and thus pre-ALMA surveys struggled to detect these lines in all but the brightest disks.

1.1.3   The Exoplanet Population: Diversity, Trends, Challenges

Large-scale and long-term exoplanet surveys, such as the Eta-Earth radial velocity survey (Howard et al. 2010) and the *Kepler* transit survey (Borucki et al. 2010), have now discovered and characterized hundreds of exoplanet systems. The exoplanet population appears to show a wide diversity in planet sizes, compositions, and orbital architectures (e.g., Winn & Fabrycky 2015) that often differ in striking ways from what is seen in our own solar system. In particular, intermediate-mass planets—commonly known as "super-Earths" and "mini-Neptunes"—are missing from our solar system, yet appear to be the most common planet type in the nearby galaxy, at least for the short orbital periods ($\sim$50–100 days) that have been probed by state-of-the-art exoplanet population studies (Howard et al. 2012; Fressin et al. 2013; Petigura et al. 2013; Gaidos et al. 2016). Moreover, these intermediate-mass planets may have a range of compositions, from those made of pure rock to those hosting substantial volatile-rich envelopes (e.g., Sinukoff et al. 2016).

These observational findings from exoplanet surveys have challenged traditional planet formation theories, which predicted a "planetary desert" in the intermediate-mass range (Ida & Lin 2004). This is because core accretion models dictate that $\sim$10 $M_{\oplus}$ planet cores should have sufficient gravity to rapidly accrete gaseous envelopes, reaching masses of $\sim$1 M_{Jup} within $\sim$0.1 Myr, if gas is still present in the disk (e.g., Pollack et al. 1996). In other words, anything large enough to be a super-Earth or mini-Neptune should become a gas giant. The unexpected propensity and diversity of intermediate-mass planets could be explained by variations in protoplanetary disk properties—in particular the amount of

disk material, its physical state as solid or gas, and the timescale over which the material is available—having significant influences on the assembly of planetary systems.

Exoplanet surveys have also enabled statistical characterizations of the exoplanet population, resulting in the identification of several correlations with host-star properties (at least for the roughly year-long orbital periods currently probed by exoplanet surveys). In particular, clear positive correlations exist between giant planet frequency and host-star mass (e.g., Endl et al. 2006; Johnson et al. 2010; Bowler et al. 2010) as well as between giant planet frequency and host-star metallicity (e.g., Fischer & Valenti 2005; Johnson et al. 2010). Several studies have also found that Earth-sized planets are several times more common around low-mass M dwarf stars than around solar-type stars (e.g., Howard et al. 2012; Dressing & Charbonneau 2013; Mulders et al. 2015).

These exoplanet trends likely result from disk properties that also scale with host-star properties. Indeed, planet formation models find that disk mass and metallicity dictate the frequency and location of the formation of different planet types: namely, higher-metallicity disks result in higher frequencies of giant planets, and higher-mass disks result in more massive giant planets (e.g., Mordasini et al. 2012). Additionally, a scaling of protoplanetary disk mass with host-star mass, which has been observed in pre-ALMA disk surveys of the Taurus star-forming region (Natta et al. 2000; Andrews et al. 2013), has been used to explain the paucity of high-mass planets around low-mass stars (e.g., Alibert et al. 2011).

Evidently, characterizing the statistical properties of protoplanetary disks, in a manner similar to what has been achieved for exoplanets, is critical for understanding planet formation. Exoplanet population synthesis models require inputs of initial disk properties (e.g., total mass, metallicity, surface density), then apply prescriptions for their evolution (e.g., core accretion) to explain observed exoplanet systems. The outcomes of these population synthesis models are known to depend sensitively on the assumed initial disk conditions (see Bitsch et al. 2015, and references therein), which remain largely unconstrained by observations on a population level. This is because disks are faint and compact objects, requiring high-sensitivity and high-resolution observations to measure

their fundamental properties, which until recently were observationally prohibitive for large samples. By necessity, pre-ALMA studies focused on the brightest disks, which likely do not represent average disk conditions and thus typical pathways to planet formation. Directly relating protoplanetary disks to exoplanet systems will require large-scale, high-sensitivity (sub-)mm surveys that can probe disk evolution in both dust and gas, independently. These observations will enable direct measurements of fundamental disk properties and provide constraints on disk dispersal pathways, which can then serve as reliable inputs into planet formation and exoplanet population synthesis models.

1.2   Dissertation Outline

The goal of this dissertation is to provide statistical constraints on the evolution of fundamental disk properties in order to better understand how protoplanetary disks evolve into the observed exoplanet population. We focus on measuring bulk dust and gas masses, as these properties are thought to largely dictate what types of planets can form in a given disk. Moreover, these properties can now be efficiently measured for large samples of protoplanetary disks using ALMA, which provides order-of-magnitude greater sensitivity and resolution over previous (sub-)mm arrays.

We begin in Chapter 2 by describing our methods for deriving the bulk dust and gas masses of protoplanetary disks. Dust masses are derived from optically thin (sub-)mm continuum flux using a well-established linear relation (Hildebrand 1983), while gas masses are estimated by applying a novel approach that utilizes CO isotopologue flux (Williams & Best 2014). We then present our ALMA surveys of the protoplanetary disk populations in two star-forming regions with distinct ages, Lupus and σ Orionis, and apply our methods for deriving bulk dust and gas masses to each disk.

In Chapter 3, we use our surveys to characterize fundamental disk properties on a population level and study how they change with age. We see a clear decline in disk dust mass with age, along with a potentially swifter decline in disk gas mass; consequently, gas-

to-dust ratios are typically much smaller than the ISM value traditionally assumed in disk studies. However, we discuss the possibility that our gas masses are under-estimated due to additional volatile carbon depletion mechanisms that are not yet well understood. We also find that in OB clusters external photoevaporation driven by high-mass stars further depletes dust and especially gas at much higher rates than previously thought.

The implications for planet formation are discussed in Chapter 4: overall, our findings indicate that giant planet formation is either rare or rapid—the former being more consistent with exoplanet trends. We also show how our ALMA surveys have been combined with other datasets to test theories of viscous disk evolution as well as study the relation between the inner and outer disk regions. Finally, we conclude with an overview of the presented work and discuss prospects for future research.

Chapter 2

Analysis Methods & ALMA Survey Results

Characterizing the evolution of dust and gas in protoplanetary disks is critical to understanding planet formation. In this dissertation, we focus on bulk dust and gas masses, as these are fundamental disk properties that largely dictate the types of planets that can form in a given disk. Although there are well-established methods for measuring dust masses, techniques for estimating gas masses are in ongoing development and often require exceptional datasets and detailed modeling. In this chapter, we calculate dust masses from (sub-)mm continuum flux using a standard linear relation (Hildebrand 1983), then estimate gas masses from CO isotopologue emission using a recently developed technique by Williams & Best (2014). These methods are chosen for their efficiency, which enables their application to entire populations of protoplanetary disks in star-forming regions with ages spanning the disk lifetime ($\sim$1–10 Myr). We employ these methods in our ALMA surveys of two star-forming regions at distinct stages of disk evolution: Lupus and σ Orionis. Lupus is a young ($\sim$1–3 Myr) and nearby (150–200 pc) star-forming region containing 93 protoplanetary disks, while σ Orionis is an intermediate-aged ($\sim$3–5 Myr) and more distant (385 pc) OB cluster hosting 92 protoplanetary disks. We also use from the literature the (sub-)mm continuum surveys of several other star-forming regions (Taurus, Chamaeleon I, and Upper Sco) in order to expand our understanding of bulk disk dust evolution. This work represents the largest demographic study to date on the evolution of bulk dust and gas content in protoplanetary disks.

2.1 Analysis Methods: Deriving Bulk Disk Properties

2.1.1 Dust Masses from (Sub)-mm Continuum Emission

(Sub-)mm continuum emission from protoplanetary disks is generally optically thin. This is because the dust extinction experienced at a given wavelength of light (λ) is dominated by grains with sizes $a \approx \lambda/3$ (Draine 2011) and most dust grains in protoplanetary disks are sub-μm in size (Mathis et al. 1977); hence disk emission is optically thick at IR wavelengths, but generally optically thin at longer wavelengths. Additionally, (sub-)mm continuum emission from protoplanetary disks primarily traces dust grains with (sub-)mm to cm sizes, as the thermal emission from dust grains peaks at wavelengths similar to their size (Wyatt & Dent 2002). Although these larger solids constitute the tail end of the grain size distribution in protoplanetary disks, they still contain the vast majority of the dust mass (Mathis et al. 1977). Consequently, the (sub-)mm continuum flux of a protoplanetary disk can be directly related to its bulk dust mass (M_{dust}), as derived in Hildebrand (1983):

$$M_{\mathrm{dust}} = \frac{F_\nu d^2}{\kappa_\nu B_\nu(T_{\mathrm{disk}})} \tag{2.1}$$

where F_ν is the (sub-)mm continuum flux density, d is the source distance, $B_\nu(T_{\mathrm{disk}})$ is the Planck function for a characteristic dust temperature of T_{dust}, and κ_ν is the dust grain opacity. We take κ_ν as $10 \ \mathrm{cm^2 \ g^{-1}}$ at 1000 GHz and use an opacity power-law index of $\beta = 1$, such that $\kappa_\nu = 10(\nu/1000\mathrm{GHz})\mathrm{cm^2 g^{-1}}$ (Beckwith et al. 1990). We assume an isothermal disk where $T_{\mathrm{disk}} = 20$ K (the median for Taurus disks; Andrews & Williams 2005).

This approach has been applied in numerous disk studies to estimate dust mass, and is particularly useful for large surveys due to its efficiency (e.g., Williams et al. 2013; Andrews & Williams 2005; Mathews et al. 2012b; Barenfeld et al. 2016; Pascucci et al. 2016). Indeed, for a given population of protoplanetary disks, only the observed F_ν of each source must be changed in Equation 2.1, as all other factors can be assumed constant for a uniform survey. For these reasons, we adopt this method for deriving disk dust masses in this work.

We note that some disk studies apply a weak scaling of T_{dust} to the stellar luminosity ($L_\star$) using the relation $T_{\mathrm{dust}} = 25\mathrm{K} \times (L_\star/L_\odot)^{0.25}$. This is because the outer disk regions generating most of the (sub-)mm continuum flux are heated solely by irradiation from the central star, resulting in the above dependence of T_{dust} on $L_\star$ for a purely optically thin case. Andrews et al. (2013) used two-dimensional continuum radiative transfer models to validate this scaling; however, more detailed modeling of resolved disks has recently shown that T_{dust} is independent of stellar parameters (Tazzari et al. 2017), which is likely due to variations in other key disk parameters (e.g., scale height) nullifying any weak dependence of T_{dust} on $L_\star$. Consequently, adopting the above scaling may actually introduce biases in the derived dust masses. Moreover, any plausible variations in T_{disk} are dominated by uncertainties in κ_ν, which can be up to a factor of three due to our lack of constraints on dust grain sizes and compositions. Disk surveys also apply different methods for deriving stellar parameters, with varying levels of confidence (e.g., photometrically derived stellar parameters are less reliable than those derived from spectra), thus scaling T_{dust} to $L_\star$ can complicate comparisons of disk dust mass distributions between star-forming regions.

2.1.2 Gas Masses from CO Isotopologue Emission

Measuring the gas content in protoplanetary disks is essential for a complete understanding of planet formation (§1.1.3). But estimating bulk gas mass (M_{gas}) from line emission is complicated by the complex chemistry and radiative transfer occurring in disks; current techniques often require exceptional datasets (e.g., high-resolution spectra at high signal-to-noise) coupled with detailed modeling, both of which are prohibitive for typical disks and especially for large surveys. The ISM gas-to-dust ratio of $\sim$100 is therefore commonly used to infer gas masses from the measured dust masses, yet this inherited ISM value must evolve significantly as protoplanetary disks mature into dusty debris disks and eventually planetary systems (§1.1). This motivates the development of more efficient techniques for estimating bulk gas masses of protoplanetary disks.

Ideally, the dominant species in disks, H_2, would be used to measure gas masses. However, disks are too cold ($T_{gas} < 200$ K) for efficient collisional excitation of H_2 due to the symmetry of the molecule, resulting in weak and often undetectable emission (e.g., Carmona et al. 2008). HD is the closest chemical species to H_2 and follows the same spatial distribution, but it only emits at far-IR wavelengths and thus cannot be observed from the ground. Before *Herschel* was decommissioned, this space-based observatory was used to measure HD in three exceptionally bright and nearby disks (TW Hydrae, DM Tau, GM Aur; Bergin et al. 2013; McClure et al. 2016). Unfortunately, all other disks are too faint for similar observations with the *SOFIA* airborne observatory; without another far-IR mission in operation, additional gas mass measurements via HD are not currently possible.

The best alternative is to use molecular tracers of total gas mass. These tracers are asymmetric molecules with non-zero dipole moments, which provide low energy levels that can be excited even at the cool temperatures found in disks. CO is typically used because it is the most abundant molecule after H_2, forming quickly in the gas phase and using up the vast majority of available carbon (van Dishoeck & Black 1988). It also has the strongest rotational lines at (sub-)mm wavelengths, making it relatively easy to observe from the ground. Gas-phase CO has two main destruction mechanisms: freeze-out onto dust grains near the disk mid-plane due to low temperatures ($T_{gas} < 20$ K; e.g., Jørgensen et al. 2002) and photodissociation by stellar UV irradiation in the upper-most disk layers due to low column densities ($N_{H_2} < 1.3 \times 10^{21}$ cm^2; e.g., Visser et al. 2009). Physical-chemical models of protoplanetary disks have shown that a significant fraction of CO is sufficiently warm to avoid freeze-out and also sufficiently shielded from UV irradiation to avoid photodissociation (Aikawa et al. 2002); thus the surviving CO gas fraction is expected to be large, except for exceptionally cold or low-mass disks (Williams & Best 2014). However, CO rotational lines at (sub-)mm wavelengths are optically thick, tracing the surface temperature profile of the disk rather than the bulk gas mass. Fortunately, the emission lines of the less-abundant CO isotopologues can avoid saturation, making them useful for inferring bulk gas mass, as with their application to molecular clouds/cores (Goldsmith et al. 1997).
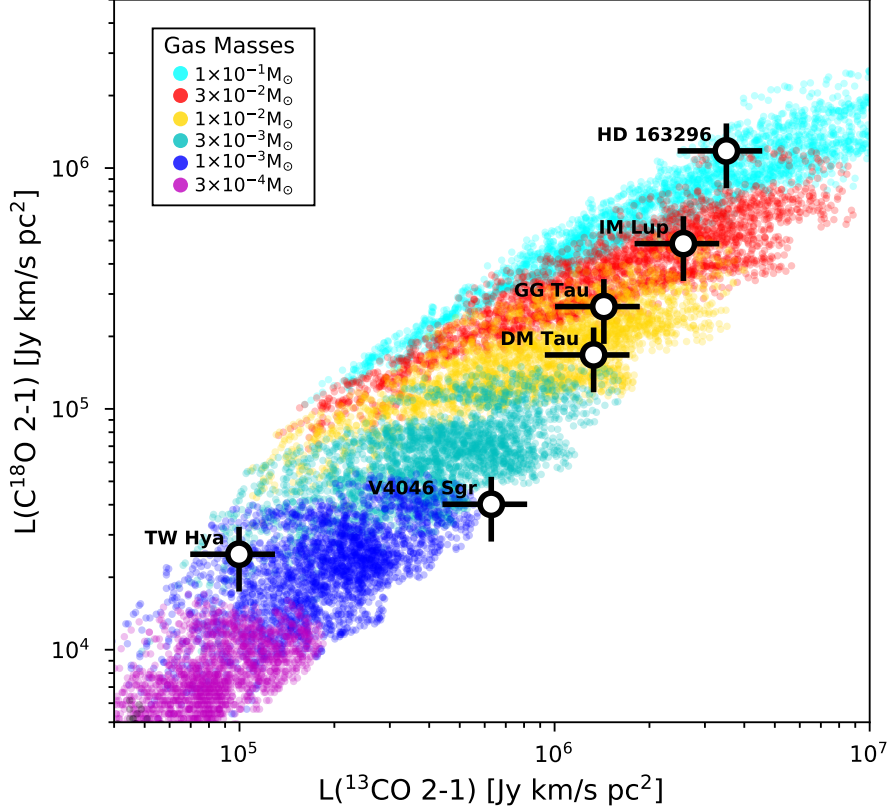
Figure 2.1 Modeled ^{13}CO and C^{18}O integrated line luminosities from the WB14 grid, color coded by disk gas mass. Observations for several well-characterized disks are shown to illustrate how the combination of the two lines can be used to estimate total gas mass to within a factor of three given typical ($\sim$10%) measurement uncertainties.

Williams & Best (2014) (hereafter WB14) developed a novel technique to relate CO isotopologue line luminosities to disk gas masses, using only a parametric disk model, simple assumptions of CO chemistry (i.e., freeze-out and photodissociation), and the radiative transfer code RADMC-3D.[1] This technique requires measurements of just two CO isotopologue lines, ^{13}CO and C^{18}O, to infer bulk gas masses to within factors of 3–10 of estimates by more detailed chemical modeling. It is therefore the best available method for efficiently estimating disk gas masses independently from the dust, and also provides sufficient accuracy for statistical studies of large samples of protoplanetary disks. Figure 2.1 shows the full WB14 model grid as a function of total gas mass, illustrating how we can

---

[1]http://www.ita.uni-heidelberg.de/ dullemond/software/radmc-3d/

simply over-plot our measurements of ^{13}CO and C^{18}O in order to obtain rough estimates of the disk gas mass. The spread in the model grid for a given gas mass is due to other disk parameters (e.g., vertical disk structure) affecting line emission strengths; thus these often unconstrained parameters are accounted for in the range of possible gas masses consistent with a given set of line measurements.

In the following sections, we introduce two star-forming regions, present our ALMA surveys of their disk populations, and measure disk dust and gas masses using the analysis techniques described above.

2.2 Lupus: Baseline Study of Early Disk Conditions

2.2.1 Overview

The Lupus complex is an ideal target for a baseline study of early disk conditions: it is one of the youngest and closest star-forming regions, and hosts a well-characterized population of several hundred young stellar objects (YSOs) (see review in Comerón 2008). Lupus is part of the larger Scorpius-Centaurus association and contains four main star-forming clouds (Lupus I, II, III, IV) with mass functions that are dominated by low-mass (M-type) stars, when compared to the similarly aged Taurus region (Hughes et al. 1994). The distances to the Lupus clouds likely vary due to the depth of the complex: Lupus I, II, and IV are estimated to be at 150 pc, while Lupus III is slightly more distant at 200 pc. The average age of the complex has been estimated at $\sim$1–3 Myrs based on the position of YSOs above the main sequence (Comerón et al. 2003; Alcalá et al. 2014), although these values rely on model isochrones and depend heavily on distance uncertainties.

The Lupus clouds have been studied across the spectrum of wavelengths, resulting in well-defined SEDs for most cluster members. The clouds have been targeted by mid-IR *Spitzer* IRAC/MIPS (3.6–160 μm; Merín et al. 2008) and far-IR *Herschel* (70–500 μm; Rygl et al. 2013) surveys, while also being covered by all-sky optical ($UVBRI$) and near-IR (2MASS JHK_{S}) surveys. These observations revealed high protoplanetary disk fractions

17

in the Lupus I, III, and IV clouds (70–80%; Merín et al. 2008), a clear indication of their youth (see Figure 1.2). Although Lupus II was not targeted by *Spitzer* or *Herschel*, it is a recognized active star-forming region (Schwartz 1977) and contains RU Lup, one of the most active known T Tauri stars.

The majority of disk-hosting YSOs in Lupus are extremely well characterized thanks to the analysis of VLT/X-Shooter spectra by Alcalá et al. (2014) and Alcalá et al. (2017). The broad wavelength coverage of the VLT/X-Shooter spectrograph ($\lambda \sim 330$–2500 nm), combined with its medium spectral resolution ($R \sim 2000$–18000), enables precise constraints on stellar properties (T_{eff}, $M_\star$, $L_\star$), optical extinction (A_{V}), and stellar mass accretion rate ($\dot{M}_{\mathrm{acc}}$). The addition of VLT/X-Shooter data makes Lupus an especially valuable target for studying young star-disk systems.

2.2.2 Sample Selection

Our sample consists of the 93 YSOs in Lupus I–IV with masses above the brown-dwarf limit (≥ 0.1 $M_\odot$) and IR excesses consistent with the presence of protoplanetary disks. These sources are identified in published Lupus disk catalogues (Hughes et al. 1994; Merín et al. 2008; Comerón 2008; Mortier et al. 2011; Dunham et al. 2015; Bustamante et al. 2015) as Class II, TD, or flat-spectrum objects. Disk classifications were primarily derived from the IR spectral index slope (§1.1.1) measured between the 2MASS K_{S} (2 μm) and *Spitzer*/MIPS-1 (24 μm) bands (Merín et al. 2008). For the five Lupus II sources (Sz 79, Sz 81A, IM Lup, Sz 83, Sz 84), which do not have *Spitzer* data, disk classifications were approximated from accretion signatures (e.g., Hα emission; Hughes et al. 1994). To estimate the preliminary stellar masses used for our $M_\star \geq 0.1$ $M_\odot$ cutoff, we fit absolute 2MASS J-band magnitudes, which are relatively unaffected by disk excess emission, to the 3 Myr model isochrone from Siess et al. (2000). Note that we do not include RXJ1556.1-3655 and RXJ1615.3-3255 in our sample, despite them being listed as Class II Lupus disks in the literature (Wahhaj et al. 2010; Andrews et al. 2011), as their coordinates are off the Lupus I–IV clouds (e.g., Cambrésy 1999).
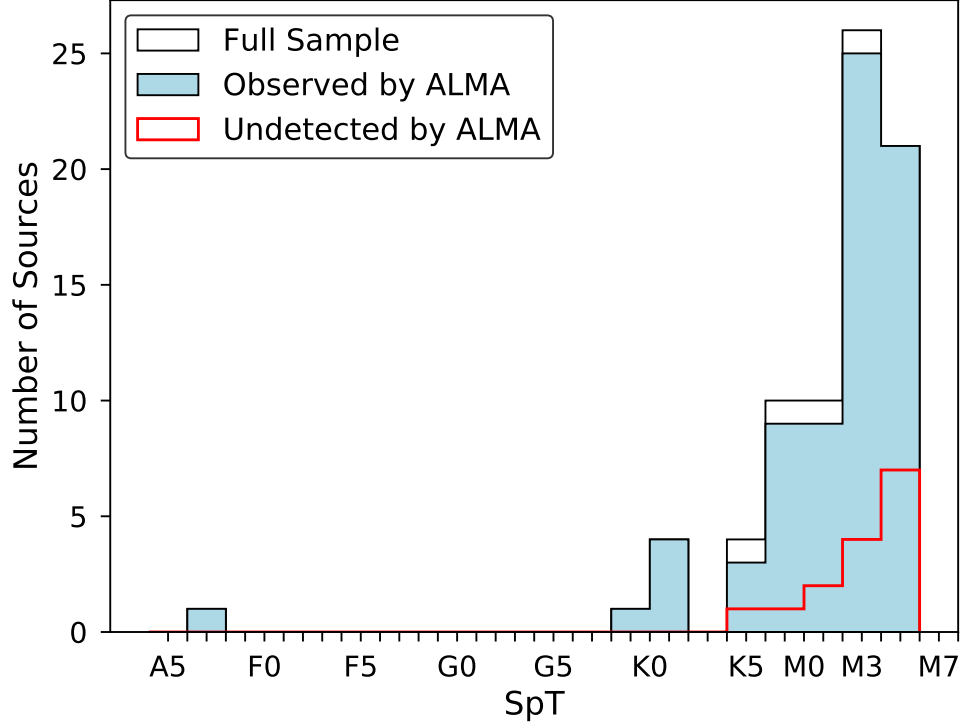
Figure 2.2 Distribution of stellar spectral types (SpT) in our Lupus sample (Table 2.1). The blue histogram shows the sources in our sample with ALMA observations, the open histogram includes the four objects for which we did not obtain ALMA observations (§2.2.3), and the red histogram shows the sources undetected in the ALMA continuum (§2.2.4).

Table 2.1 presents the 93 sources in our sample with some basic stellar and disk properties. Source distances (d) are based on cloud membership (§2.2.1) and stellar spectral types (SpT) and masses ($M_\star$) are from the literature (see Table 2.1 for references). Figure 2.2 shows the SpT distribution of our sample. The 73 $M_\star$ values in Table 2.1 (except for V856 Sco) are derived by obtaining accurate measurements of T_{eff} and $L_\star$ from VLT/X-Shooter spectra, then comparing these values to the stellar evolutionary models of Siess et al. (2000); the median $M_\star$ uncertainty is ~16%. For details on the derivation of these $M_\star$ values, as well as their associated T_{eff} and $L_\star$ values, see Alcalá et al. (2014) and Alcalá et al. (2017). The 20 sources without $M_\star$ estimates are the more obscured flat-spectrum sources or exceptionally faint sources, for which it is not possible to derive accurate stellar properties, thus we do not provide them in Table 2.1.

19

Table 2.1: Lupus Sample Properties

ID	d	Disk	SpT	$M_\star(M_\odot)$	Reference
Sz 65	150	II	K7.0	0.76 ± 0.18	Alcalá et al. (2017)
Sz 66	150	II	M3.0	0.31 ± 0.04	Alcalá et al. (2014)
J15430131-3409153	150	F			
J15430227-3444059	150	F			
J15445789-3423392	150	II	M5.0	0.12 ± 0.03	Alcalá et al. (2014)
J15450634-3417378	150	F			
J15450887-3417333	150	II	M5.5	0.14 ± 0.03	Alcalá et al. (2017)
Sz 68	150	II	K2.0	2.13 ± 0.34	Alcalá et al. (2017)
Sz 69	150	II	M4.5	0.19 ± 0.03	Alcalá et al. (2014)
Sz 71	150	II	M1.5	0.42 ± 0.11	Alcalá et al. (2014)
Sz 72	150	II	M2.0	0.38 ± 0.09	Alcalá et al. (2014)
Sz 73	150	II	K7.0	0.82 ± 0.16	Alcalá et al. (2014)
Sz 74	150	II	M3.5	0.29 ± 0.03	Alcalá et al. (2014)
Sz 76	150	TD	M4.0	0.25 ± 0.03	Alcalá et al. (2017)
Sz 77	150	II	K7.0	0.79 ± 0.17	Alcalá et al. (2017)
Sz 81A	150	II	M4.5	0.23 ± 0.03	Alcalá et al. (2017)
IM Lup	150	II	K5.0	1.10 ± 0.00	Alcalá et al. (2017)
Sz 83	150	II	K7.0	0.75 ± 0.19	Alcalá et al. (2014)
Sz 84	150	TD	M5.0	0.18 ± 0.03	Alcalá et al. (2014)
Sz 129	150	II	K7.0	0.80 ± 0.15	Alcalá et al. (2017)
J15592523-4235066	150	II	M5.0	0.12 ± 0.03	Alcalá et al. (2017)
RY Lup	150	II	K2.0	1.47 ± 0.22	Alcalá et al. (2017)
J16000060-4221567	150	II	M4.5	0.19 ± 0.03	Alcalá et al. (2017)
J16000236-4222145	150	II	M4.0	0.24 ± 0.03	Alcalá et al. (2017)
J16002612-4153553	150	II	M5.5	0.14 ± 0.03	Alcalá et al. (2017)
Sz 130	150	II	M2.0	0.37 ± 0.10	Alcalá et al. (2014)
MY Lup	150	TD	K0.0	1.02 ± 0.13	Alcalá et al. (2017)
Sz 131	150	II	M3.0	0.30 ± 0.04	Alcalá et al. (2017)
J16011549-4152351	150	F/TD			
Sz 133	150	II	K2.0	0.63 ± 0.05	Alcalá et al. (2017)
Sz 88A	200	II	M0.0	0.57 ± 0.15	Alcalá et al. (2014)
Sz 88B	200	II	M4.5	0.20 ± 0.03	Alcalá et al. (2014)
J16070384-3911113	200	F	M4.5	0.17 ± 0.03	Alcalá et al. (2017)
J16070854-3914075	200	F			
Sz 90	200	II	K7.0	0.79 ± 0.18	Alcalá et al. (2017)
Sz 91	200	TD	M1.0	0.47 ± 0.12	Alcalá et al. (2017)
J16073773-3921388	200	II	M5.5	0.11 ± 0.02	Alcalá et al. (2014)
Sz 95	200	II	M3.0	0.33 ± 0.03	Alcalá et al. (2017)
J16075475-3915446	200	F			
J16080017-3902595	200	II	M5.5	0.13 ± 0.02	Alcalá et al. (2014)
J16080175-3912316	200	II	K6.0		Merín et al. (2008)
Sz 96	200	II	M1.0	0.46 ± 0.11	Alcalá et al. (2017)
J16081497-3857145	200	TD	M5.5	0.10 ± 0.02	Alcalá et al. (2017)
Sz 97	200	II	M4.0	0.25 ± 0.03	Alcalá et al. (2014)
Sz 98	200	II	K7.0	0.74 ± 0.20	Alcalá et al. (2017)
Sz 99	200	II	M4.0	0.22 ± 0.03	Alcalá et al. (2014)
Sz 100	200	II	M5.5	0.18 ± 0.03	Alcalá et al. (2014)

J160828.1-391310	200	II	M6.5	0.10 ± 0.01	Alcalá et al. (2017)
Sz 103	200	II	M4.0	0.25 ± 0.03	Alcalá et al. (2014)
J16083070-3828268	200	TD	K2.0	1.81 ± 0.28	Alcalá et al. (2017)
Sz 104	200	II	M5.0	0.18 ± 0.03	Alcalá et al. (2014)
J160831.1-385600	200	F			
V856 Sco	200	II	A7.0	2.84 ± 0.29	Alecian et al. (2013)
V1094 Sco	200	II	K6.0	0.47 ± 0.14	Alcalá et al. (2017)
Sz 106	200	II	M0.5	0.51 ± 0.10	Alcalá et al. (2014)
Sz 108B	200	II	M5.0	0.19 ± 0.03	Alcalá et al. (2017)
J16084940-3905393	200	II	M4.0	0.26 ± 0.03	Alcalá et al. (2014)
V1192 Sco	200	II	M4.5	0.16 ± 0.02	Alcalá et al. (2014)
Sz 110	200	II	M4.0	0.26 ± 0.03	Alcalá et al. (2014)
J16085324-3914401	200	II	M3.0	0.32 ± 0.04	Alcalá et al. (2017)
J16085373-3914367	200	II	M5.5	0.10 ± 0.02	Alcalá et al. (2017)
Sz 111	200	TD	M1.0	0.46 ± 0.12	Alcalá et al. (2014)
J16085529-3848481	200	II	M6.5	0.10 ± 0.02	Alcalá et al. (2017)
Sz 112	200	TD	M5.0	0.20 ± 0.03	Alcalá et al. (2014)
Sz 113	200	II	M4.5	0.19 ± 0.03	Alcalá et al. (2014)
J16085828-3907355	200	II			
J16085834-3907491	200	II			
J16090141-3925119	200	II	M4.0	0.24 ± 0.03	Alcalá et al. (2014)
Sz 114	200	II	M4.8	0.23 ± 0.03	Alcalá et al. (2014)
Sz 115	200	II	M4.5	0.22 ± 0.03	Alcalá et al. (2014)
J16091644-3904438	200	II			
J16092032-3904015	200	II			
J16092317-3904074	200	II			
J16092697-3836269	200	II	M4.5	0.20 ± 0.03	Alcalá et al. (2017)
J160934.2-391513	200	F			
J16093928-3904316	200	II			
Sz 117	200	II	M3.5	0.29 ± 0.03	Alcalá et al. (2017)
Sz 118	200	II	K5.0	1.09 ± 0.20	Alcalá et al. (2017)
J16095628-3859518	200	II	M6.0	0.10 ± 0.01	Alcalá et al. (2014)
J16100133-3906449	200	II	M6.5	0.14 ± 0.03	Alcalá et al. (2017)
J16101307-3846165	200	F	M4.0		Mortier et al. (2011)
J16101857-3836125	200	II	M5.0	0.15 ± 0.03	Alcalá et al. (2017)
J16101984-3836065	200	II	M5.5	0.10 ± 0.02	Alcalá et al. (2017)
J16102741-3902299	200	F			
J16102955-3922144	200	TD	M4.5	0.22 ± 0.03	Alcalá et al. (2017)
J16104536-3854547	200	II	K9.0		Merín et al. (2008)
Sz 123B	200	II	M2.0	0.34 ± 0.09	Alcalá et al. (2014)
Sz 123A	200	TD	M1.0	0.46 ± 0.11	Alcalá et al. (2014)
J16115979-3823383	200	II	M5.0	0.15 ± 0.03	Alcalá et al. (2014)
J16120445-3809589	200	F			
J16121120-3832197	200	II	K7.0		Merín et al. (2008)
J16124373-3815031	200	II	M1.0	0.47 ± 0.12	Alcalá et al. (2017)
J16134410-3736462	200	II	M5.0	0.16 ± 0.03	Alcalá et al. (2017)

2.2.3 ALMA Observations

Our ALMA Cycle 2 observations (Project ID: 2013.1.00220.S; PI: Williams) of the sources in our Lupus sample were obtained in Band 7 on 2015 June 14 (AGK-type and unknown SpT sources) and 2015 June 15 (M-type sources). The continuum spectral windows were centered on 328.3, 340.0, and 341.8 GHz with bandwidths of 1.875, 0.938, and 1.875 GHz and channel widths of 15.625, 0.244, and 0.977 MHz, respectively. The bandwidth-weighted mean continuum frequency is 335.8 GHz (890 μm). The spectral setup included two windows covering the ^{13}CO and C^{18}O $J = 3$–2 transitions; these spectral windows were centered on 330.6 and 329.3 GHz, respectively, with bandwidths of 58.594 MHz, channel widths of 0.122 MHz, and velocity resolutions of 0.11 km s^{-1}.

The array configuration used 37 12-m antennas for the M-type sub-sample and 41 12-m antennas for the AGK-type sub-sample, with baselines of 21.4–783.5 m in both cases. We integrated for 48 sec per source on the AGK-type sub-sample and 120 sec per source on the M-type sub-sample, for average rms sensitivities of 0.41 and 0.25 mJy beam^{-1}, respectively. Data calibration and imaging were performed using `CASA` 4.4.0. Data calibration by NRAO staff included flux, phase, bandpass, and gain calibrations. Flux calibration used observations of Titan, passband calibration used observations of J1427-4206, and gain calibration used observations of J1604-4228 or J1610-3958. We estimate an absolute flux calibration error of 10% based on variations in the gain calibrators.

We extract continuum and line images using standard routines in the `CASA` package. The 890 μm continuum images are extracted from the calibrated visibilities by first averaging over the continuum channels using the *split* routine, then imaging the visibilities using the *clean* routine with a Briggs robust weighting parameter of +0.5 for unresolved sources and −1.0 for resolved sources. The Briggs robust parameter of +0.5 balances point-source sensitivity and spatial resolution, providing an average beam size of 0″34×0″29 (∼50×45 AU at 150 pc) for unresolved sources. The Briggs robust parameter of −1.0 allows for slightly higher spatial resolution (at the cost of point-source sensitivity) for an average beam size of 0″33×0″27 (∼50×40 AU at 150 pc) for resolved sources.

We extract the ^{13}CO and C^{18}O $J = 3$–2 channel maps from the calibrated visibilities by first subtracting the continuum from the line regions using the *uvcontsub* routine, then imaging the visibilities using the *clean* routine with a Briggs robust weighting parameter of +0.5 in all cases due to the weakness of the line emission. We create zero-moment maps by integrating over the velocity channels showing line emission above the noise; the appropriate velocity range is determined for each source by visual inspection of the channel map and spectrum. If no line emission is detected, we sum across the average velocity range of the detected sources (± 2 km s^{-1}) around the average radial velocity (RV) of Lupus I–IV sources (3.7 km s^{-1}in the LSRK frame; Galli et al. 2013); note that the dispersion around this average RV is small (± 0.4 km s^{-1}) thus our method is unlikely to miss any detections.

Our ALMA Cycle 2 program did not observe Sz 76, Sz 77, Sz 91, V1094 Sco, or IM Lup. However, for IM Lup we utilize existing ALMA data (Cleeves et al. 2016) in this work. Thus we obtained ALMA data in the 890 μm continuum and ^{13}CO and C^{18}O $J = 3$–2 lines for 89 (out of 93) sources in our Lupus sample, for a 96% completeness rate. Continuum and line images for these sources are presented in the appendix of Ansdell et al. (2016c).

2.2.4 Dust Masses from 890 μm Continuum Emission

We measure the 890 μm continuum flux density for each source by an fitting elliptical Gaussian to the visibilities with *uvmodelfit* in `CASA`. The elliptical Gaussian model has six free parameters: integrated flux density ($F_{\rm cont}$), full width at half maximum (FWHM) of the major axis (a), aspect ratio of the axes (r), position angle (PA), and right ascension offset ($\Delta\alpha$) and declination offset ($\Delta\delta$) from the phase center. If $a/\sigma_a < 5$ then we instead fit a point-source model with three parameters ($F_{\rm cont}$, $\Delta\alpha$, $\Delta\delta$) to the visibilities.

For disks with resolved structure (e.g., TDs), we measure flux densities from the continuum images using circular aperture photometry. The aperture radius for each source is determined by a curve-of-growth method, in which we apply successively larger apertures until the measured flux density levels off. Uncertainties on the flux density are estimated by

Table 2.2: Lupus ALMA Continuum Properties

ID	RA$_{\text{J2000}}$	Dec$_{\text{J2000}}$	$F_{890\mu\text{m}}$ (mJy)	rms (mJy beam^{-1})	M_{dust} ($M_\oplus$)
Sz 65	15:39:27.756	-34:46:17.56	64.49 ± 0.32	0.30	15.16 ± 0.08
Sz 66	15:39:28.272	-34:46:18.44	14.78 ± 0.29	0.27	3.47 ± 0.07
J15430131-3409153	15:43:01.290	-34:09:15.40	0.01 ± 0.31	0.39	0.00 ± 0.07
J15430227-3444059	15:43:02.290	-34:44:06.20	0.22 ± 0.27	0.34	0.05 ± 0.06
J15445789-3423392	15:44:57.900	-34:23:39.50	-0.05 ± 0.18	0.24	-0.01 ± 0.04
J15450634-3417378	15:45:06.325	-34:17:38.28	15.00 ± 0.40	0.34	3.53 ± 0.09
J15450887-3417333	15:45:08.858	-34:17:33.81	46.27 ± 0.50	0.40	10.87 ± 0.12
Sz 68	15:45:12.851	-34:17:30.98	150.37 ± 0.46	0.61	35.34 ± 0.11
Sz 69	15:45:17.398	-34:18:28.66	16.96 ± 0.28	0.24	3.99 ± 0.07
Sz 71	15:46:44.718	-34:30:36.05	166.04 ± 0.63	0.37	39.02 ± 0.15
Sz 72	15:47:50.616	-35:28:35.75	14.10 ± 0.28	0.23	3.31 ± 0.07
Sz 73	15:47:56.927	-35:14:35.15	30.43 ± 0.55	0.39	7.15 ± 0.13
Sz 74	15:48:05.217	-35:15:53.29	20.94 ± 0.27	0.29	4.92 ± 0.06
Sz 81A	15:55:50.272	-38:01:34.05	9.46 ± 0.18	0.23	2.22 ± 0.04
IM Lup	15:56:09.18	-37:56:06.12	590.00 ± 90.00	0.21	138.66 ± 21.15
Sz 83	15:56:42.298	-37:49:15.82	426.90 ± 0.72	0.56	100.33 ± 0.17
Sz 84	15:58:02.508	-37:36:03.08	32.64 ± 0.40	0.32	7.67 ± 0.09
Sz 129	15:59:16.463	-41:57:10.66	181.12 ± 0.52	0.33	42.57 ± 0.12
J15592523-4235066	15:59:25.240	-42:35:07.17	-0.03 ± 0.19	0.24	-0.01 ± 0.04
RY Lup	15:59:28.376	-40:21:51.57	275.50 ± 1.16	0.50	64.75 ± 0.27
J16000060-4221567	16:00:00.594	-42:21:57.12	2.40 ± 0.19	0.25	0.56 ± 0.04
J16000236-4222145	16:00:02.348	-42:22:14.99	119.85 ± 0.63	0.34	28.17 ± 0.15
J16002612-4153553	16:00:26.110	-41:53:55.76	1.20 ± 0.19	0.25	0.28 ± 0.04
Sz 130	16:00:31.030	-41:43:37.33	6.19 ± 0.35	0.24	1.45 ± 0.08
MY Lup	16:00:44.509	-41:55:31.27	176.81 ± 0.76	0.56	41.55 ± 0.18
Sz 131	16:00:49.421	-41:30:04.24	8.57 ± 0.29	0.23	2.01 ± 0.07
J16011549-4152351	16:01:15.534	-41:52:35.52	82.07 ± 0.89	0.57	19.29 ± 0.21
Sz 133	16:03:29.383	-41:40:02.14	69.05 ± 0.77	0.55	16.23 ± 0.18
Sz 88A	16:07:00.575	-39:02:19.89	8.94 ± 0.30	0.27	3.74 ± 0.13
Sz 88B	16:07:00.620	-39:02:18.10	-0.20 ± 0.19	0.26	-0.08 ± 0.08
J16070384-3911113	16:07:03.830	-39:11:11.75	4.52 ± 0.55	0.25	1.89 ± 0.23
J16070854-3914075	16:07:08.546	-39:14:07.88	92.07 ± 1.49	0.49	38.47 ± 0.62
Sz 90	16:07:10.062	-39:11:03.64	21.83 ± 0.46	0.37	9.12 ± 0.19
J16073773-3921388	16:07:37.718	-39:21:39.12	1.91 ± 0.18	0.23	0.80 ± 0.08
Sz 95	16:07:52.303	-38:58:06.45	4.08 ± 0.18	0.25	1.70 ± 0.08
J16075475-3915446	16:07:54.760	-39:15:44.74	2.55 ± 0.46	0.33	1.07 ± 0.19
J16080017-3902595	16:08:00.168	-39:02:59.87	3.01 ± 0.17	0.21	1.26 ± 0.07
J16080175-3912316	16:08:01.750	-39:12:31.60	0.28 ± 0.26	0.34	0.12 ± 0.11
Sz 96	16:08:12.617	-39:08:33.80	4.08 ± 0.28	0.24	1.70 ± 0.12
J16081497-3857145	16:08:14.960	-38:57:14.89	8.32 ± 0.30	0.25	3.48 ± 0.13
Sz 97	16:08:21.791	-39:04:21.85	4.64 ± 0.18	0.23	1.94 ± 0.08
Sz 98	16:08:22.484	-39:04:46.81	237.29 ± 1.42	0.51	99.14 ± 0.59
Sz 99	16:08:24.040	-39:05:49.40	-0.04 ± 0.18	0.22	-0.02 ± 0.08
Sz 100	16:08:25.749	-39:06:01.63	54.85 ± 0.58	0.30	22.92 ± 0.24
J160828.1-391310	16:08:28.100	-39:13:10.00	0.23 ± 0.18	0.24	0.10 ± 0.08
Sz 103	16:08:30.257	-39:06:11.53	11.54 ± 0.28	0.24	4.82 ± 0.12

J16083070-3828268	16:08:30.687	-38:28:27.21	135.31 ± 1.12	0.48	56.53 ± 0.47
Sz 104	16:08:30.804	-39:05:49.21	3.15 ± 0.19	0.25	1.32 ± 0.08
J160831.1-385600	16:08:31.100	-38:56:00.00	0.25 ± 0.26	0.32	0.10 ± 0.11
V856 Sco	16:08:34.280	-39:06:18.68	55.81 ± 0.28	0.36	23.32 ± 0.12
Sz 106	16:08:39.748	-39:06:25.71	1.99 ± 0.20	0.26	0.83 ± 0.08
Sz 108B	16:08:42.868	-39:06:15.04	26.77 ± 0.34	0.26	11.18 ± 0.14
J16084940-3905393	16:08:49.389	-39:05:39.79	1.70 ± 0.17	0.21	0.71 ± 0.07
V1192 Sco	16:08:51.428	-39:05:30.84	0.91 ± 0.19	0.24	0.38 ± 0.08
Sz 110	16:08:51.561	-39:03:18.03	15.40 ± 0.29	0.23	6.43 ± 0.12
J16085324-3914401	16:08:53.227	-39:14:40.53	19.57 ± 0.28	0.23	8.18 ± 0.12
J16085373-3914367	16:08:53.722	-39:14:37.16	3.17 ± 0.19	0.20	1.32 ± 0.08
Sz 111	16:08:54.673	-39:37:43.49	179.39 ± 0.98	0.33	74.95 ± 0.41
J16085529-3848481	16:08:55.279	-38:48:48.52	1.81 ± 0.18	0.26	0.76 ± 0.08
Sz 112	16:08:55.517	-39:02:34.32	3.89 ± 0.17	0.21	1.63 ± 0.07
Sz 113	16:08:57.792	-39:02:23.21	22.35 ± 0.27	0.22	9.34 ± 0.11
J16085828-3907355	16:08:58.270	-39:07:35.50	0.16 ± 0.25	0.31	0.07 ± 0.10
J16085834-3907491	16:08:58.300	-39:07:49.40	0.04 ± 0.26	0.34	0.02 ± 0.11
J16090141-3925119	16:09:01.403	-39:25:12.34	17.50 ± 0.68	0.30	7.31 ± 0.28
Sz 114	16:09:01.836	-39:05:12.79	96.41 ± 0.41	0.32	40.28 ± 0.17
Sz 115	16:09:06.210	-39:08:51.80	0.29 ± 0.18	0.24	0.12 ± 0.08
J16091644-3904438	16:09:16.430	-39:04:43.70	0.24 ± 0.26	0.34	0.10 ± 0.11
J16092032-3904015	16:09:20.300	-39:04:01.60	0.13 ± 0.24	0.34	0.05 ± 0.10
J16092317-3904074	16:09:23.150	-39:04:07.40	0.25 ± 0.26	0.34	0.10 ± 0.11
J16092697-3836269	16:09:26.970	-38:36:27.28	3.89 ± 0.27	0.35	1.63 ± 0.11
J160934.2-391513	16:09:34.180	-39:15:12.70	-0.56 ± 0.28	0.34	-0.23 ± 0.12
J16093928-3904316	16:09:39.290	-39:04:31.80	0.12 ± 0.26	0.33	0.05 ± 0.11
Sz 117	16:09:44.347	-39:13:30.50	10.47 ± 0.18	0.25	4.37 ± 0.08
Sz 118	16:09:48.640	-39:11:17.23	63.34 ± 0.97	0.57	26.46 ± 0.41
J16095628-3859518	16:09:56.285	-38:59:51.90	7.44 ± 0.18	0.24	3.11 ± 0.08
J16100133-3906449	16:10:01.320	-39:06:44.90	0.33 ± 0.25	0.30	0.14 ± 0.10
J16101307-3846165	16:10:13.060	-38:46:16.80	0.01 ± 0.19	0.24	0.00 ± 0.08
J16101857-3836125	16:10:18.560	-38:36:13.00	-0.46 ± 0.18	0.22	-0.19 ± 0.08
J16101984-3836065	16:10:19.840	-38:36:06.80	0.55 ± 0.19	0.23	0.23 ± 0.08
J16102741-3902299	16:10:27.430	-39:02:30.20	0.59 ± 0.27	0.33	0.25 ± 0.11
J16102955-3922144	16:10:29.544	-39:22:14.83	7.14 ± 0.35	0.22	2.98 ± 0.15
J16104536-3854547	16:10:45.380	-38:54:54.90	-0.56 ± 0.29	0.36	-0.23 ± 0.12
Sz 123B	16:10:51.310	-38:53:12.80	-0.28 ± 0.19	0.24	-0.12 ± 0.08
Sz 123A	16:10:51.579	-38:53:14.11	40.64 ± 0.56	0.32	16.98 ± 0.23
J16115979-3823383	16:11:59.810	-38:23:38.50	0.09 ± 0.18	0.21	0.04 ± 0.08
J16120445-3809589	16:12:04.480	-38:09:59.00	-0.04 ± 0.28	0.35	-0.02 ± 0.12
J16121120-3832197	16:12:11.220	-38:32:19.80	0.08 ± 0.27	0.35	0.03 ± 0.11
J16124373-3815031	16:12:43.741	-38:15:03.40	29.88 ± 0.49	0.38	12.48 ± 0.20
J16134410-3736462	16:13:44.083	-37:36:46.60	2.14 ± 0.30	0.39	0.89 ± 0.13

taking the standard deviation of the flux densities measured within a same-sized aperture placed randomly within the field of view but away from the source.

Table 2.2 gives our measured 890 μm continuum flux densities and associated uncertainties (the latter are statistical errors, thus do not include the 10% absolute flux calibration error described in Section 2.2.3). For IM Lup, we report the ALMA 875 μm continuum flux from Cleeves et al. (2016). Of these 89 sources observed by ALMA, 62 were detected at $>3\sigma$ significance; Figure 2.3 shows the continuum images of the 61 sources detected by our ALMA Cycle 2 program (i.e., excluding IM Lup). Table 2.2 also provides the fitted source centers output by *uvmodelfit* for the detected sources, or the phase centers of our ALMA observations (i.e., 2MASS positions) for the non-detected sources. The reported rms values are derived from 4–9″ radius annuli centered on the fitted or expected source positions for detected or non-detected sources, respectively.

We calculate M_{dust} by inputting the (sub-)mm continuum flux densities from Table 2.2 and the source distances from Table 2.1 into Equation 2.1; the calculated M_{dust} values are reported in Table 2.2. Figure 2.5 (top panel) shows M_{dust} for the continuum-detected disks in Lupus, illustrating how even at this young age only 26% of disks have sufficient reservoirs of dust to form giant planet cores (i.e., $M_{\text{dust}} \gtrsim 10\ M_{\oplus}$).

2.2.5 Gas Masses from CO $J = 3$–2 Line Emission

We measure ^{13}CO and C^{18}O $J = 3$–2 integrated flux densities and associated uncertainties from our ALMA zero-moment maps (§2.2.3) using the same aperture photometry method described above for structured continuum sources (§2.2.4). For non-detections, we take upper limits of $3\times$ the uncertainty when using an aperture that is the same size as the beam ($\sim$0.3″). Table 2.3 gives our measured integrated flux densities or upper limits. For IM Lup, we report the corresponding ALMA line measurements from Cleeves et al. (2016). Of the 89 targets, 36 were detected in ^{13}CO while only 11 were detected in C^{18}O at $>3\sigma$ significance. All sources detected in C^{18}O were also detected in ^{13}CO, and all sources detected in ^{13}CO were also detected in the continuum.
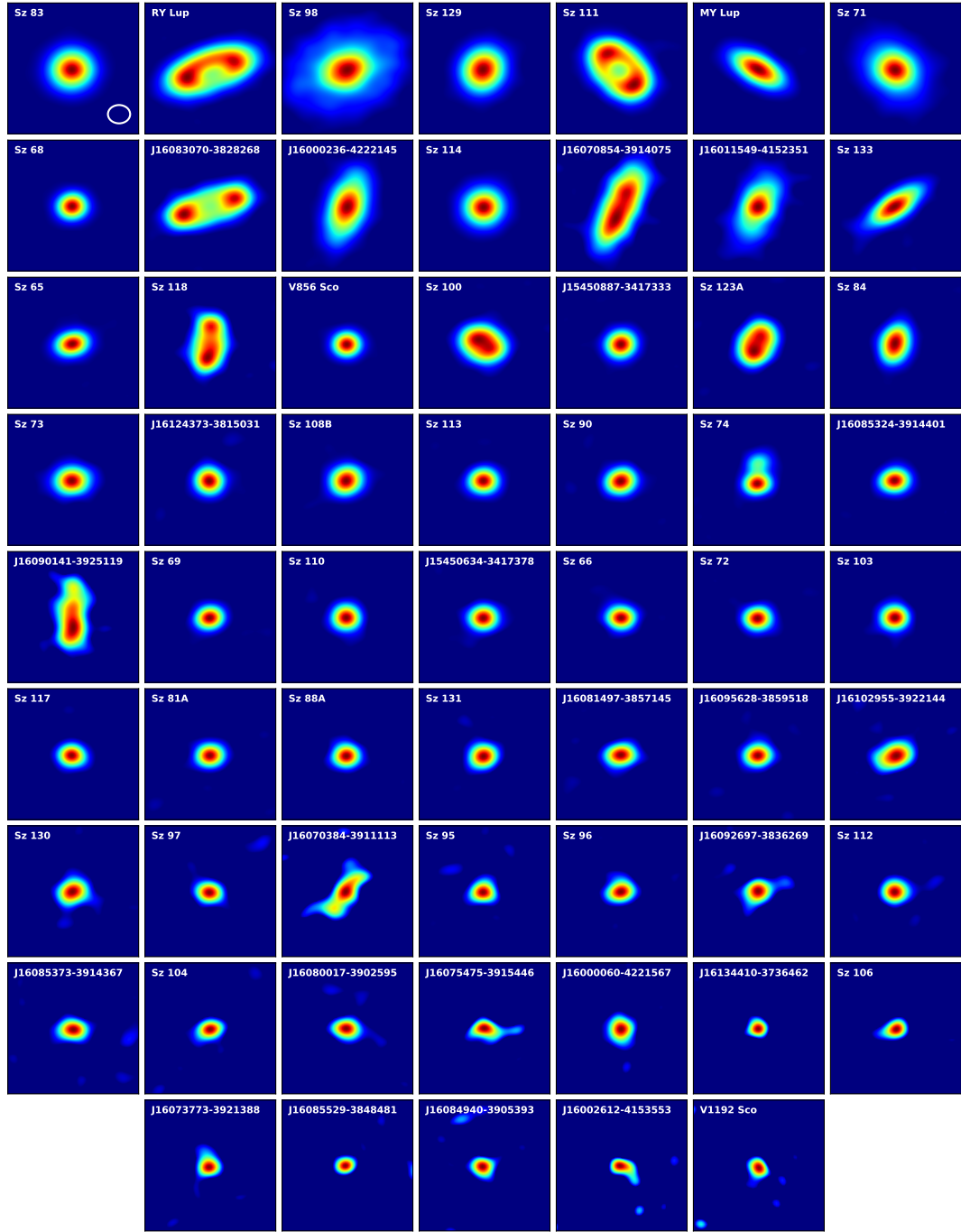
Figure 2.3 The 890 μm continuum images for the 61 disks detected in our ALMA Cycle 2 survey of Lupus, ordered by decreasing flux density (as reported in Table 2.2). We exclude IM Lup, which is presented in Cleeves et al. (2016). Images are $2'' \times 2''$ and the typical beam size of $0\!''\!.34 \times 0\!''\!.28$ (§2.2.3) is shown in the first panel.

27

Table 2.3: Lupus ALMA CO Line Properties

ID	F_{13CO} (mJy km s^{-1})	F_{C18O} (mJy km s^{-1})	M_{gas} (M_{Jup})	$M_{gas,min}$ (M_{Jup})	$M_{gas,max}$ (M_{Jup})
Sz 65	971 ± 128	415 ± 105	0.7	0.3	10.5
Sz 66	153 ± 45	< 111	0.2		1.0
J15430131-3409153	< 162	< 192			1.0
J15430227-3444059	< 138	< 171			1.0
J15445789-3423392	< 84	< 102			0.3
J15450634-3417378	356 ± 111	< 174	0.1		3.1
J15450887-3417333	759 ± 87	573 ± 145	3.2	1.0	10.5
Sz 68	915 ± 133	444 ± 132	0.8	0.3	10.5
Sz 69	466 ± 74	< 102	0.2		3.1
Sz 71	1298 ± 107	< 111	0.3		1.0
Sz 72	< 93	< 105			0.3
Sz 73	< 177	< 189			1.0
Sz 74	< 93	< 111			0.3
Sz 81A	< 87	< 105			0.3
IM Lup	11500 ± 1700	2700 ± 400	6.7	3.1	31.4
Sz 83	3078 ± 155	994 ± 152	2.8	1.0	10.5
Sz 84	924 ± 110	< 120	0.4		3.1
Sz 129	516 ± 72	< 108	0.2		1.0
J15592523-4235066	< 93	< 105			0.3
RY Lup	4624 ± 225	1143 ± 147	2.5	1.0	10.5
J16000060-4221567	< 96	< 114			0.3
J16000236-4222145	1890 ± 124	< 111	0.7		1.0
J16002612-4153553	< 72	< 102			0.3
Sz 130	470 ± 71	< 117	0.2		3.1
MY Lup	874 ± 154	< 267	0.4		3.1
Sz 131	251 ± 60	< 102	0.1		1.0
J16011549-4152351	3320 ± 317	1558 ± 182	6.7	1.0	31.4
Sz 133	746 ± 108	< 240	0.3		3.1
Sz 88A	< 96	< 123			1.0
Sz 88B	< 72	< 102			1.0
J16070384-3911113	1248 ± 100	295 ± 69	1.4	0.3	10.5
J16070854-3914075	1232 ± 173	< 183	0.9		3.1
Sz 90	433 ± 98	< 183	0.3		10.5
J16073773-3921388	< 90	< 105			1.0
Sz 95	217 ± 48	< 120	0.2		3.1
J16075475-3915446	< 147	< 174			1.0
J16080017-3902595	< 90	< 102			1.0
J16080175-3912316	< 135	< 168			1.0
Sz 96	< 93	< 102			1.0
J16081497-3857145	170 ± 42	< 114	0.1		1.0
Sz 97	< 90	< 108			1.0
Sz 98	506 ± 120	< 183	0.4		10.5
Sz 99	< 84	< 96			1.0
Sz 100	1050 ± 69	< 105	0.4		1.0
J160828.1-391310	< 90	< 93			1.0
Sz 103	< 90	< 102			1.0

Table 2.3: (Continued) Lupus ALMA CO Line Properties

J16083070-3828268	6682 ± 262	1697 ± 238	8.2	3.1	31.4
Sz 104	< 96	< 114			1.0
J160831.1-385600	< 132	< 168			1.0
V856 Sco	< 153	< 186			1.0
Sz 106	< 96	< 120			1.0
Sz 108B	370 ± 63	209 ± 45	0.9	0.3	3.1
J16084940-3905393	< 84	< 99			1.0
V1192 Sco	< 96	< 111			1.0
Sz 110	< 90	< 105			1.0
J16085324-3914401	267 ± 46	< 135	0.2		3.1
J16085373-3914367	< 93	< 108			1.0
Sz 111	2381 ± 146	714 ± 73	3.3	1.0	10.5
J16085529-3848481	< 96	< 108			1.0
Sz 112	< 84	< 102			1.0
Sz 113	< 84	< 105			1.0
J16085828-3907355	< 132	< 156			1.0
J16085834-3907491	< 144	< 165			1.0
J16090141-3925119	1637 ± 95	< 117	1.0		1.0
Sz 114	716 ± 105	< 102	0.4		3.1
Sz 115	< 66	< 99			0.3
J16091644-3904438	< 147	< 171			1.0
J16092032-3904015	< 132	< 156			1.0
J16092317-3904074	< 135	< 171			1.0
J16092697-3836269	591 ± 108	< 180	0.4		10.5
J160934.2-391513	< 147	< 174			1.0
J16093928-3904316	< 144	< 159			1.0
Sz 117	< 90	< 108			1.0
Sz 118	695 ± 133	< 234	0.5		10.5
J16095628-3859518	< 93	< 105			1.0
J16100133-3906449	< 126	< 156			1.0
J16101307-3846165	< 90	< 111			1.0
J16101857-3836125	< 84	< 102			1.0
J16101984-3836065	< 87	< 102			1.0
J16102741-3902299	< 141	< 165			1.0
J16102955-3922144	963 ± 76	< 90	0.4		1.0
J16104536-3854547	< 147	< 177			1.0
Sz 123B	< 93	< 108			1.0
Sz 123A	1112 ± 107	< 108	0.5		1.0
J16115979-3823383	< 90	< 96			1.0
J16120445-3809589	< 144	< 174			1.0
J16121120-3832197	< 144	< 171			1.0
J16124373-3815031	< 168	< 207			1.0
J16134410-3736462	468 ± 112	< 240	0.4		10.5

We estimate M_{gas} independently from M_{dust} by comparing our measured ^{13}CO and C^{18}O line luminosities to the model grids of WB14 (§2.1.2). This comparison is illustrated in Figure 2.4, where the two panels show different values for the C^{18}O isotopologue abundance: the ISM value (left) and a factor of three lower (right). The reduced C^{18}O abundance was required to fit some of the Taurus disk observations in WB14, and is similarly necessary to fit some of the Lupus disk observations in this work; specifically, the left panel of Figure 2.4 shows that some upper limits do not match any model grid points when assuming an ISM-like C^{18}O abundance. The physical reasoning for a reduced C^{18}O abundance is CO isotope-selective photodissociation (van Dishoeck & Black 1988), which has been modeled in detail for protoplanetary disks in Miotello et al. (2014). The empirical factor of three used in Figure 2.4 is sufficient to fit our Lupus observations, and also lies within the range of physical-chemical models from Miotello et al. (2017) for most detected disks, although for lower-mass disks ($M_{\mathrm{gas}} \lesssim 10^{-4}\ M_\odot$) the C^{18}O line luminosities may be further reduced due to stronger isotope-selective photodissociation effects.

Our derived M_{gas} values, given in Table 2.3, are determined by comparing our ^{13}CO and C^{18}O line luminosity measurements or upper limits to the WB14 model grids. We consider both WB14 model grids (ISM and 3× reduced C^{18}O abundance) in order to take into account possible isotope-selective photodissociation effects. The line luminosity uncertainties include the statistical errors in Table 2.3 as well as the 10% absolute flux calibration error (added in quadrature). For the 11 sources detected in both ^{13}CO and C^{18}O, M_{gas} is the geometric mean of the WB14 model grid points within $\pm 3\sigma$ of our measured ^{13}CO and C^{18}O line luminosities; we also set upper ($M_{\mathrm{gas,max}}$) and lower ($M_{\mathrm{gas,min}}$) limits based on the maximum and minimum WB14 model grid points consistent with the data. For the 25 sources with ^{13}CO detections and C^{18}O upper limits, we similarly calculate M_{gas} and $M_{\mathrm{gas,max}}$, but do not constrain $M_{\mathrm{gas,min}}$ as the effects of isotope-selective photodissociation may be stronger for low-mass disks ($M_{\mathrm{gas}} \lesssim 10^{-4}\ M_\odot$; Miotello et al. 2017). For the 53 disks undetected in both lines, we set only $M_{\mathrm{gas,max}}$ using the maximum model grid points consistent with the ^{13}CO and C^{18}O upper limits.
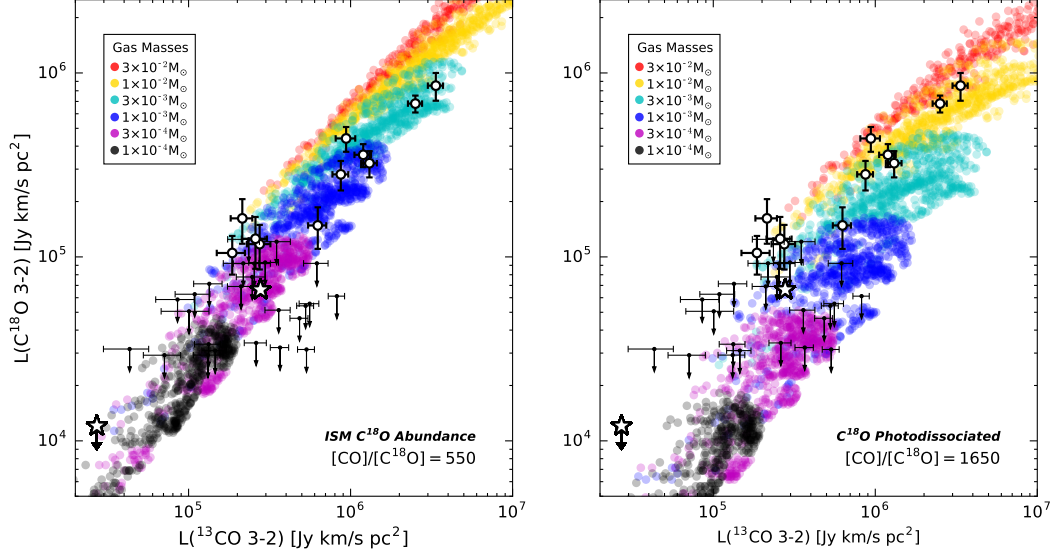
Figure 2.4 The ^{13}CO and C^{18}O $J = 3$–2 line luminosities used to determine disk gas masses (§2.2.5). The WB14 model grids are color-coded by gas mass and the two panels show different [C^{18}O]/[CO] isotopologue ratios: the ISM value of 550 (left) and 3× reduced abundance (right) to account for isotope-selective photodissociation. The 11 Lupus disks with both lines detected are plotted as white circles, and the 25 Lupus disks with only ^{13}CO detections are plotted as black circles with arrows indicating 3σ upper limits on C^{18}O. Error bars include both the statistical uncertainties (Table 2.3) and the 10% flux calibration error. Stars show the stacked non-detections (§2.2.6) where error bars are smaller than the symbol.

Figure 2.5 (middle panel) shows the derived gas masses for the continuum-detected sources in our Lupus sample. The disk gas masses are low, in most cases much less than the MMSN. For disks with at least one line detection, the inferred gas-to-dust ratios are almost universally below the ISM value of 100 (Figure 2.5, bottom panel). These low gas masses and low gas-to-dust ratios expand on the findings of WB14, who presented a similar result for a small sample of nine disks around K/M-type sources in Taurus.

2.2.6 Stacking Analysis

We perform a stacking analysis to constrain the average dust and gas mass of the individually undetected sources in our sample. Before stacking, we center each image on the expected source location and scale the flux to 200 pc. We then measure flux densities in the stacked images using the aperture photometry method described in §2.2.4. We confirm that the
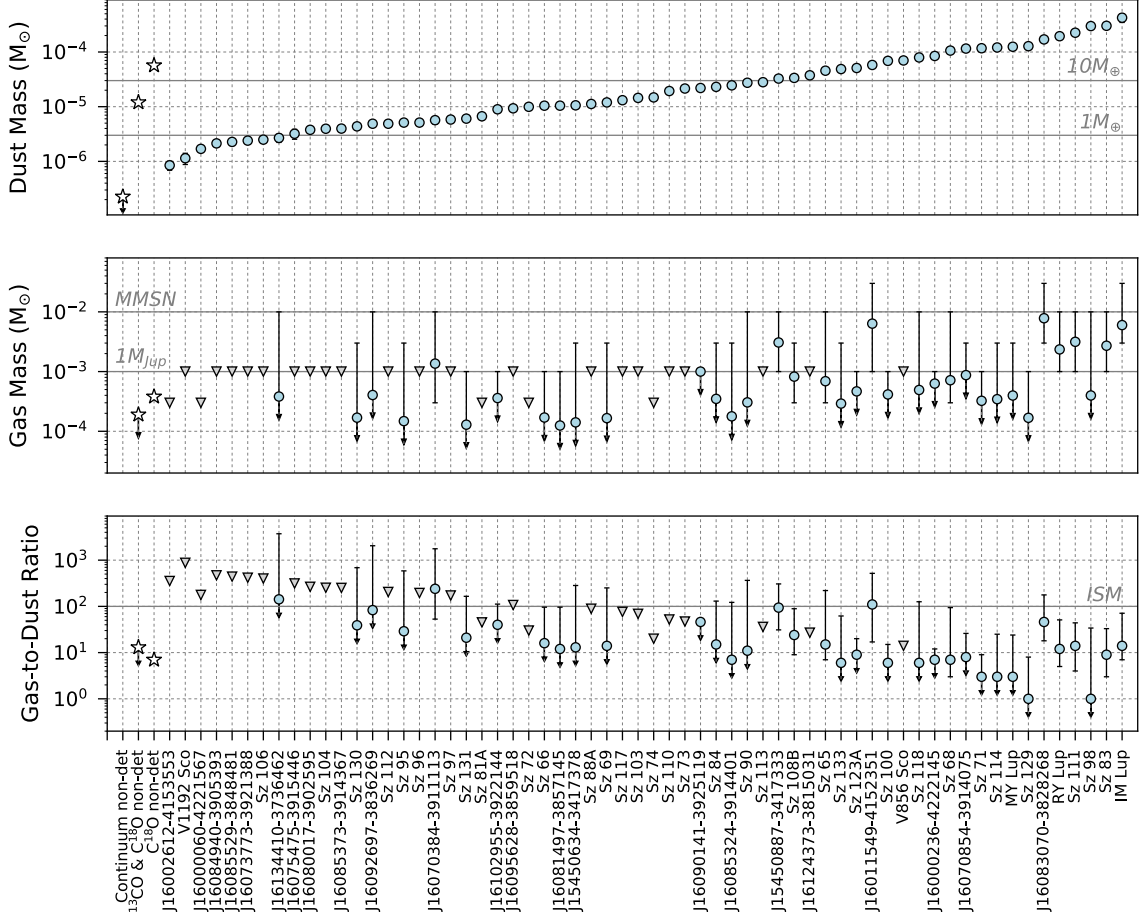
Figure 2.5 Dust masses (top), gas masses (middle), and gas-to-dust ratios (bottom) for the continuum-detected sources in our Lupus ALMA sample. Blue circles are detections and gray triangles are upper limits. Dust masses are from Table 2.2 and error bars include the 10% absolute flux calibration uncertainty. Gas masses and associated ranges are from Table 2.3, and sources with downward-facing arrows are those detected in ^{13}CO but not $C^{18}O$ (for which we did not place lower limits on their gas masses; §2.2.5). Gas-to-dust ratios and associated ranges are directly calculated from the dust masses and range of possible gas masses. Stars show the results of our stacking analysis (§2.2.6).

source locations are known to sufficient accuracy for stacking by measuring the average offset of the detected sources from their phase centers: we find $\langle \Delta\alpha \rangle = -0.15''$ and $\langle \Delta\delta \rangle = -0.22''$, both smaller than the average beam size. Moreover, because the dispersion around the mean RV of Lupus I-IV sources is much smaller than the velocity range over which we integrated the zero-moment maps (§2.2.3), any RV differences among the gas non-detections should have negligible effects on the stacking.
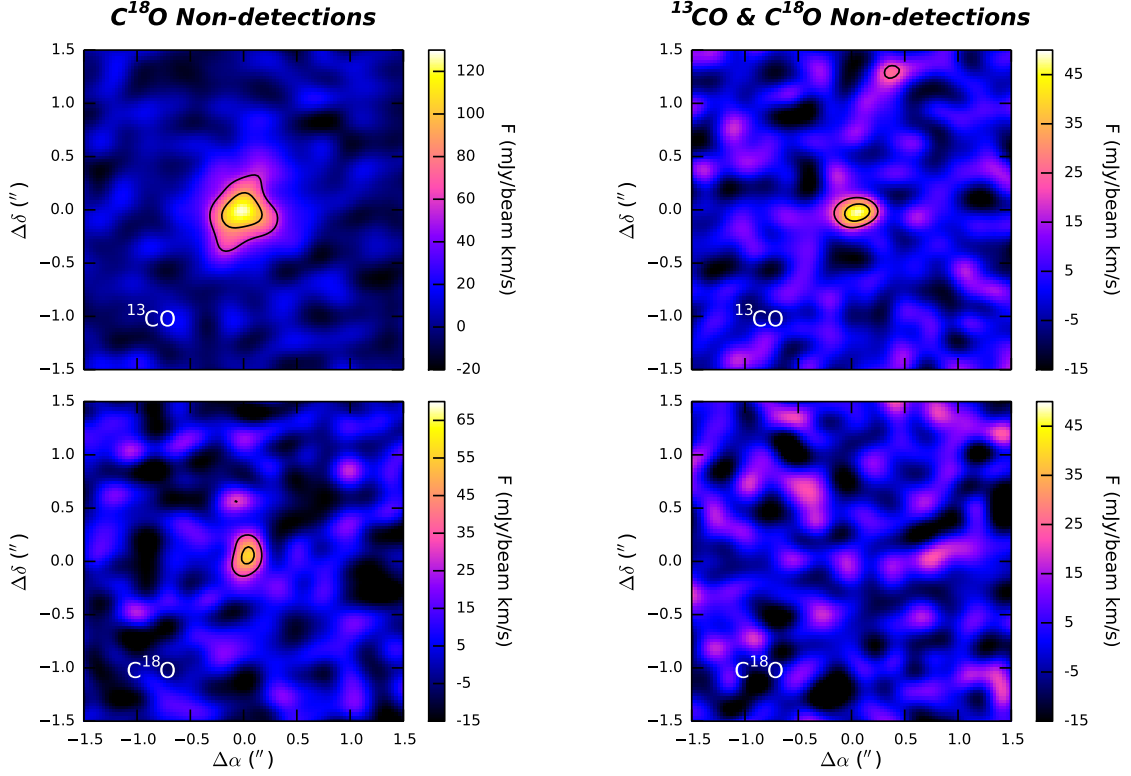
Figure 2.6 Stacks of the individually undetected sources (§2.2.6). The left panel shows stacks of sources detected in the continuum and ^{13}CO, but not C^{18}O. The right panel shows stacks of sources detected in the continuum, but neither ^{13}CO nor C^{18}O. The top panels show ^{13}CO stacks and the bottom panels show C^{18}O stacks. Contour lines are 3σ and 5σ.

We first stack the 27 continuum non-detections, but do not find a significant mean signal in the continuum, ^{13}CO, or C^{18}O stacks. The lack of line emission is expected given the undetected continuum, but the absence of continuum emission is surprising given the sensitivity of the stacked image. We measure a mean signal of 0.08 ± 0.06 mJy, which gives a 3σ upper limit on the average dust mass of individually undetected continuum sources of ~6 Lunar masses (0.03 $M_{\oplus}$), comparable to debris disk levels (Wyatt 2008). The stark contrast between the detected and undetected continuum sources (Figure 2.5, top panel) suggests that protoplanetary disks evolve quickly to debris disk levels once disk clearing begins (Alexander et al. 2014).

33

We then stack the 25 sources detected in the continuum and ^{13}CO, but not C^{18}O. We measure a continuum mean signal of 45.25 ± 0.20 mJy and a ^{13}CO mean signal of 586 ± 27 mJy km s^{-1} (Figure 2.6, upper left panel). Interestingly, the stacking also reveals a significant mean signal for C^{18}O of 132 ± 20 mJy km s^{-1} (Figure 2.6, lower left panel). The stacked continuum flux corresponds to $M_{\rm dust} \sim 19~M_{\oplus}$ and the stacked line fluxes correspond to $M_{\rm gas} \sim 0.4~M_{\rm Jup}$ (Figure 2.4), giving an average gas-to-dust ratio of only ~ 7 for sources detected in the continuum and ^{13}CO, but not C^{18}O (Figure 2.5, bottom panel).

Finally, we stack the 26 sources detected in the continuum, but undetected in both ^{13}CO and C^{18}O. We measure a continuum mean signal of 9.53 ± 0.13 mJy. The stacking also reveals a significant mean signal for ^{13}CO (Figure 2.6, upper right panel), but not C^{18}O (Figure 2.6, lower right panel); the stacked gas fluxes are 54 ± 7 mJy km s^{-1} and 3 ± 8 mJy km s^{-1}, respectively. The continuum flux corresponds to $M_{\rm dust} \sim 4~M_{\oplus}$ while the ^{13}CO line flux and C^{18}O upper limit correspond to $M_{\rm gas} \lesssim 0.2~M_{\rm Jup}$ (Figure 2.4), for an average gas-to-dust ratio of $\lesssim 13$ for disks detected in the continuum but undetected in ^{13}CO and C^{18}O (Figure 2.5, bottom panel).

2.3 σ Orionis: Can Middle-aged Disks Still Make Planets?

2.3.1 Overview

The σ Orionis cluster is a particularly important target for studying protoplanetary disk evolution, as it is the only nearby ($\lesssim 400$ pc) star-forming region with an intermediate age (~ 3–5 Myr; Oliveira et al. 2002, 2004) that is comparable to the characteristic disk lifetime (Figure 1.2). The disk dust and gas distributions in σ Orionis can therefore be used to analyze what types of planets can still form in middle-aged clusters, or to test whether planet formation is essentially complete at this stage.

The σ Orionis cluster consists of several hundred YSOs, ranging from brown dwarfs to OB-type stars, and is named after its brightest member, σ Ori, a trapezium-like system whose most massive component is an O9V star. Walter et al. (2008) reviewed

the properties of σ Orionis, summarizing the region as "an older and less massive analog of the Orion Nebula Cluster." We adopt a cluster distance of 385 pc based on orbital parallax measurements of the σ Ori triple system (Schaefer et al. 2016). This relative proximity, as well as the low reddening towards the cluster ($A_\mathrm{V} \sim 0.2$; Sherry et al. 2008), make σ Orionis a valuable site for studying young star-disk systems.

Cluster membership is defined by the Mayrit catalog (Caballero 2008), which identifies 241 stars and brown dwarfs located within $30'$ of the σ Ori system exhibiting known features of youth (X-ray emission, Li 6708Å absorption, etc.). Almost all members of σ Orionis have photometry in optical ($UVBRI$), near-IR (2MASS JHK_S), and mid-IR (*Spitzer* IRAC/MIPS; Hernández et al. 2007) bandpasses. The majority of sources have their stellar spectral types determined from a homogenous sample of low-resolution optical spectra (Hernández et al. 2014) and membership confirmed with RV measurements (Jeffries et al. 2006; Sacco et al. 2008; Maxted et al. 2008). However, contamination from the PMS populations of the background Orion OB 1a/1b associations may still exist due to similar RVs and small proper motions (Walter et al. 2008).

Williams et al. (2013) surveyed the inner $\sim 0°.5$ region of the σ Orionis cluster at 850 μm using JCMT/SCUBA-2, detecting only eight disks with an rms sensitivity of 2.9 mJy beam^{-1}, which corresponds to $M_\mathrm{dust} \sim 4\ M_\oplus$. Interestingly, the SEDs of their limited number of detections exhibit remarkable diversity by including Class I, Class II, Class III, and TD objects (see their Figure 3). The dearth of sub-mm continuum detections in σ Orionis is indicative of low disk dust masses when compared to younger regions (e.g., Lupus; see Figure 2.5), while the diverse SEDs testify to the substantial and ongoing disk evolution at this intermediate age. Follow-up SMA observations of the eight continuum-detected sources revealed faint CO emission (see Figure 5 in Williams et al. 2013), demonstrating that molecular gas still exists in these disks. By stacking the individually undetected disks, Williams et al. (2013) also found a significant mean continuum signal of $F_{850\mu m} = 1.3 \pm 0.3$ mJy (4σ), suggesting that higher-sensitivity observations should reveal many more detections, thus motivating a follow-up survey with ALMA.
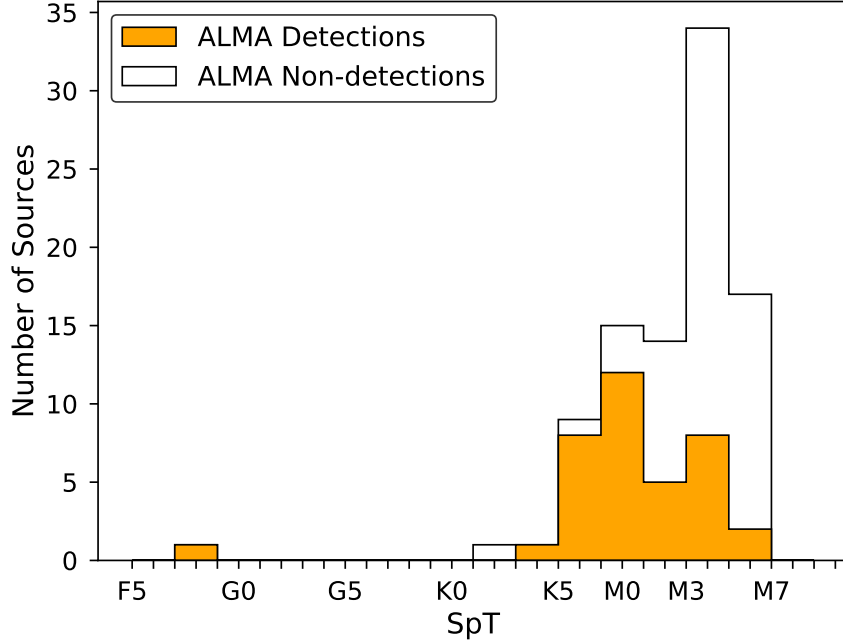
Figure 2.7 Distribution of stellar spectral types (SpT) in our σ Orionis ALMA sample (Table 2.4). The open histogram shows the entire sample, while the orange histogram shows only the sources detected in the ALMA continuum (§2.3.4).

2.3.2 Sample Selection

Our sample consists of the 92 YSOs in σ Orionis with masses above the brown-dwarf limit ($\geq$0.1 $M_\odot$) and IR excesses consistent with the presence of protoplanetary disks. These sources were selected by cross-matching the aforementioned Mayrit catalog (Caballero 2008) with the Class II and TD candidates identified in the *Spitzer* survey of σ Orionis by Hernández et al. (2007). Disk classifications were based on the IR spectral index slope (§1.1.1) measured between *Spitzer*/IRAC [3.6] and [8.0] bands in Hernández et al. (2007). We include a Class I disk in our sample (SO 1153), as it is located near the border with Class II disks. These cluster membership and disk catalogues, and thus our sample, are expected to be complete down to the brown dwarf limit.

Table 2.4 presents our sample with some basic stellar and disk properties; we adopt the source IDs from Hernández et al. (2007) in this work. The SpT classifications are primarily taken from the homogenous sample of low-resolution optical spectra analyzed

36

in Hernández et al. (2014), but supplemented with those derived from higher-resolution VLT/X-Shooter spectra when available from Rigliaco et al. (2012). For the 23 sources without spectroscopic information, we estimate SpT classifications using an empirical relation with $V - J$ color; the relation was derived by measuring synthetic photometry from flux-calibrated VLT/X-Shooter spectra of YSOs ranging from G5 to M9.5 (Manara et al. 2017), then performing a non-parametric fit of SpT to synthetic $V - J$ color. For these sources with photometrically derived SpT values, we cautiously assume uncertainties of $\pm$ two spectral subtypes. Figure 2.7 shows the SpT distribution of our sample.

We estimate $M_\star$ for our sample by comparing their positions on the Hertzsprung-Russel (HR) diagram to the stellar evolution models of Siess et al. (2000). In order to place our targets on the HR diagram, we convert SpT to $T_{\rm eff}$ and derive $L_\star$ from 2MASS J-band magnitudes using the model-dependent relations in Herczeg & Hillenbrand (2015). Uncertainties on $L_\star$ are obtained by propagating the uncertainties on SpT and bolometric correction, and thus on distance and A_V. We then calculate the uncertainties on $M_\star$ using a Monte Carlo (MC) method, where we take the standard deviation of 1000 estimates of $M_\star$, each calculated after randomly perturbing $T_{\rm eff}$ and $L_\star$ by their uncertainties.

2.3.3 ALMA Observations

The ALMA Cycle 3 observations of our σ Orionis sample were obtained in Band 6 on 2016 July 30 and 31 (Project ID: 2015.1.00089.S; PI: Williams). The array configuration used 36 and 37 12 m antennas on July 30 and 31, respectively, with baselines of 15–1124 m on both runs. The correlator setup included two broadband continuum windows centered on 234.293 and 216.484 GHz with bandwidths of 2.000 and 1.875 GHz and channel widths of 15.625 and 0.976 MHz, respectively. The bandwidth-weighted mean continuum frequency was 225.676 GHz (1.33 mm). The spectral windows covered the ^{12}CO (230.538 GHz), ^{13}CO (220.399 GHz), and C^{18}O (219.560 GHz) $J = 2$–1 transitions at velocity resolutions of 0.16-0.17 km s^{-1}. These spectral windows were centered on 230.531, 220.392, and 219.554 GHz with bandwidths of 11.719 MHz and channel widths of 0.122 MHz.

Table 2.4: σ Orionis Sample Properties

ID	V	J	Disk	SpT	$M_\star(M_\odot)$	Reference
1036	14.7	11.3	II	K7.5 $\pm$ 0.5	0.67 $\pm$ 0.06	Hernandez et al. (2014)
1050	18.0	13.5	II	M3.6 $\pm$ 2.0	0.22 $\pm$ 0.14	$V - J$ color
1075		12.8	II	M0.0 $\pm$ 1.5	0.62 $\pm$ 0.14	Hernandez et al. (2014)
1152	15.4	11.6	II	M0.0 $\pm$ 1.0	0.62 $\pm$ 0.16	Hernandez et al. (2014)
1153	14.3	11.8	I/II	K5.5 $\pm$ 1.0	0.91 $\pm$ 0.12	Hernandez et al. (2014)
1154	16.7	12.2	II	M3.5 $\pm$ 2.0	0.27 $\pm$ 0.17	$V - J$ color
1155	13.3	10.6	II	K1.0 $\pm$ 2.5	1.71 $\pm$ 0.25	Hernandez et al. (2014)
1156	13.9	11.5	II	K5.0 $\pm$ 1.0	0.96 $\pm$ 0.16	Hernandez et al. (2014)
1182	17.7	13.0	II	M3.9 $\pm$ 2.0	0.22 $\pm$ 0.13	$V - J$ color
1193	19.8	14.2	II	M5.3 $\pm$ 2.0	0.10 $\pm$ 0.10	$V - J$ color
1230	18.2	13.4	II	M4.0 $\pm$ 2.0	0.19 $\pm$ 0.13	$V - J$ color
1248	18.0	12.6	II	M4.9 $\pm$ 2.0	0.16 $\pm$ 0.13	$V - J$ color
1260	16.9	12.8	II	M4.0 $\pm$ 0.5	0.21 $\pm$ 0.04	Rigliaco et al. (2012)
1266	18.2	13.5	II	M4.5 $\pm$ 0.5	0.15 $\pm$ 0.03	Rigliaco et al. (2012)
1267	15.0	11.4	TD	M1.0 $\pm$ 0.5	0.47 $\pm$ 0.06	Hernandez et al. (2014)
1268	20.8	14.7	TD	M4.5 $\pm$ 3.0	0.12 $\pm$ 0.12	Hernandez et al. (2014)
1274	14.4	11.1	II	K6.0 $\pm$ 1.0	0.81 $\pm$ 0.11	Hernandez et al. (2014)
1285	18.4	13.3	II	M5.0 $\pm$ 1.0	0.12 $\pm$ 0.05	Hernandez et al. (2014)
1327	16.6	12.3	II	M4.5 $\pm$ 2.5	0.19 $\pm$ 0.16	Hernandez et al. (2014)
1338	21.8	15.3	II	M6.4 $\pm$ 2.0	0.05 $\pm$ 0.06	$V - J$ color
1344	19.1	13.9	II	M4.6 $\pm$ 2.0	0.12 $\pm$ 0.12	$V - J$ color
1361	14.6	11.5	II	K7.5 $\pm$ 1.0	0.68 $\pm$ 0.15	Hernandez et al. (2014)
1362	18.5	13.1	II	M4.9 $\pm$ 2.0	0.14 $\pm$ 0.12	$V - J$ color
1369	13.7	10.6	II	K5.5 $\pm$ 1.0	0.85 $\pm$ 0.16	Hernandez et al. (2014)
247	18.3	13.5	II	M5.0 $\pm$ 0.5	0.12 $\pm$ 0.02	Hernandez et al. (2014)
254	21.4	15.2	II	M4.5 $\pm$ 3.5	0.11 $\pm$ 0.11	Hernandez et al. (2014)
271	19.8	14.2	II	M5.0 $\pm$ 1.0	0.10 $\pm$ 0.05	Hernandez et al. (2014)
299	16.7	12.8	TD	M2.5 $\pm$ 1.0	0.34 $\pm$ 0.09	Hernandez et al. (2014)
300	17.4	12.4	II	M4.5 $\pm$ 0.5	0.19 $\pm$ 0.04	Hernandez et al. (2014)
327	21.4	15.3	II	M4.5 $\pm$ 2.0	0.12 $\pm$ 0.09	Hernandez et al. (2014)
341	15.1	11.8	II	M0.0 $\pm$ 0.5	0.62 $\pm$ 0.09	Hernandez et al. (2014)
362	16.2	12.1	II	M2.5 $\pm$ 0.5	0.35 $\pm$ 0.03	Hernandez et al. (2014)
374	16.4	12.3	II	M3.0 $\pm$ 0.5	0.31 $\pm$ 0.05	Hernandez et al. (2014)
396	15.7	12.1	II	M1.5 $\pm$ 0.5	0.43 $\pm$ 0.05	Hernandez et al. (2014)
397	16.9	12.5	II	M4.5 $\pm$ 0.5	0.18 $\pm$ 0.03	Rigliaco et al. (2012)
411	10.4	9.4	TD	F7.5 $\pm$ 2.5	1.69 $\pm$ 0.18	Hernandez et al. (2014)
435	18.1	13.2	II	M5.0 $\pm$ 0.5	0.12 $\pm$ 0.03	Hernandez et al. (2014)
451	16.8	12.8	II	M2.5 $\pm$ 1.0	0.34 $\pm$ 0.09	Hernandez et al. (2014)
462	19.4	12.7	II	M4.0 $\pm$ 1.0	0.24 $\pm$ 0.07	Hernandez et al. (2014)
467	18.2	12.9	II	M5.5 $\pm$ 0.5	0.12 $\pm$ 0.02	Hernandez et al. (2014)
482	18.4	13.8	II	M3.8 $\pm$ 2.0	0.19 $\pm$ 0.12	$V - J$ color
485	18.4	13.7	II	M2.0 $\pm$ 1.0	0.36 $\pm$ 0.09	Hernandez et al. (2014)
490	18.6	13.4	II	M5.5 $\pm$ 0.5	0.10 $\pm$ 0.01	Rigliaco et al. (2012)
500	20.3	14.9	II	M6.0 $\pm$ 0.5	0.06 $\pm$ 0.01	Rigliaco et al. (2012)
514	19.7	14.1	II	M3.5 $\pm$ 1.0	0.23 $\pm$ 0.09	Hernandez et al. (2014)
518	14.2	12.0	II	K6.0 $\pm$ 1.0	0.85 $\pm$ 0.09	Hernandez et al. (2014)
520	17.2	12.8	II	M3.5 $\pm$ 0.5	0.26 $\pm$ 0.04	Hernandez et al. (2014)

537	20.8	14.8	II	M5.8 ± 2.0	0.06 ± 0.08	$V - J$ color
540	14.4	11.7	TD	K6.5 ± 1.5	0.79 ± 0.16	Hernandez et al. (2014)
562	16.4	12.2	II	M3.5 ± 1.5	0.27 ± 0.14	Hernandez et al. (2014)
563	15.8	11.5	II	K7.5 ± 0.5	0.66 ± 0.06	Hernandez et al. (2014)
583	12.1	10.1	II	K4.5 ± 1.5	1.03 ± 0.32	Hernandez et al. (2014)
587	16.4	12.0	II	M4.5 ± 0.5	0.20 ± 0.03	Rigliaco et al. (2012)
598	18.0	13.1	II	M2.0 ± 1.0	0.38 ± 0.09	Hernandez et al. (2014)
646	17.3	12.9	II	M3.5 ± 0.5	0.25 ± 0.04	Rigliaco et al. (2012)
657	21.8	14.9	II	M6.9 ± 2.0	0.04 ± 0.04	$V - J$ color
662	15.5	11.5	II	K7.0 ± 1.0	0.72 ± 0.12	Hernandez et al. (2014)
663	17.6	12.8	II	M4.2 ± 2.0	0.19 ± 0.13	$V - J$ color
674	17.1	12.8	II	M3.1 ± 2.0	0.30 ± 0.18	$V - J$ color
682	15.3	11.8	II	M0.5 ± 1.0	0.54 ± 0.14	Hernandez et al. (2014)
687	14.9	11.9	II	M1.0 ± 1.0	0.47 ± 0.13	Hernandez et al. (2014)
694	17.9	12.8	II	M4.5 ± 2.0	0.18 ± 0.13	$V - J$ color
697	14.0	11.4	II	K6.0 ± 0.5	0.82 ± 0.06	Hernandez et al. (2014)
707	18.8	13.4	II	M5.0 ± 2.0	0.12 ± 0.13	$V - J$ color
710	15.6	12.0	II	M1.5 ± 1.5	0.43 ± 0.17	Hernandez et al. (2014)
723	17.6	12.6	II	M4.0 ± 1.5	0.23 ± 0.11	Hernandez et al. (2014)
726	14.8	11.7	II	M0.5 ± 1.0	0.53 ± 0.14	Hernandez et al. (2014)
73	17.1	13.0	II	M2.0 ± 0.5	0.37 ± 0.04	Hernandez et al. (2014)
733	15.5	12.0	II	M1.0 ± 0.5	0.47 ± 0.06	Hernandez et al. (2014)
736	13.2	10.2	II	K6.0 ± 0.5	0.79 ± 0.06	Hernandez et al. (2014)
738	19.9	14.5	II	M5.0 ± 2.0	0.10 ± 0.10	$V - J$ color
739	19.8	14.1	II	M5.4 ± 2.0	0.10 ± 0.10	$V - J$ color
750	19.4	14.4	II	M4.5 ± 2.0	0.13 ± 0.10	$V - J$ color
754	18.0	13.0	II	M4.4 ± 2.0	0.18 ± 0.13	$V - J$ color
762	19.4	13.8	II	M5.3 ± 2.0	0.10 ± 0.10	$V - J$ color
774	14.3	11.5	II	K7.5 ± 1.0	0.68 ± 0.15	Hernandez et al. (2014)
818	15.6	12.3	TD	M0.0 ± 0.5	0.63 ± 0.09	Hernandez et al. (2014)
823	16.1	11.3	II	M2.0 ± 1.0	0.39 ± 0.08	Hernandez et al. (2014)
827	16.6	12.9	II	M2.5 ± 1.0	0.34 ± 0.10	Hernandez et al. (2014)
844	15.0	11.7	II	M0.5 ± 0.5	0.54 ± 0.07	Hernandez et al. (2014)
848	19.7	14.4	II	M4.0 ± 0.5	0.16 ± 0.04	Rigliaco et al. (2012)
859	16.5	12.4	II	M2.5 ± 0.5	0.35 ± 0.03	Hernandez et al. (2014)
865	16.9	12.8	II	M3.5 ± 1.0	0.26 ± 0.09	Hernandez et al. (2014)
866	18.8	13.8	II	M4.5 ± 1.0	0.14 ± 0.06	Hernandez et al. (2014)
871	16.4	14.0	II	M0.0 ± 1.5	0.55 ± 0.10	Hernandez et al. (2014)
897	14.0	11.3	TD	K6.5 ± 1.5	0.78 ± 0.18	Hernandez et al. (2014)
908	18.1	13.0	TD	M3.0 ± 1.0	0.31 ± 0.10	Hernandez et al. (2014)
927	15.7	12.0	II	M0.0 ± 1.0	0.62 ± 0.16	Hernandez et al. (2014)
936	20.7	15.2	II	M5.1 ± 2.0	0.08 ± 0.07	$V - J$ color
959	22.0	15.6	II	M6.4 ± 2.0	0.05 ± 0.05	$V - J$ color
967	17.7	13.3	II	M4.0 ± 0.5	0.20 ± 0.04	Hernandez et al. (2014)
984	14.4	11.4	II	K7.0 ± 0.5	0.74 ± 0.06	Hernandez et al. (2014)

On-source integration times were 120 sec per object to obtain an average continuum rms sensitivity of 0.15 mJy beam^{-1} (Table 2.5). This sensitivity was chosen based on the JCMT/SCUBA-2 survey of σ Orionis by Williams et al. (2013), who found in their stacked non-detections a mean 850 μm continuum signal of 1.3 mJy at 4σ significance. The sensitivity of our ALMA survey was therefore chosen to provide $\sim$3–4σ detections of such disks at 1.3 mm, based on an extrapolation of the 850 μm mean signal assuming a (sub-)mm spectral slope of $\alpha = 2$–3. The raw data were pipeline calibrated by NRAO staff using the `CASA` package (version 4.5.3). The pipeline calibration included: absolute flux calibration with observations of J0522-3627 or J0423-0120; bandpass calibration with observations of J0510+1800 or J0522-3627; and gain calibration with observations of J0532-0307. We estimate an absolute flux calibration error of 10% based on the amplitude variations of the gain calibrators over time.

We extract continuum and line images using standard routines in the `CASA` package. Continuum images are extracted from the calibrated visibilities by first averaging over the continuum channels using the *split* routine, then cleaning with a Briggs robust weighting parameter of +0.5 using the *clean* routine. This Briggs robust weighting parameter balances point source sensitivity and spatial resolution, giving an average beam size of $0\rlap{.}''31 \times 0\rlap{.}''25$ ($\sim$120$\times$95 AU at 385 pc). Of the 92 sources in our survey, only five are resolved; cleaning with a lower Briggs robust weighting parameter, which slightly increases spatial resolution at the cost of point-source sensitivity, does not result in additional resolved sources due to the compact nature of disks combined with the distance to σ Orionis.

We extract ^{12}CO, ^{13}CO, and C^{18}O $J = 2$–1 line channel maps from the calibrated visibilities by first subtracting the continuum level from the spectral windows containing line emission with the *uvcontsub* routine in `CASA`. We then image the visibilities using the *clean* routine; sources showing clear line emission are cleaned with a Briggs robust weighting parameter of +0.5 due to the faintness of the line emission. We find average rms sensitivities of 13, 14, and 11 mJy beam^{-1} within 1 km s^{-1} velocity channels for the ^{12}CO, ^{13}CO, and C^{18}O lines, respectively.
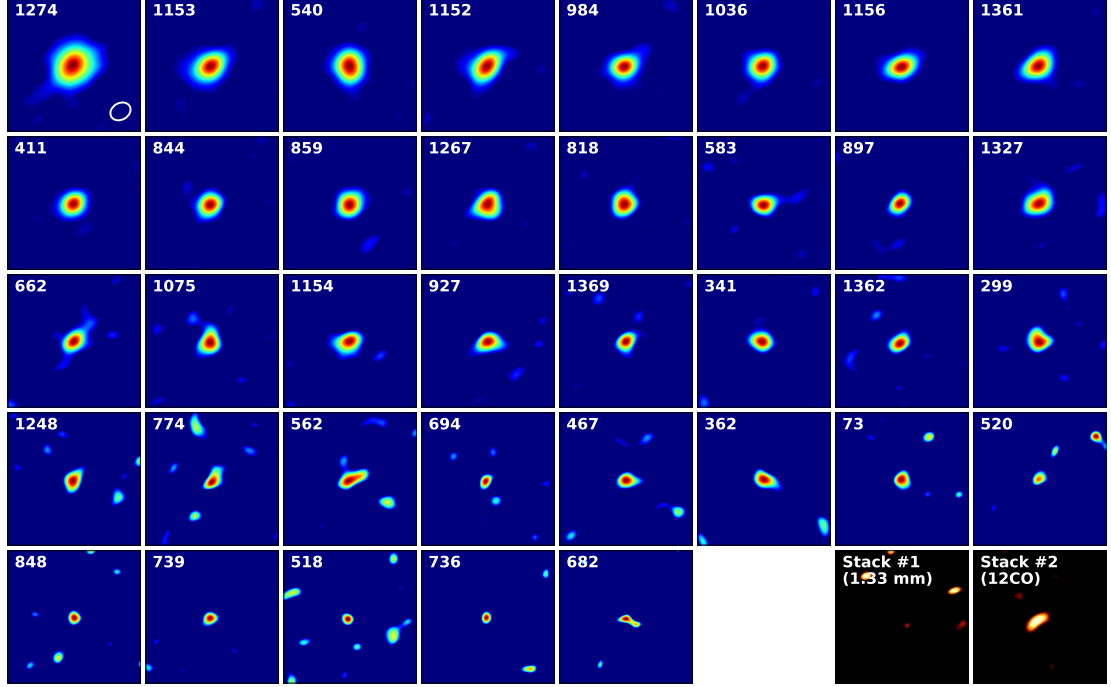
Figure 2.8 Continuum images at 1.33 mm of the 37 detected disks in our ALMA Cycle 3 survey of σ Orionis, ordered by decreasing flux density (as reported in Table 2.5). Images are $2'' \times 2''$ and the typical beam size of $0\rlap{.}''31 \times 0\rlap{.}''25$ (§2.3.3) is shown in the first panel. The last two panels show the stacked non-detections described in §2.3.6.

2.3.4 Dust Masses from 1.33 mm Continuum Emission

Nearly all sources in our σ Orionis sample are unresolved, thus we measure 1.33 mm continuum flux densities by fitting point-source models to the visibility data using the *uvmodelfit* routine in `CASA`. The point-source model has three free parameters: integrated flux density (F_λ), right ascension offset from the phase center ($\Delta\alpha$), and declination offset from the phase center ($\Delta\delta$). For the five resolved sources (1036, 1152, 1153, 1274, 540), we fit an elliptical Gaussian model instead, which has three additional free parameters: FWHM along the major axis (a), aspect ratio of the axes (r), and position angle (PA). Because the fits consistently produced $\chi^2_{\rm red} > 1$, we also scale the uncertainties on the fitted parameters by $\sqrt{\chi^2_{\rm red}}$, as recommended in the `CASA` documentation.

Table 2.5: σ Orionis ALMA Continuum Properties

ID	RA$_{\text{J2000}}$	Dec$_{\text{J2000}}$	$F_{1.33\text{mm}}$ (mJy)	rms (mJy beam^{-1})	M_{dust} ($M_{\oplus}$)
1036	05:39:25.206	-02:38:22.09	5.94 ± 0.15	0.16	26.45 ± 0.66
1050	05:39:26.330	-02:28:37.70	-0.15 ± 0.15	0.15	-0.67 ± 0.66
1075	05:39:29.350	-02:27:21.02	1.48 ± 0.15	0.16	6.57 ± 0.65
1152	05:39:39.377	-02:17:04.50	8.57 ± 0.17	0.18	38.16 ± 0.77
1153	05:39:39.828	-02:31:21.89	13.62 ± 0.16	0.18	60.66 ± 0.72
1154	05:39:39.833	-02:33:16.08	1.44 ± 0.15	0.16	6.43 ± 0.65
1155	05:39:39.900	-02:43:09.00	-0.12 ± 0.15	0.15	-0.54 ± 0.65
1156	05:39:40.171	-02:20:48.04	5.66 ± 0.15	0.18	25.21 ± 0.68
1182	05:39:43.190	-02:32:43.30	0.18 ± 0.15	0.15	0.82 ± 0.66
1193	05:39:44.510	-02:24:43.20	-0.02 ± 0.15	0.15	-0.09 ± 0.66
1230	05:39:49.450	-02:23:45.90	-0.02 ± 0.15	0.15	-0.10 ± 0.66
1248	05:39:51.728	-02:22:47.21	0.79 ± 0.15	0.16	3.52 ± 0.67
1260	05:39:53.630	-02:33:42.70	-0.12 ± 0.15	0.15	-0.52 ± 0.66
1266	05:39:54.210	-02:27:32.60	0.11 ± 0.15	0.16	0.47 ± 0.69
1267	05:39:54.275	-02:24:40.16	2.27 ± 0.15	0.17	10.13 ± 0.68
1268	05:39:54.330	-02:37:18.90	0.09 ± 0.15	0.15	0.42 ± 0.66
1274	05:39:54.659	-02:46:34.16	15.38 ± 0.25	0.16	68.48 ± 1.12
1285	05:39:56.460	-02:38:03.50	-0.01 ± 0.15	0.16	-0.03 ± 0.69
1327	05:40:01.958	-02:21:32.61	1.63 ± 0.16	0.16	7.25 ± 0.70
1338	05:40:04.540	-02:36:42.10	0.03 ± 0.15	0.15	0.14 ± 0.66
1344	05:40:05.260	-02:30:52.30	0.22 ± 0.15	0.16	0.99 ± 0.66
1361	05:40:08.888	-02:33:33.78	5.34 ± 0.15	0.16	23.79 ± 0.67
1362	05:40:09.336	-02:25:06.83	1.02 ± 0.15	0.17	4.55 ± 0.68
1369	05:40:12.863	-02:22:02.20	1.40 ± 0.15	0.17	6.22 ± 0.68
247	05:37:54.860	-02:41:09.20	-0.04 ± 0.13	0.14	-0.19 ± 0.59
254	05:37:55.600	-02:33:05.30	0.04 ± 0.13	0.13	0.18 ± 0.58
271	05:37:57.460	-02:38:44.40	0.03 ± 0.13	0.13	0.11 ± 0.58
299	05:38:00.975	-02:26:07.92	1.01 ± 0.14	0.15	4.52 ± 0.61
300	05:38:01.070	-02:45:38.00	-0.25 ± 0.13	0.13	-1.13 ± 0.59
327	05:38:05.520	-02:35:57.10	0.10 ± 0.13	0.13	0.46 ± 0.60
341	05:38:06.746	-02:30:22.74	1.19 ± 0.13	0.15	5.29 ± 0.59
362	05:38:08.263	-02:35:56.27	0.56 ± 0.13	0.15	2.51 ± 0.60
374	05:38:09.940	-02:51:37.70	0.12 ± 0.13	0.13	0.52 ± 0.58
396	05:38:13.160	-02:45:51.00	0.10 ± 0.13	0.13	0.45 ± 0.59
397	05:38:13.200	-02:26:08.80	-0.07 ± 0.14	0.14	-0.31 ± 0.62
411	05:38:14.123	-02:15:59.79	5.16 ± 0.13	0.15	22.96 ± 0.59
435	05:38:17.780	-02:40:50.10	0.17 ± 0.13	0.13	0.73 ± 0.59
451	05:38:18.860	-02:51:38.80	0.03 ± 0.13	0.13	0.15 ± 0.59
462	05:38:20.500	-02:34:09.00	0.18 ± 0.13	0.13	0.78 ± 0.59
467	05:38:21.201	-02:54:11.15	0.61 ± 0.13	0.14	2.70 ± 0.59
482	05:38:23.080	-02:36:49.40	0.29 ± 0.14	0.14	1.27 ± 0.61
485	05:38:23.330	-02:25:34.60	0.10 ± 0.13	0.13	0.43 ± 0.60
490	05:38:23.580	-02:20:47.60	0.05 ± 0.14	0.14	0.21 ± 0.62
500	05:38:25.440	-02:42:41.30	0.14 ± 0.13	0.14	0.61 ± 0.59
514	05:38:26.840	-02:38:46.10	0.17 ± 0.13	0.13	0.76 ± 0.59
518	05:38:27.256	-02:45:09.71	0.52 ± 0.13	0.15	2.30 ± 0.60

Table 2.5: (Continued) σ Orionis ALMA Continuum Properties

520	05:38:27.512	-02:35:04.28	0.52 ± 0.14	0.15	2.33 ± 0.60
537	05:38:28.970	-02:48:47.30	0.06 ± 0.13	0.14	0.26 ± 0.59
540	05:38:29.161	-02:16:15.76	10.69 ± 0.17	0.15	47.59 ± 0.77
562	05:38:31.420	-02:36:33.89	0.71 ± 0.13	0.15	3.17 ± 0.59
563	05:38:31.580	-02:35:14.90	0.06 ± 0.13	0.14	0.26 ± 0.59
583	05:38:33.691	-02:44:14.18	1.90 ± 0.13	0.14	8.47 ± 0.59
587	05:38:34.060	-02:36:37.50	0.19 ± 0.13	0.14	0.83 ± 0.60
598	05:38:34.600	-02:41:08.80	-0.19 ± 0.13	0.13	-0.84 ± 0.60
646	05:38:39.030	-02:45:32.20	0.08 ± 0.14	0.14	0.37 ± 0.60
657	05:38:39.760	-02:32:20.30	0.09 ± 0.14	0.14	0.41 ± 0.62
662	05:38:40.275	-02:30:18.61	1.54 ± 0.14	0.16	6.85 ± 0.62
663	05:38:40.540	-02:33:27.60	0.02 ± 0.14	0.15	0.09 ± 0.61
674	05:38:41.600	-02:30:28.90	0.01 ± 0.14	0.15	0.07 ± 0.64
682	05:38:42.277	-02:37:14.81	0.41 ± 0.14	0.15	1.84 ± 0.61
687	05:38:43.020	-02:36:14.60	0.15 ± 0.14	0.14	0.67 ± 0.63
694	05:38:43.872	-02:37:06.93	0.61 ± 0.14	0.15	2.70 ± 0.62
697	05:38:44.230	-02:40:19.70	-0.01 ± 0.14	0.14	-0.03 ± 0.62
707	05:38:45.280	-02:37:29.30	-0.08 ± 0.14	0.15	-0.37 ± 0.63
710	05:38:45.380	-02:41:59.40	-0.23 ± 0.14	0.15	-1.02 ± 0.62
723	05:38:47.190	-02:34:36.80	0.16 ± 0.15	0.15	0.71 ± 0.65
726	05:38:47.460	-02:35:25.20	0.02 ± 0.14	0.15	0.08 ± 0.63
73	05:37:30.956	-02:23:42.77	0.53 ± 0.13	0.14	2.37 ± 0.57
733	05:38:47.920	-02:37:19.20	-0.27 ± 0.14	0.15	-1.20 ± 0.62
736	05:38:48.035	-02:27:14.15	0.45 ± 0.14	0.15	1.99 ± 0.62
738	05:38:48.100	-02:28:53.60	-0.11 ± 0.14	0.14	-0.49 ± 0.63
739	05:38:48.218	-02:44:01.23	0.52 ± 0.14	0.15	2.31 ± 0.63
750	05:38:49.290	-02:23:57.60	-0.06 ± 0.15	0.15	-0.25 ± 0.65
754	05:38:49.700	-02:34:52.60	-0.05 ± 0.14	0.14	-0.24 ± 0.63
762	05:38:50.610	-02:42:42.90	-0.06 ± 0.14	0.14	-0.25 ± 0.63
774	05:38:52.009	-02:46:43.74	0.76 ± 0.14	0.15	3.38 ± 0.63
818	05:38:58.316	-02:16:10.15	1.97 ± 0.15	0.17	8.75 ± 0.68
823	05:38:59.110	-02:47:13.30	-0.03 ± 0.14	0.15	-0.14 ± 0.63
827	05:38:59.230	-02:33:51.40	-0.05 ± 0.14	0.14	-0.22 ± 0.63
844	05:39:01.370	-02:18:27.44	2.85 ± 0.14	0.16	12.68 ± 0.63
848	05:39:01.936	-02:35:02.87	0.52 ± 0.14	0.16	2.32 ± 0.64
859	05:39:02.977	-02:41:27.14	2.49 ± 0.14	0.16	11.08 ± 0.64
865	05:39:03.570	-02:46:27.00	0.18 ± 0.14	0.15	0.78 ± 0.64
866	05:39:03.870	-02:20:08.20	0.10 ± 0.15	0.16	0.47 ± 0.66
871	05:39:04.590	-02:41:49.40	0.12 ± 0.14	0.14	0.53 ± 0.64
897	05:39:07.606	-02:32:39.20	1.71 ± 0.14	0.15	7.63 ± 0.64
908	05:39:08.780	-02:31:11.50	0.09 ± 0.15	0.15	0.42 ± 0.65
927	05:39:11.519	-02:31:06.55	1.41 ± 0.15	0.15	6.27 ± 0.67
936	05:39:13.080	-02:37:50.90	0.09 ± 0.15	0.14	0.39 ± 0.65
959	05:39:15.260	-02:21:50.70	0.04 ± 0.15	0.16	0.18 ± 0.67
967	05:39:15.830	-02:36:50.70	0.21 ± 0.14	0.15	0.92 ± 0.64
984	05:39:18.838	-02:30:53.22	6.07 ± 0.15	0.17	27.03 ± 0.66
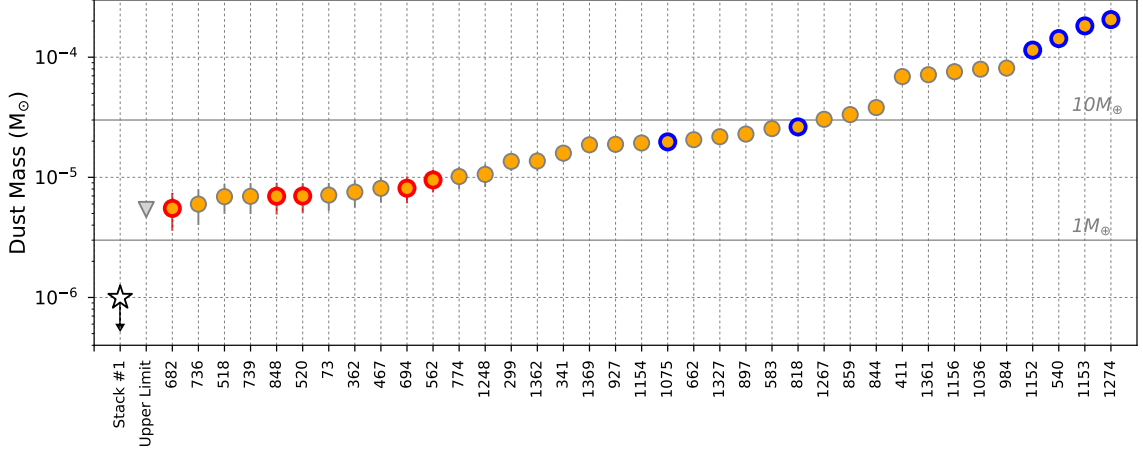
Figure 2.9 Dust masses for the 37 continuum-detected sources in our σ Orionis ALMA survey. Dust masses are from Table 2.5 and error bars (typically smaller than the symbols) include the 10% absolute flux calibration uncertainty (§2.3.3). The downward-facing triangle is the typical 3σ upper limit for individual non-detections, while the star shows their average constraint from the stacked non-detections ("Stack #1" in §2.3.6). Sources outlined in blue are also detected in ^{12}CO (§2.3.5) and sources outlined in red are located $\lesssim 0.5$ pc from the central OB system (§3.3).

Table 2.5 presents our 1.33 mm continuum flux densities ($F_{1.33\mathrm{mm}}$), where the uncertainties are statistical errors, thus do not include the 10% absolute flux calibration error (§2.3.3). We detect 37 out of the 92 observed sources at $>3\sigma$ significance; Figure 2.8 shows the continuum images for the detected sources. Table 2.5 provides the fitted source locations output by *uvmodelfit* for the detections, or the phase centers of the ALMA observations (i.e., 2MASS positions) for the non-detections. The average offset from the phase center for detections is $\Delta\alpha = 0\farcs057$ and $\Delta\delta = -0\farcs096$ (i.e., smaller than the average beam size). We note that only 5 out of the 37 continuum detections have photometrically derived spectral types, which are less accurate than those derived from spectra (§2.3.2).

Table 2.5 gives our M_{dust} estimates, derived by inputting our $F_{1.33\mathrm{mm}}$ measurements into Equation 2.1. Figure 2.9 shows the continuum-detected disks in order of increasing M_{dust} as well as the typical 3σ upper limit of $\sim$2.0 $M_\oplus$. Only 4 disks have $M_{\mathrm{dust}} > 30$ $M_\oplus$, thus nearly all protoplanetary disks in σ Orionis have dust masses well below the MMSN

(Weidenschilling 1977). Moreover, only 11 disks have $M_{\rm dust} > 10\ M_{\oplus}$, thus by $\sim$3–5 Myr most protoplanetary disks lack sufficient dust reservoirs to form giant planet cores.

2.3.5 Gas Masses from CO $J = 2$–1 Line Emission

To search for objects exhibiting significant line emission, we first extract the ^{12}CO spectrum for each source. When creating the spectrum, we use 1 km s^{-1} velocity sampling and measure fluxes in each channel using a circular aperture that is $0\rlap{.}''30$ in diameter and centered on the continuum emission (for detections) or the expected stellar position (for non-detections). We measure the image rms using a 4–9$''$ radius annulus centered on the fitted or expected source position. Candidate detections are identified as those with emission exceeding 3$\times$ the rms in multiple nearby channels within 0–25 km s^{-1} (LSRK frame), which covers the range of RVs found for σ Orionis members (e.g., Jeffries et al. 2006).

For each candidate detection, we create zero-moment maps by integrating across the velocity range where the emission exceeds the noise. The integrated flux density ($F_{\rm 12CO}$) is then measured using circular aperture photometry, where the aperture size for each source is determined by a curve-of-growth method in which successively larger apertures are applied until the flux density stabilizes to within errors. Uncertainties ($E_{\rm 12CO}$) are estimated by taking the standard deviation of the flux densities measured within the same-sized aperture placed randomly within the field of view but away from the source. We consider sources as detections when $F_{\rm 12CO} > 4 \times E_{\rm 12CO}$. We adopt this high detection threshold because this procedure selects both the velocity range and aperture size that maximize the signal, thus can produce false detections at lower significance levels. We detect only six sources in ^{12}CO using this procedure. For these sources, we also search for ^{13}CO and C^{18}O emission using the same velocity range and aperture photometry method as for ^{12}CO; we detect three of these sources in ^{13}CO and none in C^{18}O.

For sources with no significant line emission found using the above procedure, we create zero-moment maps by integrating across the channels ±1 km s^{-1} from their known RVs, when available in the literature (Maxted et al. 2008; Sacco et al. 2008). For sources

with unknown RVs, we integrate around the average value for σ Orionis members with known RVs. Jeffries et al. (2006) showed that σ Orionis members are divided into two kinematically distinct subgroups differentiated by their RVs (Group 1 and 2, by their convention). However, the region is dominated by Group 2 sources at $\delta < -02{:}18{:}00$, where all our gas non-detections with unknown RVs are located. Thus we adopt the average RV of Group 2 (13 km s^{-1} in the LSRK frame) when creating zero-moment maps for our gas non-detections with unknown RVs. We measure ^{12}CO, ^{13}CO, and C^{18}O integrated flux densities from these zero-moment maps using the aforementioned aperture photometry method, but with an aperture size fixed to the beam size. We found no additional detections, thus took upper limits as $3\times$ the image rms.

Table 2.6 gives our integrated line flux densities or upper limits. Of the 92 targets, six are detected in ^{12}CO, three are detected in ^{13}CO, and none are detected in C^{18}O with $>4\sigma$ significance. All sources detected in ^{12}CO are detected in the continuum, and all sources detected in ^{13}CO are detected in ^{12}CO. The zero- and first-moment maps of the gas detections are shown in Figure 2.10. Unfortunately, because we find no C^{18}O detections in σ Orionis, we cannot use the same combination of CO isotopologue lines to estimate M_{gas} in this region, as we did for Lupus (§2.2.5). However, we can still place rough constraints on M_{gas} by comparing our measured ^{12}CO and ^{13}CO line luminosities or upper limits to the WB14 model grid. The uncertainties on M_{gas} are larger for this line combination because ^{12}CO is optically thick and therefore more sensitive to other disk parameters, such as the temperature profile. Nevertheless, M_{gas} can still be estimated using this method because the combination of integrated line fluxes still primarily depends on bulk gas mass rather than these other disk parameters (see the parameter exploration described in WB14 as well as the separation of gas masses in Figure 2.11).

Table 2.6 provides our M_{gas} constraints derived from comparing our measured ^{12}CO and ^{13}CO line luminosities or upper limits to the WB14 model grid; Figure 2.11 illustrates this comparison for sources detected in at least one of these lines. To estimate M_{gas} for the three sources detected in both ^{12}CO and ^{13}CO (540, 1274, 1152), we calculate the geometric
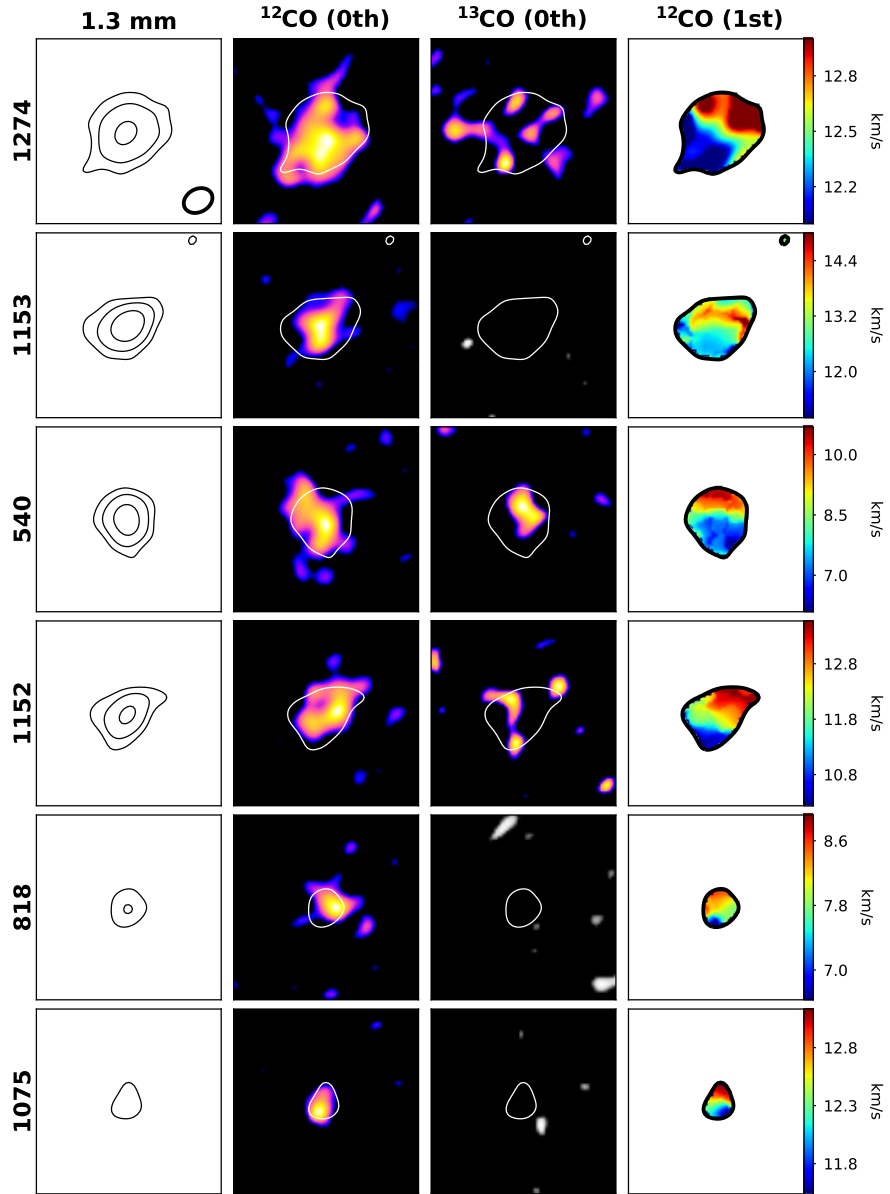
Figure 2.10 The six sources in our σ Orionis ALMA survey detected in CO (§2.3.5). The first column shows the 1.33 mm continuum emission in 4σ, 10σ, and 25σ contours. The second and third columns show the ^{12}CO and ^{13}CO zero-moment maps with 4σ continuum contours. The last column shows the ^{12}CO first-moment maps within 4σ continuum contours. Images are $2'' \times 2''$ and the typical beam size of $0\rlap{.}''31 \times 0\rlap{.}''25$ (§2.3.3) is shown in the first panel.

Table 2.6: σ Orionis ALMA CO Line Properties

ID	F_{12CO} (mJy km s^{-1})	F_{13CO} (mJy km s^{-1})	F_{C18O} (mJy km s^{-1})	M_{gas} (M_{Jup})	$M_{\mathrm{gas,min}}$ (M_{Jup})	$M_{\mathrm{gas,max}}$ (M_{Jup})
1036	< 72	< 81	< 57			3.1
1050	< 72	< 81	< 60			3.1
1075	165 ± 33	< 93	< 66			10.5
1152	633 ± 82	314 ± 65	< 60	7.1	1.0	31.4
1153	557 ± 57	< 99	< 72			1.0
1154	< 69	< 75	< 57			3.1
1155	< 69	< 78	< 57			3.1
1156	< 72	< 84	< 60			3.1
1182	< 69	< 78	< 60			3.1
1193	< 72	< 81	< 60			3.1
1230	< 72	< 81	< 57			3.1
1248	< 72	< 81	< 60			3.1
1260	< 69	< 78	< 60			3.1
1266	< 72	< 84	< 60			3.1
1267	< 69	< 84	< 63			3.1
1268	< 72	< 84	< 60			3.1
1274	861 ± 88	326 ± 68	< 48	5.5	1.0	31.4
1285	< 75	< 81	< 63			3.1
1327	< 75	< 87	< 66			10.5
1338	< 72	< 81	< 60			3.1
1344	< 69	< 78	< 60			3.1
1361	< 72	< 81	< 60			3.1
1362	< 72	< 78	< 60			3.1
1369	< 72	< 78	< 63			3.1
247	< 66	< 75	< 54			3.1
254	< 66	< 75	< 54			3.1
271	< 66	< 75	< 51			3.1
299	< 66	< 78	< 54			3.1
300	< 66	< 75	< 57			3.1
327	< 66	< 78	< 57			3.1
341	< 66	< 75	< 54			3.1
362	< 69	< 75	< 54			3.1
374	< 66	< 78	< 54			3.1
396	< 63	< 78	< 54			3.1
397	< 69	< 81	< 60			3.1
411	< 69	< 75	< 54			3.1
435	< 66	< 75	< 57			3.1
451	< 63	< 75	< 54			3.1
462	< 69	< 75	< 51			3.1
467	< 66	< 75	< 54			3.1
482	< 69	< 78	< 57			3.1
485	< 63	< 75	< 54			3.1
490	< 72	< 78	< 54			3.1
500	< 63	< 72	< 51			3.1
514	< 66	< 78	< 54			3.1
518	< 69	< 75	< 60			3.1

Table 2.6: (Continued) σ Orionis ALMA CO Line Properties

520	< 69	< 75	< 57		3.1
537	< 66	< 75	< 54		3.1
540	1204 ± 85	276 ± 54	< 78	2.4	1.0	10.5
562	< 63	< 75	< 54		3.1
563	< 69	< 75	< 54		3.1
583	< 66	< 75	< 54		3.1
587	< 66	< 75	< 54		3.1
598	< 66	< 75	< 57		3.1
646	< 69	< 78	< 57		3.1
657	< 69	< 78	< 57		3.1
662	< 69	< 75	< 54		3.1
663	< 69	< 75	< 54		3.1
674	< 69	< 78	< 57		3.1
682	< 69	< 75	< 57		3.1
687	< 69	< 78	< 57		3.1
694	< 69	< 75	< 57		3.1
697	< 72	< 72	< 57		3.1
707	< 69	< 75	< 60		3.1
710	< 69	< 78	< 57		3.1
723	< 72	< 81	< 60		3.1
726	< 72	< 81	< 57		3.1
73	< 66	< 75	< 54		3.1
733	< 69	< 78	< 57		3.1
736	< 69	< 78	< 57		3.1
738	< 66	< 81	< 54		3.1
739	< 69	< 75	< 57		3.1
750	< 72	< 81	< 60		3.1
754	< 69	< 78	< 60		3.1
762	< 66	< 75	< 54		3.1
774	< 69	< 72	< 54		3.1
818	514 ± 58	< 108	< 81		1.0
823	< 72	< 75	< 57		3.1
827	< 69	< 78	< 57		3.1
844	< 69	< 81	< 57		3.1
848	< 66	< 81	< 57		3.1
859	< 69	< 78	< 57		3.1
865	< 69	< 81	< 57		3.1
866	< 72	< 84	< 57		3.1
871	< 66	< 78	< 57		3.1
897	< 69	< 81	< 60		3.1
908	< 69	< 81	< 60		3.1
927	< 72	< 87	< 60		3.1
936	< 72	< 78	< 57		10.5
959	< 72	< 84	< 60		3.1
967	< 72	< 81	< 60		3.1
984	< 69	< 81	< 60		3.1

mean of the WB14 model grid points consistent with our measured line luminosities and their associated errors; these values span 2–7 $M_{\rm Jup}$. We also set upper ($M_{\rm gas,max}$) and lower ($M_{\rm gas,min}$) limits based on the maximum and minimum WB14 model grid points consistent with the data, respectively. For the three sources with ^{12}CO detections and ^{13}CO upper limits (1153, 818, 1075) we provide only $M_{\rm gas,max}$, since at these very low disk masses isotope-selective photodissociation becomes important (Miotello et al. 2017). For the 86 sources undetected in both lines, we give only $M_{\rm gas,max}$, set by the maximum WB14 model grid point consistent with the upper limits on both lines.

The disk gas masses in σ Orionis appear to be very low, with the vast majority of systems below our detection threshold of $\sim$3 $M_{\rm Jup}$, pointing to significant gas evolution in disks by $\sim$3–5 Myr of age. We discuss the implications and potential caveats in §3.2.

2.3.6 Stacking Analysis

We perform a stacking analysis to constrain the average dust and gas mass of the individually undetected sources in our σ Orionis sample. To stack the images, we first center them on their expected source locations, then average them in the image plane and search for emission using the aperture photometry method described in Section 2.3.5. We also check these image stacking results using averages of the individual photometry measurements presented in Table 2.5.

We first stack the 55 sources undetected in the continuum ("Stack #1"), but do not find a significant mean signal in the continuum or any of the CO lines. The measured continuum mean signal is 0.05±0.03 mJy (1.7σ) and the stacked image is shown in the bottom right of Figure 2.8. We confirm this non-detection by calculating the mean and standard error on the mean of the continuum fluxes reported in Table 2.5, which similarly gives 0.03±0.02 mJy (1.5σ). This provides a 3σ upper limit on the average dust mass of individually undetected continuum sources of 0.4 $M_\oplus$, which is 5× lower than the smallest dust mass among the continuum-detected sources in σ Orionis (see Figure 2.9). This striking difference in the dust masses of detected and undetected continuum sources was also seen in
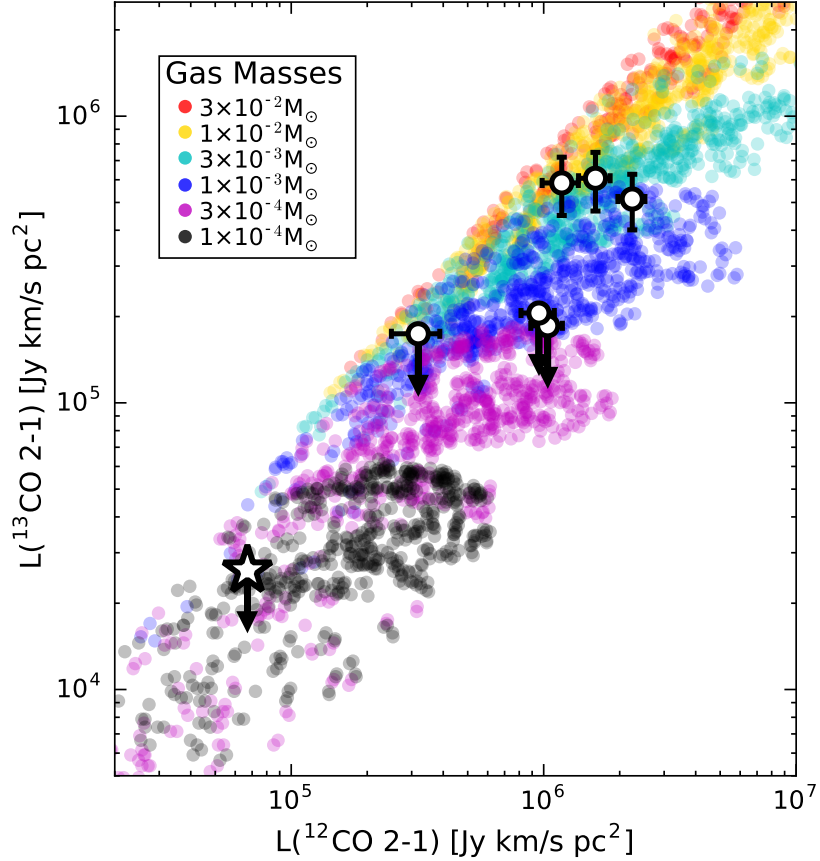
Figure 2.11 ^{12}CO and ^{13}CO $J = 1$–2 line luminosities for determining gas masses (§2.3.5). The WB14 model grid is color-coded by gas mass. The three disks with both lines detected are plotted as white circles, and the three disks with only ^{12}CO detections are plotted as white circles with arrows indicating 3σ upper limits on ^{13}CO. Error bars account for the statistical errors given in Table 2.6 as well as the 10% absolute flux calibration error. The star shows the location of "Stack #2" (§2.3.6); error bars are smaller than the symbol.

our ALMA survey of Lupus (Figure 2.5) and supports theoretical photoevaporation models that predict protoplanetary disks dispersing rapidly once disk clearing begins (e.g., see review in Alexander et al. 2014).

We also stack the 31 sources that are detected in the continuum but undetected in ^{12}CO ("Stack #2"), finding a mean continuum signal of 2.29 ± 0.09 mJy as well as a significant mean ^{12}CO signal of 36 ± 8 km s^{-1} (4.5σ; see bottom right panel of Figure 2.8). No emission is detected in the ^{13}CO or C^{18}O lines with 3σ upper limits of 14 and 11 mJy km s^{-1}, respectively. The continuum flux corresponds to $M_{\rm dust} \sim 10\ M_{\oplus}$, while the ^{12}CO detection

and ^{13}CO upper limit correspond to $M_{\mathrm{gas}} < 1.0\ M_{\mathrm{Jup}}$ using the WB14 model grid (the ^{13}CO and C^{18}O upper limits also correspond to $M_{\mathrm{gas}} < 1.0\ M_{\mathrm{Jup}}$). This gives an average gas-to-dust ratio of < 30 for sources detected in the continuum but not the CO lines.

2.4   Other Star-forming Regions

The protoplanetary disk populations in several other star-forming regions have been surveyed in the (sub-)mm continuum at sensitivities similar to our Lupus and σ Orionis surveys. We briefly describe these regions and their surveys below, as we use their (sub-)mm continuum flux densities to estimate disk dust masses in the next chapter in order to expand our study of disk dust evolution.

2.4.1   Taurus: The Prototypical Young Star-forming Region

Taurus is the prototypical low-mass star-forming region in the northern sky, as evidenced by the "T Tauri" designation for optically visible PMS stars (Joy 1945). At a distance of only $\sim$140 pc, the region contains several hundred young ($\sim$1–3 Myr) YSOs that have been extensively studied from X-ray to radio wavelengths (see review in Kenyon et al. 2008). The survey of the 179 Class II disks in Taurus (complete for stars with spectral types earlier than M8.5) using pre-ALMA facilities at 850 μm and 1.3 mm (Andrews & Williams 2005; Andrews et al. 2013) has become a benchmark study of disk dust masses at the early stages of disk evolution. The region has not yet been uniformly studied by ALMA (partly due to its northern location in the sky, which is not ideal for ALMA observations), thus the (sub-)mm continuum sensitivities for Taurus disks remain limited, corresponding to dust mass limits of just $\sim$1 $M_{\oplus}$. Moreover, the angular resolutions are poor compared to current ALMA observations ($\gg 1''$), which means that binary disks are typically unresolved.

Nevertheless, the protoplanetary disk population in Taurus is a valuable point of comparison to those in Lupus and σ Orionis. Although Taurus has a similar age to Lupus and its pre-ALMA (sub-)mm survey is hindered by what is now considered to be poor

continuum sensitivities, the region hosts $\sim2\times$ as many protoplanetary disks compared to Lupus and thus still provides statistically significant results that can be used to study disk evolution. In particular, by comparing Taurus to Lupus, we can search for differences in disk populations due to environment rather than age.

2.4.2   Upper Sco: An Evolved Disk Population

The Upper Scorpius association (Upper Sco) is the closest star-forming region with an evolved age (5–11 Myr; Preibisch et al. 2002; Pecaut et al. 2012) that is comparable to the disk dispersal timescale (e.g., see Figure 1.2), making it an important point of comparison for disk evolution studies. Its nearby distance of 145 pc (de Zeeuw et al. 1999) also means that the weak (sub-)mm emission from these presumably more evolved disks can be detected within reasonable integration times using ALMA.

Upper Sco has been surveyed with ALMA in the Band 7 (880 μm) continuum and CO $J = 3$–2 line. Carpenter et al. (2014) first observed an initial sample of 20 disks in ALMA Cycle 0 with angular resolutions of $\sim0\rlap{.}''55$. In ALMA Cycle 2, Barenfeld et al. (2016) completed the sample of 106 disk-hosting stars with stellar masses $\gtrsim 0.14 \; M_\odot$ with angular resolutions of $\sim0\rlap{.}''34$ and continuum rms noise values of ~0.15 mJy. This sample includes the 75 "primordial" disks (encompassing "full", "transitional", and "evolved" disks) and the 31 "debris/evolved transitional" disks classified by Luhman & Mamajek (2012) based on WISE excess emission; the former category is analogous to the Class II sources hosting protoplanetary disks observed in our Lupus and σ Orionis ALMA surveys, whereas the latter category likely consists of end-stage Class III disks or second-generation disks made from dust originating from collisions of larger bodies. Thus we only compare the 75 primordial disks in Upper Sco to our Lupus and σ Orionis surveys.

2.4.3   Chamaeleon I: Another Young Disk Population

Chamaeleon I is another young (~2–3 Myr) and nearby (160 pc) star-forming region (see review in Luhman 2008). During the course of this thesis, its protoplanetary disk population

was observed in ALMA Band 7 (887 μm) by Pascucci et al. (2016). Their sample of 93 protoplanetary disks (82 Class II, 8 TD, 3 flat-spectrum) is complete to the substellar limit. The continuum sensitivities were $\sim$1.0 mJy beam^{-1} for the higher-mass stars (M3 and earlier) and $\sim$0.2 mJy beam^{-1} for the lower-mass stars.

Chapter 3

Evidence of Protoplanetary Disk Evolution

Initial evidence of protoplanetary disk evolution came from the first large-scale surveys of star-forming regions at (sub-)mm wavelengths using pre-ALMA facilities such as the SMA, JCMT, and IRAM (e.g., Beckwith et al. 1990; Andrews & Williams 2005; Mann & Williams 2009; Andrews et al. 2013; Williams et al. 2013; Ansdell et al. 2015). Due to observational limitations, these surveys were often incomplete and hampered by dust mass sensitivities of a few Earth masses; these constraints meant that it remained unclear whether (sub-)mm continuum emission systematically declines with age, reflecting steady disk dispersal and/or grain growth (Williams 2012). Moreover, none of these surveys probed disk gas mass, as pre-ALMA facilities lacked the sensitivity to detect faint line emission in most disks.

In this chapter, we use our ALMA surveys of Lupus and σ Orionis (§2) to provide new insights into disk evolution. We use our continuum measurements to demonstrate that disk dust masses do indeed clearly decline with age. We also confirm the positive relation between M_{dust} and $M_{\star}$ (initially suggested in pre-ALMA surveys of Taurus; Natta et al. 2000; Andrews et al. 2013), and show for the first time that this relation steepens with age. We then present evidence of rapid gas dispersal based on our CO line measurements, and also consider the alternative scenario of carbon depletion. Finally, we show that the effects of external photoevaporation for disks in OB clusters appear to be much more extensive than previously thought. Studying these evolutionary trends is key to distinguishing between competing disk processes as well as explaining trends seen in the exoplanet population.

3.1 Trends in Disk Dust Distributions

In this section, we compare the disk dust mass distributions in star-forming regions at distinct ages in order to quantitatively trace the bulk evolution of solids in protoplanetary disks. Our ALMA survey of the young ($\sim$1–3 Myr) Lupus complex (§2.2) characterizes early disk conditions, while our ALMA survey of the middle-aged ($\sim$3–5 Myr) σ Orionis cluster (§2.3) gives conditions near the median disk lifetime. From the literature, we use the ALMA survey of Upper Sco (§2.4.2; Barenfeld et al. 2016), as its evolved age ($\sim$5–10 Myr) is similar to the disk dispersal timescale, providing another important point for comparison. Additionally, we include the disk surveys of Taurus (Andrews et al. 2013) and Chamaeleon I (Pascucci et al. 2016); although their young ($\sim$1–3 Myr) ages are similar to that of Lupus, these regions are useful for testing the universality of disk trends across different environments and stellar populations. We note that although absolute cluster ages are uncertain and possibly underestimated (Bell et al. 2013), relative ages are robust and thus sufficient for our study.

We calculate disk dust masses uniformly across each region by inputting the (sub-)mm continuum fluxes (or 3σ upper limits) reported by each survey into Equation 2.1, scaled to the distances of the clusters and the observation wavelengths of the surveys. We adopt distances of 150 or 200 pc for Lupus, 385 pc for σ Orionis, 145 pc for Upper Sco, 160 pc for Chamaeleon I, and 140 pc for Taurus (see §2 for references). We consider only sources with $M_\star \geq 0.1\ M_\odot$ in order to exclude brown dwarfs, while also maintaining a common stellar mass limit among the surveys. Stellar masses were derived using the Siess et al. (2000) evolutionary tracks for all regions except Chamaeleon I, for which the Baraffe et al. (2015) models were employed in Pascucci et al. (2016); the stellar masses derived using these two model grids are generally consistent, thus any effects should be negligible.

These samples of disk dust masses (and associated host star masses) are used in the following sub-sections to identify and analyze trends in the bulk evolution of solids in protoplanetary disks.

56
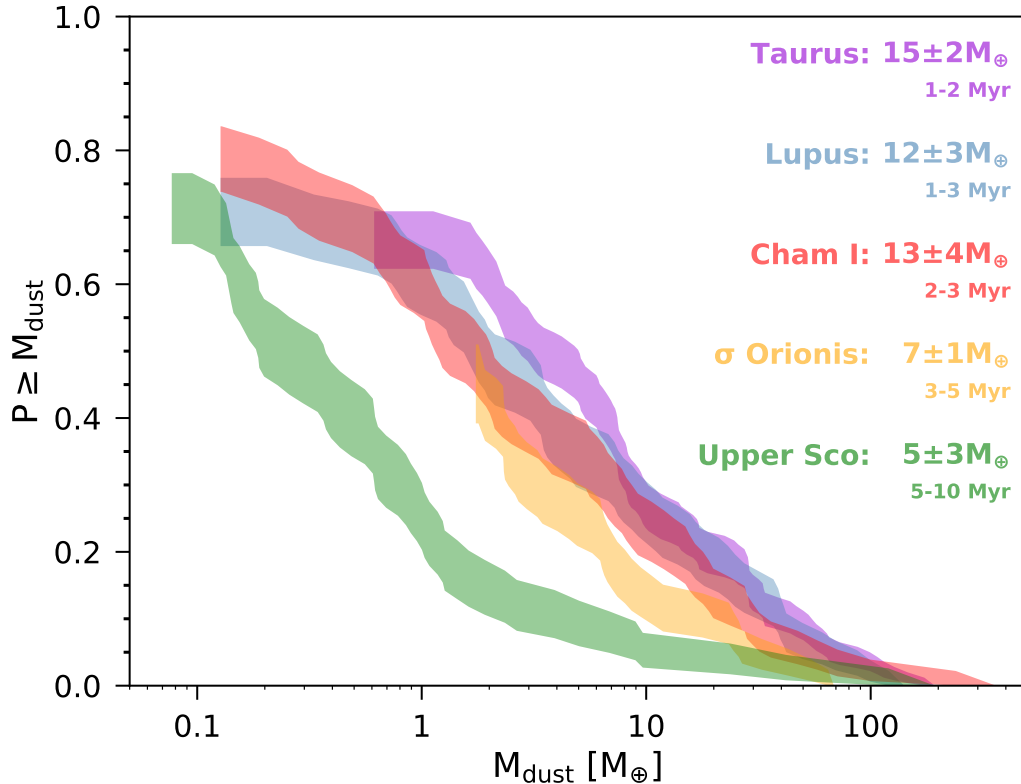
Figure 3.1 Disk dust mass ($M_{\rm dust}$) cumulative distributions in Taurus, Lupus, Chamaeleon I, σ Orionis, and Upper Sco. The average $M_{\rm dust}$ value and age for each region are given for reference. The distributions and their 1σ confidence intervals are calculated using the Kaplan-Meier estimator in `ASURV` (Lavalley et al. 1992) to properly account for upper limits. The $M_{\rm dust}$ distributions of σ Orionis, Lupus, and Upper Sco can be directly compared, as these regions have similar stellar mass distributions; caution should be taken when comparing the $M_{\rm dust}$ distributions in Taurus and Chamaeleon I to those of the other regions due to their potentially different stellar mass distributions (see discussion in §3.1.1).

3.1.1   Declining Disk Dust Masses

Disk dispersal and grain growth should be reflected in a decline with age of the bulk dust mass probed by (sub-)mm continuum flux. Figure 3.1 shows the $M_{\rm dust}$ cumulative distributions for the five star-forming regions considered in this study, calculated using the Kaplan-Meier estimator in the `ASURV` package (Lavalley et al. 1992) to properly account for upper limits. Ideally we would compare the medians of these distributions, however the lower $M_{\rm dust}$ sensitivity of our σ Orionis survey (due to its much further distance) prohibits

this comparison. Instead we compare mean dust masses ($\overline{M}_{\rm dust}$) calculated again with the Kaplan-Meier estimator to account for upper limits. Taurus, Lupus, and Chamaeleon I have consistent $\overline{M}_{\rm dust}$ values (15 ± 2, 12 ± 3, and 13 ± 4 $M_\oplus$, respectively), which is in line with their similarly young ages. The older σ Orionis and Upper Sco regions have significantly lower $\overline{M}_{\rm dust}$ values (7 ± 1 and 5 ± 3 $M_\oplus$, respectively), presumably due to their several Myr of additional disk evolution. Although the $\overline{M}_{\rm dust}$ values of σ Orionis and Upper Sco are statistically indistinguishable, the $M_{\rm dust}$ distributions of these regions are clearly distinct in Figure 3.1. Indeed, the overall picture from Figure 3.1 is a clear decline in $M_{\rm dust}$ with age. These results are reported in Ansdell et al. (2016c) and Ansdell et al. (2017).

When comparing the $M_{\rm dust}$ distributions of two regions, it is important to confirm that they have similar $M_\star$ distributions due to the dependence of $M_{\rm dust}$ on $M_\star$ (see §3.1.2). Thus we employ the two-sample tests in the ASURV package (longrank test, Peto-Prentice Generalized Wilcoxon test, Peto & Peto Generalized Wilcoxon test, and two versions of the Gehan Generalized Wilcoxon test) to determine the probabilities that the stellar masses in each region are drawn from the same parent population. Using σ Orionis as the comparison standard, we find that the $M_\star$ distributions are statistically indistinguishable for σ Orionis and Lupus ($p = 0.45$–0.96), σ Orionis and Chamaeleon I ($p = 0.06$–0.22), and σ Orionis and Upper Sco ($p = 0.21$–0.30). However we find statistically distinct $M_\star$ distributions for σ Orionis and Taurus ($p = 0.03$–0.04); this distinction from Taurus is also found for the stellar populations of Lupus and Upper Sco ($p = 0.0001$–0.04), while Chamaeleon I has a very similar ($p = 0.99$) stellar population to Taurus. Thus in Figure 3.1 we can directly compare the dust mass distributions of σ Orionis, Lupus, and Upper Sco; caution should be taken, however, when comparing Taurus and Chamaeleon I to the other regions in Figure 3.1 due to their potentially different stellar mass distributions. Nevertheless, our conclusion in the previous paragraph of a clear decline in $M_{\rm dust}$ with age remains robust.

Alternatively, to account for the different stellar populations among star-forming regions, we could instead compare the $M_{\rm dust}/M_\star$ distributions (e.g., Barenfeld et al. 2016) or employ an MC approach that aims to normalize the stellar mass selection functions (e.g., Andrews

et al. 2013; Williams et al. 2013; Ansdell et al. 2016c). However, in this work we do not attempt these more detailed analyses due to the large uncertainties on the many $M_\star$ estimates that were derived from photometry (e.g., all of the stars in Upper Sco and 23 stars in σ Orionis).

3.1.2 The $M_{\rm dust}$–$M_\star$ Relation

Pre-ALMA surveys of protoplanetary disks in Taurus (Natta et al. 2000; Andrews et al. 2013) first identified the potential dependence of disk dust mass on host-star mass. This $M_{\rm dust}$–$M_\star$ relation is important because it could fundamentally explain the positive correlation between giant planet frequency and stellar mass (Endl et al. 2006; Johnson et al. 2007; Bowler et al. 2010; Bonfils et al. 2013); this is because the cores of giant planets theoretically form more efficiently both in higher-mass disks (e.g., Thommes et al. 2008; Mordasini et al. 2012) and around higher-mass stars (e.g., Kennedy & Kenyon 2008) (see §4.1 for a detailed discussion). Moreover, tracking the evolution of the $M_{\rm dust}$–$M_\star$ relation with age can inform whether disk evolution proceeds differently around low-mass stars compared to high-mass stars, which in turn can help to constrain the relative importance of competing disk processes during key epochs of planet formation (e.g., Pascucci et al. 2016).

Confirmation of the $M_{\rm dust}$–$M_\star$ relation in other regions apart from Taurus has until recently remained elusive. This is because finding a statistically significant correlation requires high-sensitivity observations of a large sample of disks spanning a large range in host star mass. Indeed, parameterizing the $M_{\rm dust}$–$M_\star$ relation is complicated by three main factors: 1) measurement uncertainties on both variables, 2) intrinsic scatter in the data, and 3) upper limits on $M_{\rm dust}$. The procedure most often utilized in the disk survey literature to fit the $M_{\rm dust}$–$M_\star$ relation is the Bayesian linear regression method of Kelly (2007), as it accounts for these three key factors simultaneously, unlike other linear regression methods (see Pascucci et al. 2016 for a detailed discussion). For a given dataset, the Kelly (2007) procedure fits a slope (β), intercept (α), and intrinsic dispersion (δ) with associated uncertainties on each parameter.
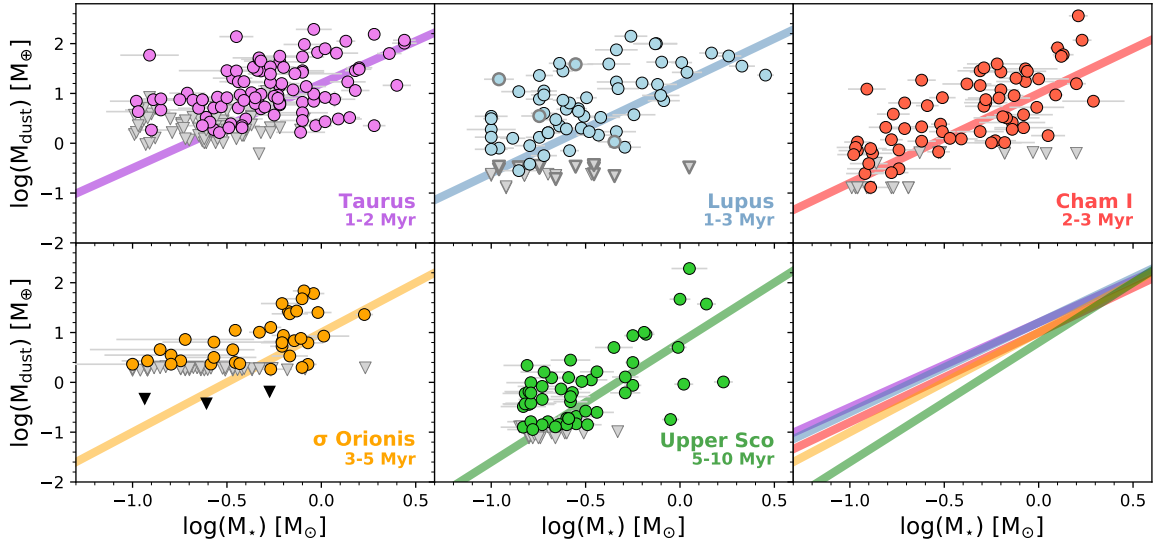
Figure 3.2 Disk dust mass (M_{dust}) as a function of stellar mass ($M_\star$) for disk populations in five star-forming regions with ages spanning the disk dispersal timescale ($\sim$1–10 Myr). Colored circles are (sub-)mm continuum detections and gray triangles are 3σ upper limits. For σ Orionis, the black triangles indicate 3σ upper limits from stacks of the non-detections in three stellar mass bins. For Lupus, the 20 sources with unknown stellar masses that were included in the analysis via an MC method (see Ansdell et al. 2016c) are given representative values and identified by thick gray outlines. For each region, the solid lines show our Bayesian linear regression fits to the data, which take into account upper limits, intrinsic scatter, and measurement errors on both axes (Kelly 2007). The lower right panel compares the fits in all five regions, illustrating the $\sim$1 dex difference in M_{dust} between the youngest and oldest regions at low stellar masses, and the convergence of M_{dust} at high stellar masses.

We derive the M_{dust}–$M_\star$ relation in the five regions considered in this study using the Bayesian linear regression method of Kelly (2007), implemented in Python with the publicly available `linmix` routine.[1] Figure 3.2 shows the fitted M_{dust}–$M_\star$ relations and Table 3.1 presents the fitted parameters. We first reported these results for Lupus, Taurus, and Upper Sco in Ansdell et al. (2016c), showing for the first time that the relation appears to steepen with age. Pascucci et al. (2016) then showed that Chamaeleon I has a slope consistent with the similarly aged Taurus and Lupus regions, further supporting a steepening of the M_{dust}–$M_\star$ relation with age. Our results for σ Orionis were then added in Ansdell et al. (2017), showing an intermediate slope consistent with the intermediate age of the cluster.

---

[1] http://linmix.readthedocs.io/en/latest/src/linmix.html

Table 3.1. $M_{\rm dust}$–$M_\star$ Bayesian Fit Parameters

Region	Age (Myr)	$\alpha^\ddagger$	$\beta^\ddagger$	δ
Taurus	1–2	1.2±0.1	1.7±0.2	0.7±0.1
Lupus[†]	1–3	1.2±0.2	1.8±0.4	0.9±0.1
Cha I	2–3	1.0±0.1	1.8±0.3	0.8±0.1
σ Orionis	3–5	1.0±0.2	2.0±0.4	0.6±0.1
Upper Sco	5–11	0.8±0.2	2.4±0.4	0.7±0.1

Note. — [†]Taken from Ansdell et al. (2016c), as they used the same methodology in § 3.1.2, but also an MC analysis to account for 20 Lupus sources with unknown stellar masses.

Note. — [‡]We follow Kelly (2007), where β and α represent the slope and intercept, respectively. This differs from that of Pascucci et al. (2016), who switched these symbols.

We note that our fitted values in Table 3.1 are largely consistent with those found by Pascucci et al. (2016) (see their Table 4), despite different grain opacity assumptions (e.g., they use $\beta = 0.4$ in Equation 2.1, while we use $\beta = 1.0$) and stellar mass cutoffs (e.g., they include sources with $M_\star < 0.1\ M_\odot$, while we exclude brown dwarfs). Indeed, the main disagreement between our results is the intercept estimate for Lupus, which differs because Pascucci et al. (2016) exclude the 20 sources in Lupus with unknown stellar masses, while we account for them using the MC approach described in Ansdell et al. (2016c). The slope for Upper Sco is also different (although within errors) because Pascucci et al. (2016) only consider "full" and "transitional" disks from Upper Sco, while we also include "evolved" disks following the definition of "primordial" disks in Barenfeld et al. (2016) (§2.4.2).

There are two main possibilities for a steepening of the $M_{\rm dust}$–$M_\star$ relation with age. The first is that mm grains around lower-mass stars more efficiently grow into pebbles that would go undetected by (sub-)mm surveys due to their larger size. The second is that the inward drift of mm-sized grains is more efficient around lower-mass stars, such that a significant fraction of the mm-sized grains are hidden in the optically thick inner disk regions. Testing the first scenario requires multi-band observations at (sub-)mm wavelengths for large

samples of protoplanetary disks spanning a range of stellar masses; such observations, which unfortunately do not yet exist, can constrain the dust opacity index, β (§2.1.1), which should become smaller as grains grow to larger sizes (Draine 2006). Pascucci et al. (2016) tested the second scenario by comparing the M_{dust}–$M_\star$ relation to theoretical models of grain growth, drift, and fragmentation (Krijt et al. 2016) for disks around low-mass (0.2 $M_\odot$) and high-mass (2.0 $M_\odot$) stars. They found that a steepening of the M_{dust}–$M_\star$ relation with age is consistent with inward radial drift being more efficient around lower-mass stars, if the outer disk is in the fragmentation-limited regime. In this regime, grain sizes in the outer disk are limited by fragmenting collisions; when fragmentation sets the largest grain size, inward radial drift occurs more rapidly around lower-mass stars (Birnstiel et al. 2012), making their (sub-)mm continuum emission weaker and more compact with age compared to higher-mass stars, thereby causing the M_{dust}–$M_\star$ relation to steepen with age.

Finally, we address three caveats to our Bayesian linear regression fits. First, Pascucci et al. (2016) found that shallower slopes can result when the sample is dominated by upper limits at low stellar masses. This is only a potential issue for σ Orionis, as its larger distance compared to the other regions resulted in much poorer dust mass sensitivities and roughly two-thirds of the sample remaining undetected in the continuum (see Figure 3.2). However, even if the slope is actually steeper, this would only further distinguish σ Orionis from the younger regions. Second, we show in §3.3 that external photoevaporation is reducing disk dust masses throughout the σ Orionis region. This may serve to steepen the M_{dust}–$M_\star$ relation, as external photoevaporation should be more effective at removing gas and small dust grains around lower-mass stars whose orbiting material is less gravitationally bound. Unfortunately this possible effect has not yet been tested with external photoevaporation models. Third, the Bayesian linear regression of Kelly (2007) is but one method; several other linear regression techniques for left-censored datasets, which also take into account errors on both axes and intrinsic dispersion, are available in the statistical literature (Feigelson & Babu 2012) and should be employed to test the robustness of our results.

3.2 Low gas masses or carbon depletion?

Protoplanetary disks presumably form with an inherited ISM gas-to-dust ratio of ~ 100 (Bohlin et al. 1978), but evolve to the opposite extreme of dusty debris disks with negligible gas in ~ 5–10 Myr (Williams & Cieza 2011). How quickly the dust and gas disperse, especially relative to each other, is important for understanding disk evolution and likely dictates the types of planets that will form in a given disk.

Our ALMA survey of Lupus (§2.2) provides the largest collection of disk gas masses and gas-to-dust ratios available to date. Figure 2.5 shows that, despite their young age of ~ 1–3 Myr, typical disks in Lupus have gas masses well below the MMSN and gas-to-dust ratios significantly lower than the inherited ISM value. The lack of CO detections in all but six disks in our σ Orionis ALMA survey (§2.3), with average gas masses of $< 1\ M_{\mathrm{Jup}}$ and average gas-to-dust ratios of < 3 for the non-detections (§2.3.6), also points to rapid gas depletion. Our findings are consistent with those of Fedele et al. (2010), who used spectroscopically measured accretion rates (i.e., a completely different methodology from this work) to show that inner gas disk lifetimes are shorter than inner dust dissipation timescales; here we extend this finding to disk-averaged values. These findings imply that giant planet formation is either rare or rapid (see §4.1 for a detailed discussion on the implications for planet formation).

The preferential loss of gas relative to dust can be explained by the stratified nature of protoplanetary disks, which are thought to feature gas-rich atmospheres and growing dust grains that settle toward the disk midplane (e.g., D'Alessio et al. 2006). In this scenario, gas is lost via several mechanisms, which include: photoevaporation, where heating from the central star drives a thermal wind from the gas-rich surface layers of the disk (e.g., Alexander et al. 2014); layered accretion onto the central star, where angular momentum transport is driven by magnetic fields coupling to the disk (Gammie 1996); and/or magnetized disk winds, which can drive both accretion onto the central star as well as mass loss from the upper gas-rich disk layers (e.g., Bai 2016).

However, there are several caveats to our gas masses, as they are estimated via emission from CO isotopologues, which are only tracers of the total gas content (§2.1.2). Namely, gas masses derived from CO depend on the adopted molecular CO abundance, which we take as $[CO]/[H_2] = 10^{-4}$, and gas masses derived from CO isotopologues also depend on the adopted isotopologue ratios, which we take as $[CO]/[^{13}CO] = 70$ and $[CO]/[C^{18}O] = 550$ or 1650 (Williams & Best 2014). These values are consistent with those measured in molecular clouds (Frerking et al. 1982; Lacy et al. 1994; Ripple et al. 2013; Shimajiri et al. 2014) as well as with a direct measurement in a disk (France et al. 2014). Nevertheless, carbon abundances may still vary substantially in protoplanetary disks; TW Hydrae has been the primary example used in the literature, as it is one of the only disks with its HD line measured by *Herschel* (Bergin et al. 2013). The strong HD but weak $C^{18}O$ emission toward this system has been interpreted as resulting from significant carbon depletion of up to two orders of magnitude (Favre et al. 2013; Kama et al. 2016a; Schwarz et al. 2016). Indeed, Bergin et al. (2013) found $M_{gas} > 0.05\ M_\odot$ from HD emission, while Williams & Best (2014) found $M_{gas} \approx 5 \times 10^{-4}$ from CO isotopologue emission. However, gas masses estimated from HD depend strongly on the assumed vertical structure of the disk, which is difficult to constrain for most systems, and especially for face-on disks like TW Hydrae. More detailed physical-chemical modeling of the TW Hydrae disk using a revised vertical structure has shown that its HD-derived gas mass may actually be much lower (6–$9 \times 10^{-3}\ M_\odot$; Trapman et al. 2017) than the original estimate from Bergin et al. (2013), and thus closer to the value estimated from CO isotopologue emission

If carbon depletion (rather than gas depletion) is the true cause of the weak CO emission seen in our ALMA observations, then the responsible physical mechanisms are not yet well understood. One hypothesis is that gas-phase reactions initiated by X-ray and cosmic ray ionization of He produce He^+ atoms that react with gaseous CO to gradually extract atomic carbon, which is then processed into more complex molecules that freeze onto cold dust grains at higher temperatures than CO (e.g., Aikawa et al. 1997; Bruderer et al. 2012; Favre et al. 2013; Bergin et al. 2014; Kama et al. 2016a). Alternatively, ice chemistry

reactions can convert CO into more complex organics (e.g., CH_3OH) or into CO_2 and CH_4 ices (e.g., see Figure 3c in Eistrup et al. 2016); these reactions have typical timescales of a few Myr (depending on the ionization rate), thus could be more significant in older systems (Yu et al. 2016, 2017). Volatile carbon may also be locked up in large icy bodies in the disk midplane (Bergin et al. 2010; Ros & Johansen 2013; Guidi et al. 2016), which due to their size cannot diffuse upward and thus would no longer participate in gas-phase chemistry (e.g., Du et al. 2015; Kama et al. 2016b). Such a process would "dry out" the CO from the warm molecular layer probed by our ALMA observations, analogous to what is proposed to explain the under-abundance of gas-phase water in disk atmospheres (Bergin et al. 2010; Hogerheijde et al. 2011).

If any of these mechanisms significantly deplete carbon in protoplanetary disks, our derived gas masses would be underestimated. Our data cannot distinguish between these possibilities, although future ALMA observations will be aimed at resolving this issue (see §4.3.2). Regardless of the cause, the consistently weak CO isotopologue emission found by our ALMA observations indicates rapid gas evolution in protoplanetary disks, either directly in the gas-to-dust ratio or chemically via permanent loss of volatiles to solids. It is also important to note that the low gas-to-dust ratios are not due to over-estimated dust masses; for realistic conditions of grain compositions and sizes, Ossenkopf & Henning (1994) show that the dust opacity (κ) used in Equation 2.1 does not change sufficiently to account for the factor of $\sim$10 discrepancy between our inferred gas-to-dust ratios and that of the ISM. If anything, the growth of planetesimals would decrease the continuum emission and thereby increase the apparent gas-to-dust ratio.

3.3   External photoevaporation from OB stars

OB associations host at their centers very massive stars with spectral classifications of O and B type, surrounded by populations of several hundred to thousands of lower-mass stars. The massive OB stars emit large numbers of extreme-ultraviolet (EUV; $h\nu > 13.6$ eV) and

far-ultraviolet (FUV; 6 eV $< h\nu <$ 13.6 eV) photons, which can photoevaporate the circumstellar disks around the nearby low-mass stars (see the recent review in Gorti et al. 2016). The high-energy EUV radiation impinging on the low-density gas surrounding a disk will create an ionization front, from which an ionized wind launches with a mass-loss rate that is inversely proportional to the distance of the disk from the OB star (Johnstone et al. 1998). The EUV photons cannot penetrate the ionization front, but the non-ionizing FUV photons can proceed to heat the neutral gas closer to the disk, thereby creating a thermal wind. The resulting FUV-driven mass-loss rate due to this thermal wind is not explicitly related to the strength of the FUV field, and thus the distance of the disk from the ionizing source. However, there does exists a minimum value of the FUV field strength below which FUV heating is no longer sufficient to launch a substantial thermal wind (Johnstone et al. 1998; Störzer & Hollenbach 1999).

Thus the schematic picture is that of an OB star immediately surrounded by a small EUV-dominated region featuring high disk mass-loss rates, followed by a larger FUV-dominated zone with a spatially constant mass-loss rate, until some distance from the OB star at which external FUV photoevaporation is no longer effective. To search for evidence of disk mass loss induced by external photoevaporation, Mann et al. (2014) used the SMA and ALMA to observe the iconic proplyds in the young ($\sim$1–2 Myr) Orion Nebula Cluster (ONC). They found a lack of massive ($M_{\rm dust} \gtrsim 9\ M_{\oplus}$) disks within $\sim$0.03 pc of the central O6V star, θ^1 Ori C, where models predict that EUV emission dominates the radiation field (Johnstone et al. 1998). At larger separations of $\sim$0.03–0.3 pc, where less energetic FUV emission is expected to dominate (Adams et al. 2004), they found a range of disk masses representative of typical low-mass star-forming regions, indicating that the lower mass-loss rates in FUV-dominated regions can preserve disk masses for up to a couple Myr. Mann et al. (2014) concluded that planet formation is likely inhibited for disks in the innermost EUV-dominated regions of OB associations due to high mass-loss rates, while disks in the FUV-dominated regions and beyond are relatively unaffected with planet formation proceeding as in isolated disks.

Mann et al. (2015) then looked for similar effects in the very young NGC 2024 region, which at ~0.5 Myr old (e.g., Levine et al. 2006) hosts the massive star IRS 2b of O8V–B2V spectral type (Bik et al. 2003) as well as several hundred YSOs still heavily embedded in molecular cloud material. Mann et al. (2015) could not identify a distance-dependent disk mass distribution in NGC 2024, and instead found several massive ($M_{\rm dust} \gtrsim 17\ M_\oplus$) disks located < 0.01 pc from IRS 2b. They argued that this could be an evolutionary effect: the extremely young age of NGC 2024 simply means that processes like external photoevaporation have not yet had time to significantly reduce disk masses. Alternatively, they suggested this could be an environmental outcome: the significant cloud material in NGC 2024 may efficiently absorb the high-energy photons from IRS 2b, or the later spectral type of the star (compared to θ^1 Ori C in the ONC) means that it does not produce sufficient amounts of EUV/FUV photons to drive significant external photoevaporation.

Here we search for evidence of external photoevaporation in σ Orionis, an OB association whose central trapezium system, σ Ori, contains a massive O9V star (e.g., Simón-Díaz et al. 2015). σ Orionis is an interesting target for studying external photoevaporation, as its lack of cloud material and older age may both enhance the observable effects of external photoevaporation. Figure 3.3 shows a map of σ Orionis with the results from our ALMA survey over-plotted, while Figure 3.4 (upper panel) plots $M_{\rm dust}$ as a function of projected separation from σ Ori. Similar to the ONC, we find a lack of massive ($M_{\rm dust} \gtrsim 3\ M_\oplus$) disks close to the central OB system; however, the drop in occurrence is seen at ~0.5 pc, which is a much larger projected distance compared to the ~0.03 pc limit found for the ONC. The smaller $M_{\rm dust}$ values and larger projected distances found in σ Orionis (compared to those found in the ONC) are likely both influenced by the older age of the region: namely, $M_{\rm dust}$ distributions decline with cluster age (§3.1.1) and typical intra-cluster velocity dispersions on ~km s^{-1} scales can result in cluster expansions of several parsecs by the age of σ Orionis. Beyond ~0.5 pc, we also see a smooth distance-dependent $M_{\rm dust}$ distribution that extends out to the edge of the cluster. This is somewhat unexpected given that mass-loss rates should not depend on the FUV field strength (Johnstone et al. 1998; Störzer & Hollenbach
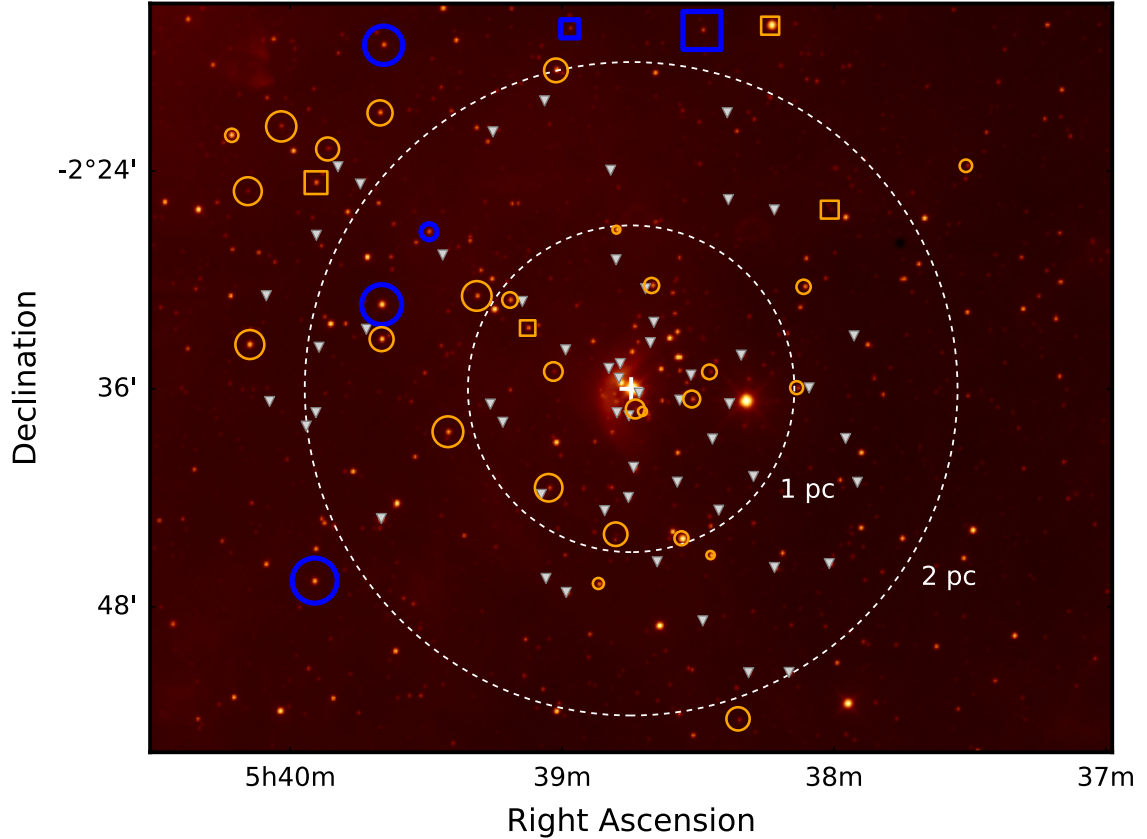
Figure 3.3 Map of σ Orionis with our ALMA 1.33 mm continuum detections (§2.3.4) circled in orange and CO $J = 2$–1 detections (§2.3.5) circled in blue; non-detections are shown by gray triangles. Symbol size scales with the ratio of disk dust mass to stellar mass ($M_{\rm dust}/M_\star$) and squares indicate TDs (Table 2.4). The central OB system, σ Ori, is marked by the white cross, and the dashed white circles show radial distances of 1 pc and 2 pc. Notably, the sources with detectable gas emission are among the furthest from σ Ori.

1999) and thus the distance from the ionizing source. However, this may also be explained by cluster expansion combined with the minimum FUV field strength needed to induce thermal winds: namely, disks in the outer regions of the cluster may have expanded beyond the FUV-dominated region sooner than those in the inner regions of the cluster, thus experienced externally driven mass loss for shorter time periods. Another possibility is that stars in the outer regions of the cluster were more protected from FUV irradiation due to intra-cluster cloud material that has since dispersed.

One concern is that, due to the M_{dust}–$M_\star$ relation (§3.1.2), mass segregation in clusters could produce these observed trends, if the least massive stars are preferentially located closer to the cluster centers. Mann et al. (2014) could not test this in the ONC, as the nature of proplyds complicates any estimates of stellar mass. Because we can estimate stellar masses in σ Orionis (§2.3.2), we also show in Figure 3.4 (lower panel) the $M_{\mathrm{dust}}/M_\star$ ratio as a function of projected separation, confirming that the distance-dependent trend still holds even when accounting for stellar mass differences. Figure 3.4 also shows our ALMA continuum detection fraction, illustrating a relatively constant detection rate of $\sim$30% out to $\sim$2 pc, after which the detection fraction more than doubles to $\sim$70%. Hernández et al. (2007) did not find a similar change in detection fraction with their *Spitzer* survey of σ Orionis disks (see their Figure 16); however, this may be because external photoevaporation does not remove material from the inner (i.e., more gravitationally bound) disk regions probed by *Spitzer*.

Interestingly, we also find that the CO detections in our ALMA sample (blue circles in Figures 3.3 & 3.4) only exist in the outer regions of the cluster. This is qualitatively consistent with the picture of external photoevaporation: for typical disks, the gas is generally more extended than the dust, and therefore less tightly bound to the star, making the gas more susceptible to external photoevaporation. However, our gas sample is small and Mann et al. (2014) were unable to reliably detect gas in ONC disks due to cloud confusion, making it important to confirm our finding with surveys of other OB associations (see §4.3.1). If external photoevaporation does have a more significant effect on gas relative to dust, this would impact the types of planets that can form in OB associations.

Some evidence for external photoevaporation has been previously found for σ Orionis disks. Rigliaco et al. (2009) detected strong optical forbidden emission lines from SO 587, which they interpreted as an externally driven photoevaporative flow due to the very low stellar mass accretion rate for this source, the profile shapes and luminosities of the forbidden emission lines, and the small projected separation ($\sim$0.3 pc) of the disk from σ Ori (we did not detect this source with our ALMA observations; see Tables 2.5 & 2.6). Additionally,
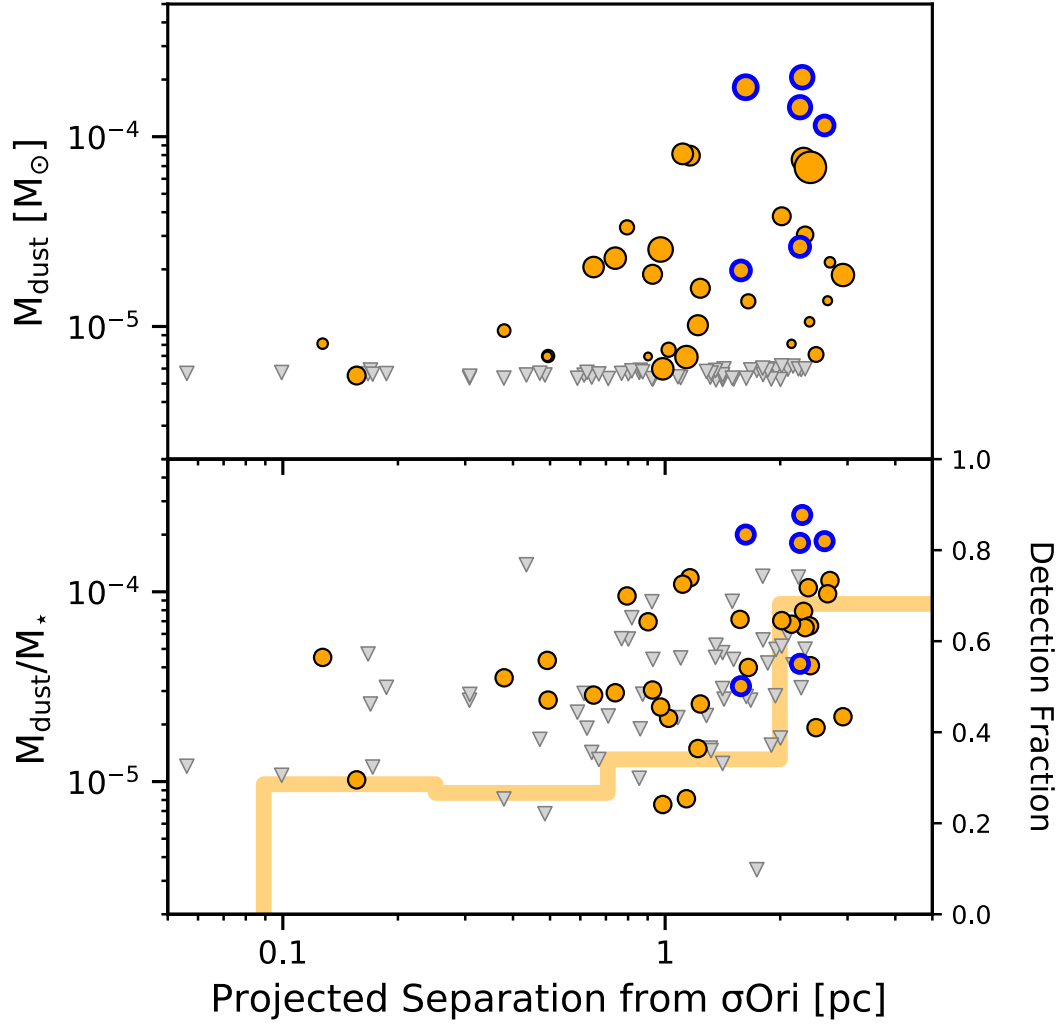
Figure 3.4 *Top*: Disk dust mass ($M_{\rm dust}$) as a function of projected separation from σ Ori (α = 05:38:44.779, δ = −02:36:00.11), where orange points are ALMA 1.33 mm continuum detections and gray triangles are 3σ upper limits (§2.3.4). Disks also detected in CO $J = 2$–1 (§2.3.5) are outlined in blue and symbol sizes scale with the ratio of disk dust mass to stellar mass ($M_{\rm dust}/M_{\star}$). This plot illustrates how $M_{\rm dust}$ clearly declines with smaller projected separations from the central OB system, massive disks ($M_{\rm dust} \gtrsim 3\ M_{\odot}$) are missing within ∼0.5 pc of σ Ori, and disks with detectable gas emission only exist in the outer regions of the cluster. *Bottom*: $M_{\rm dust}/M_{\star}$ as a function of projected separation from σ Ori, illustrating that the declining trend still holds even after correcting for the $M_{\rm dust}$–$M_{\star}$ relation (§3.1). Our ALMA continuum detection fraction, shown by the thick orange line, also stays relatively constant until ∼2 pc, after which it doubles.

Maucó et al. (2016) fit irradiated accretion disk models to the SEDs of 18 sources in σ Orionis to show decreased disk masses and sizes when compared to those in the younger ONC. They interpreted this as evidence for external photoevaporation, however their results were uncertain due to various model assumptions (e.g., constant viscosity of $\alpha = 0.01$) as well as the comparison of disk properties derived from disparate methods (e.g., they compared σ Orionis disk radii derived from SED modeling, which probes the dust disk, to ONC disk radii derived from *Hubble* imagery, which probes the gas disk). Thus our ALMA observations provide the clearest evidence to date that external photoevaporation is affecting disk masses throughout the σ Orionis region.

Our findings also indicate that FUV (not just EUV) emission from OB stars is an important driver of external photoevaporation, contrary to the previous findings of Mann et al. (2014). Moreover, it appears that the FUV field does not need to be particularly strong to induce significant mass loss. Assuming a typical O9V FUV luminosity of $\log(L_{\mathrm{FUV}}/L_\odot) = 4.5$ for σ Ori, the geometrically diluted FUV flux can be expressed as $\sim 8000(d/\mathrm{pc})^{-2}\,G_0$, where d represents the distance from the photoevaporative source in parsecs and $G_0 = 1.6 \times 10^{-3}\,\mathrm{erg\,cm^{-2}\,s^{-1}}$ (Habing 1968). We note that although σ Ori is a triple system, the FUV flux is usually dominated by the most massive star in the cluster (Fatuzzo & Adams 2008; Holden et al. 2011). In this simple calculation, we also do not consider any extinction due to intra-cluster dust, which is observed to be at low densities in σ Orionis (Walter et al. 2008), unlike in the ONC and NGC 2024. Figure 3.4 shows that external photoevaporation is affecting disk masses out to at least ~ 2 pc, which when combined with the above equation corresponds to FUV fluxes $\gtrsim 2000\,G_0$.

This reinforces recent observations of smaller disk samples, which suggest that even moderate FUV fluxes can drive significant mass loss. Kim et al. (2016) observed 7 proplyds near a B star in NGC 1997, finding high mass-loss rates for an FUV flux of only $\sim 3000\,G_0$. Haworth et al. (2017) also showed that the outer disk of IM Lup may be undergoing photoevaporation from an FUV flux of just $\sim 4\,G_0$, where the high mass-loss rate can be explained by the large size of the disk (Cleeves et al. 2016), which causes gas in the outer

regions to be only weakly gravitationally bound to the central star. Futhermore, Guarcello et al. (2016) found that disk frequency (as probed by near-IR excess) declines with smaller projected separation from the OB stars in Cygnus OB2 for FUV fluxes $\gtrsim 1000\,G_0$. Together, these observations support recent theoretical findings by Facchini et al. (2016) and Haworth et al. (2016), who predict high mass-loss rates from moderate ($< 3000\,G_0$) external FUV fluxes due to grain growth in disks. Moreover, these slow photoevaporative winds should be much more effective at removing gas and small ($\lesssim 1~\mu$m) dust particles compared to larger ($\gtrsim 1$ mm) solids (Facchini et al. 2016), which may help to explain our lack of gas detections at projected distances of $\lesssim 1.5$ pc from σ Ori.

Finally, we showed in §2.3.6 that the average dust mass of the undetected sources in σ Orionis is at least $\sim 5\times$ lower than the smallest dust mass among the continuum detections, implying that disk dispersal occurs on short timescales once it begins. The rapid dispersal of disks impinged by intermediate external FUV fluxes has been predicted by Clarke (2007) and later by Anderson et al. (2013). Their models combine estimated mass-loss rates from external FUV photoevaporation with viscous disk evolution to show that disks should be dispersed from the outside in on timescales much shorter than the expected disk lifetime. The typical lifetime of a viscous disk impinged with a $\sim 3000\,G_0$ FUV flux was predicted to be roughly a few Myr, in agreement with our observations.

In summary, our observations indicate that external photoevaporation due to FUV emission from OB stars is significantly affecting disk evolution throughout the σ Orionis cluster, although other disk evolution mechanisms are also clearly at play (§3.1). This additional depletion of dust and gas for disks in OB clusters should have implications for planet formation, especially since most disks form in cluster environments, and detailed theoretical studies will help to quantify the impacts for different planet types as well as identify any associated trends seen in the exoplanet population.

Chapter 4

Discussion & Future Work

In this final chapter, we discuss how the results from our ALMA protoplanetary disk surveys inform our understanding of planet formation. Our overall findings indicate that giant planet formation is either rare or rapid, with the former being more consistent with exoplanet statistics. We also discuss how the trends that we derive for protoplanetary disk populations may fundamentally explain the trends seen in the exoplanet population.

The power of our ALMA surveys in improving our understanding of disk evolution and planet formation is further enhanced when the results are combined with other datasets. We present two examples of this in this chapter. First, we combine the disk dust masses derived from our ALMA continuum observations with the stellar mass accretion rates from VLT/X-Shooter in order to test theories of viscous disk evolution. Second, we use high-precision light curves from the *K2* mission to study the inner disk regions, showing that their geometry can differ significantly from the outer disk regions probed by ALMA.

Finally, we discuss prospects for future research. Our future efforts focus on furthering our understanding of the effects of external photoevaporation on disk evolution and planet formation in OB clusters, and disentangling whether the weak CO emission seen in our ALMA surveys is due to bulk gas depletion or rather volatile carbon depletion. We conclude with a brief overview of the presented work.

4.1 Implications for Planet Formation

4.1.1 Is Giant Planet Formation Rare?

Core accretion theory predicts that giant planets form when solid cores of a minimum critical mass assemble in the disk, enabling runaway accretion of the surrounding gaseous material (Pollack et al. 1996; Ida & Lin 2004). The accretion of a gaseous envelope is expected to occur rapidly, where $\sim$10 $M_\oplus$ cores reach masses of $\sim$1 $M_{\rm Jup}$ within $\sim$0.1 Myr. Within the framework of this model, we can constrain the occurrence of giant planet formation by observing how quickly the dust and gas content in typical protoplanetary disks depletes to levels below what are thought to be needed to form a gas giant.

With regards to the solids, we can look at the fraction of protoplanetary disks in a region with dust masses above $\sim$10 $M_\oplus$ (e.g., roughly the core masses of Jupiter and Saturn; Guillot 1999). For regions at $\sim$1–3 Myr of age, we saw approximately a quarter of protoplanetary disks above this threshold (30% in Taurus, 26% in Lupus, and 23% in Chamaeleon I). This fraction is cut in half by $\sim$3-5 Myr (13% in σ Orionis) and then halved again by $\sim$5–10 Myr (5% in Upper Sco). Although these are only rough estimates, they clearly reflect a sharp decline in the capacity of disks to form giant planets with age. Notably, the three youngest regions consistently demonstrate that even $\sim$1–3 Myr old disks lack sufficient reservoirs of μm- to cm-sized dust needed to form the solid cores of giant planets, even when assuming 100% efficiency in converting this dust into planet cores.

These findings may imply that giant planet formation is well on its way after just a few Myr of disk evolution, with most of the solid material that will be used for planet formation already locked into stable collections of larger bodies that do not emit significantly at (sub-)mm wavelengths. This is consistent with theoretical studies showing that grain growth to meter-sized bodies can occur in just $\sim$1 Myr, if vertical turbulent mixing is included and fragmentation is ignored (Dullemond & Dominik 2005). However, including fragmentation in numerical simulations reveals the emergence of a fragmentation-coagulation equilibrium within $\sim$1 Myr, which effectively limits grain growth to roughly cm sizes (e.g., Birnstiel

et al. 2012). This so-called "fragmentation barrier" (along with the "radial drift barrier," which also becomes important around cm sizes) needs to be overcome in order to form larger bodies such as planetesimals. This can occur if areas of high local particle density form in the disk midplane (e.g., via the "streaming instability"; Youdin & Goodman 2005), allowing planetesimals to assemble by gravitational collapse of pebble clumps (see review in Johansen et al. 2014). Planetesimal growth is an active area of research and the key physical mechanisms are still being investigated both theoretically and observationally.

Alternatively, our findings may imply that giant planet formation is rare, with typical disks simply lacking the sufficient solid material needed to form giant planet cores. This scenario is more consistent with exoplanet statistics: transit, microlensing, and RV surveys have shown that giant planets have occurrence rates of $\sim 10\%$ when integrating over spectral type and orbital radius (e.g., Cassan et al. 2012; Montet et al. 2014; Bowler et al. 2015). A scarcity of giant planets is also consistent with theoretical work: for example, Laughlin et al. (2004) showed that the formation of Jupiter-mass planets orbiting low-mass ($\lesssim 0.4 M_\oplus$) stars is strongly inhibited at all orbital radii due to low disk surface densities (reducing the amount of available material) as well as long Keplerian timescales (resulting in slow planetesimal growth and accumulation rates).

Additionally, stacking the continuum non-detections from our ALMA surveys allows us to put limits on the average amount of dust in the lowest-mass disks (see §2.2.6 & 2.3.6). In Lupus, we found that the undetected disks had extremely low average dust masses of $\lesssim 6$ Lunar masses (0.03 $M_\oplus$), comparable to debris disk levels (Wyatt 2008). Although the further distance to σ Orionis resulted in looser constraints, we still found that undetected disks have $\lesssim 4$ Martian masses (0.4 $M_\oplus$) of dust on average, which is $5\times$ lower than the faintest detected disk in this region. These findings support theoretical predictions that viscous disks evolve rapidly into debris disks once stellar accretion ceases and photoevaporation from the central star dominates, clearing the dust from the inside out and leaving behind larger solids such as pebbles and planetesimals (e.g., Clarke et al. 2001; Alexander et al. 2006). Previous studies of weak-lined T Tauri stars have provided

observational evidence for rapid disk clearing (e.g., Cieza et al. 2013; Hardy et al. 2015), however our larger and more homogeneous samples of Lupus and σ Orionis disks confirm that rapid disk clearing is a uniform occurrence, even among young protoplanetary disk populations. If disks are indeed being cleared of their dust at early stages via internal photoevaporation, this would clearly inhibit the formation of giant planet cores.

Another ingredient for giant planet formation is of course the gas. As shown in Figure 2.5, we found that, despite their moderate age of $\sim$1–3 Myr, typical disks in Lupus have gas masses of $\lesssim$1 $M_{\rm Jup}$ (i.e., an order of magnitude below the MMSN) and gas-to-dust ratios of $\lesssim$10 (i.e., an order of magnitude lower than the inherited ISM value). This rapid gas depletion in young protoplanetary disks may also help to explain the scarcity of gas giants seen in the exoplanet population, as there is simply not enough gas available in most disks by the time giant planet cores have grown to the sizes at which they rapidly accrete gaseous envelopes. However, bulk gas masses are notoriously difficult to measure (§3.2), and additional observations are required to disentangle whether the weak CO emission seen in our ALMA observations is indeed due to low gas masses or is rather the result of volatile carbon depletion (§4.3.2). Still, the fact that we found only six disks in σ Orionis exhibiting ^{12}CO emission (§2.3.5) is telling, as the emission in this line is optically thick. This lack of gas in σ Orionis disks may also be related to external photoevaporation occurring in the region (§3.3), which would serve to shorten the gas disk lifetime, thereby inhibiting giant plant formation as well as migration. If external photoevaporation is significantly shortening gas disk lifetimes, then this process will be an important factor to consider in planet formation models as many planetary systems, including our solar system, are likely born in clusters hosting OB stars (Adams 2010).

Rapid gas depletion in typical protoplanetary disks may also help to explain the unexpected prevalence of intermediate-mass planets seen in the exoplanet population. Exoplanet surveys have found that intermediate-mass "super-Earths" and "mini-Neptunes" are over an order of magnitude more abundant than gas giants (at least around around G/K-type stars with $P \lesssim 100$ days; Howard et al. 2012; Petigura et al. 2013; Marcy et al. 2014).

This finding challenges traditional planet formation theories, which predicted a "planetary desert" at intermediate masses (Ida & Lin 2004). This is because cores of $\sim$10 $M_\oplus$ should have sufficient gravity to rapidly accrete gaseous envelopes, reaching masses of $\sim$1 $M_{\rm Jup}$ within $\sim$0.1 Myr if gas is still present in the disk (e.g., Pollack et al. 1996). However, if typical disks are already depleted in gas at a few Myr, such cores capable of accreting gaseous envelopes would be prohibited from doing so, more often ending up as intermediate-mass super-Earths or mini-Neptunes rather than gas giants (Lee & Chiang 2016). Furthermore, the fact that the exoplanet population is more of a "tropical rainforest" at these intermediate masses (i.e., exhibiting a diversity of compositions, ranging from rocky planets to those hosting substantial atmospheres; Hand 2011) may be due to the rapid evolution and inherent diversity of circumstellar disks (e.g., gas-to-dust ratios ranging from $\sim$0.1–100 in Lupus) having significant influences on the assembly of planetary systems.

4.1.2 Relating Disk Trends to Exoplanet Trends

Several dependencies between the properties of exoplanets and their host stars have emerged in the wake of large-scale exoplanet surveys, such as the Eta-Earth radial velocity survey (Howard et al. 2010) and the *Kepler* transit survey (Borucki et al. 2010). These exoplanet trends likely originate from similar stellar-mass-dependent disk trends; indeed, population synthesis models show planet properties being largely dictated by the initial dust and gas content of disks as well as their subsequent evolution (e.g., Mordasini et al. 2012).

One of the clearest exoplanet trends is the positive correlation between giant planet frequency and host star mass (e.g., Endl et al. 2006; Johnson et al. 2007; Bowler et al. 2010). For example, Johnson et al. (2007) found that within 2.5 AU, Jovian planet occurrence rates are 1.8% around low-mass M/K stars, increasing to 4.2% around solar-mass stars, and then to 8.9% for higher mass sub-giants. As pointed out in Andrews et al. (2013), the correlation between giant planet frequency and host star mass can be qualitatively explained by the $M_{\rm disk}$–$M_\star$ relation seen in protoplanetary disk populations (§3.1.2). This is because models predict that giant planet formation is more efficient both in higher-mass disks and around

higher-mass stars. Giant planets form more efficiently in higher-mass disks because higher disk masses translate to higher disk surface densities ($\Sigma_{\rm disk} \propto M_{\rm disk}$) and thus faster planet core growth ($\dot{M}_{\rm core} \propto \Sigma_{\rm disk}$; e.g., Ikoma et al. 2000). Moreover, the planetary gas accretion rate is limited by the disk accretion rate (e.g., Mordasini et al. 2012), which itself correlates with stellar mass (Hartmann et al. 1998), allowing giant planets forming in higher-mass disks to accrete more substantial envelopes on shorter timescales. Giant planets also form more efficiently around higher-mass stars because the dynamical timescales are faster (assuming Keplerian rotation; $\propto \sqrt{M_\star}$) and the potential formation zones are larger ($\propto M_\star$; Ida & Lin 2005; Kennedy & Kenyon 2008) in the surrounding disks. By showing that the $M_{\rm disk}$–$M_\star$ relation holds for protoplanetary disk populations spanning the disk dispersal timescale (Figure 3.2), we have provided strong evidence that the $M_{\rm disk}$–$M_\star$ relation fundamentally explains the correlation between giant planet frequency and host-star mass.

Another trend seen in the exoplanet population is the over-abundance of Earth-sized planets around M dwarfs compared to solar-type stars (e.g., Dressing & Charbonneau 2015; Mulders et al. 2015). For example, Mulders et al. (2015) found that, for $P \lesssim 150$ days, Earth- to Neptune-size planets (1–4 $R_\oplus$) around M dwarfs occur twice as frequently as around G dwarfs and three times as frequently as around F-type stars. This points to a higher formation efficiency of low-mass planets around low-mass stars, and may be related to the steepening of the $M_{\rm disk}$-$M_\star$ relation with age (§3.1.2). Pascucci et al. (2016) showed that the steepening of the $M_{\rm disk}$-$M_\star$ relation could be explained by the inward drift of mm-sized grains being more efficient around lower-mass stars compared to higher-mass stars. This could help to qualitatively explain the higher occurrence rate of Earth-sized planets around M dwarfs compared to solar-type stars, as it would deliver more solids into the inner regions of disks around low-mass stars, where the observed over-abundance of Earth-sized planets is observed. Indeed, the availability of more solids in the inner disk should enhance the formation of Earth- and Neptune-sized planets at these shorter orbital periods (e.g., Raymond et al. 2005; Kokubo et al. 2006). Detailed dynamical modeling that takes into account updated star-disk scaling laws will be required to confirm this hypothesis.

4.2 Combining ALMA Disk Surveys with Other Datasets

4.2.1 Testing Viscous Evolution Theory

Protoplanetary disks are traditionally thought to evolve viscously (Lynden-Bell & Pringle 1974), whereby turbulence in the disk redistributes angular momentum by spreading the gaseous component outward with time, which in turn drives the accretion of disk material onto the central star in order to conserve angular momentum. A fundamental prediction of viscous evolution theory is the linear relation between the mass accretion rate onto the central star ($\dot{M}_{\mathrm{acc}}$) and the mass of the surrounding protoplanetary disk (M_{disk}). The ratio of these quantities ($M_{\mathrm{disk}}/\dot{M}_{\mathrm{acc}}$) should also be roughly $2\times$ the disk age (see Equation 7 in Hartmann et al. 1998), independent of the initial disk conditions and assumed disk viscosity (Jones et al. 2012). Observational confirmation of this relation has been long sought, but pre-ALMA surveys were unable to find any statistically significant correlations (Andrews et al. 2010; Ricci et al. 2010).

For the first time, we find a statistically significant correlation between $\dot{M}_{\mathrm{acc}}$ and M_{disk} using our sample of Lupus protoplanetary disks with stellar and disk properties that have been homogeneously measured by state-of-the-art facilities. We use $\dot{M}_{\mathrm{acc}}$ values estimated from UV excess measured with the VLT/X-Shooter spectrograph (Alcalá et al. 2014, 2017) combined with M_{disk} values derived from (sub-)mm continuum emission measured by our ALMA surveys (§2.2.4) assuming an ISM gas-to-dust ratio of 100. There are 66 protoplanetary disks in Lupus that have both VLT/X-Shooter and ALMA measurements, although 5 have $\dot{M}_{\mathrm{acc}}$ values consistent with chromospheric noise rather than accretion and another 4 are edge-on disks whose $\dot{M}_{\mathrm{acc}}$ values are likely underestimated. Thus we fit the relation for the remaining 57 Lupus protoplanetary disks using the Bayesian linear regression method of Kelly (2007) to properly account for upper limits. We find a slope of $\beta = 1.2 \pm 0.2$ (Figure 4.1), which is consistent with the linear relation predicted by viscous theory. We find a probability of $< 10^{-4}$ of no correlation using the Cox hazard test for censored data in the `ASURV` package. This work is published in Manara et al. (2016).
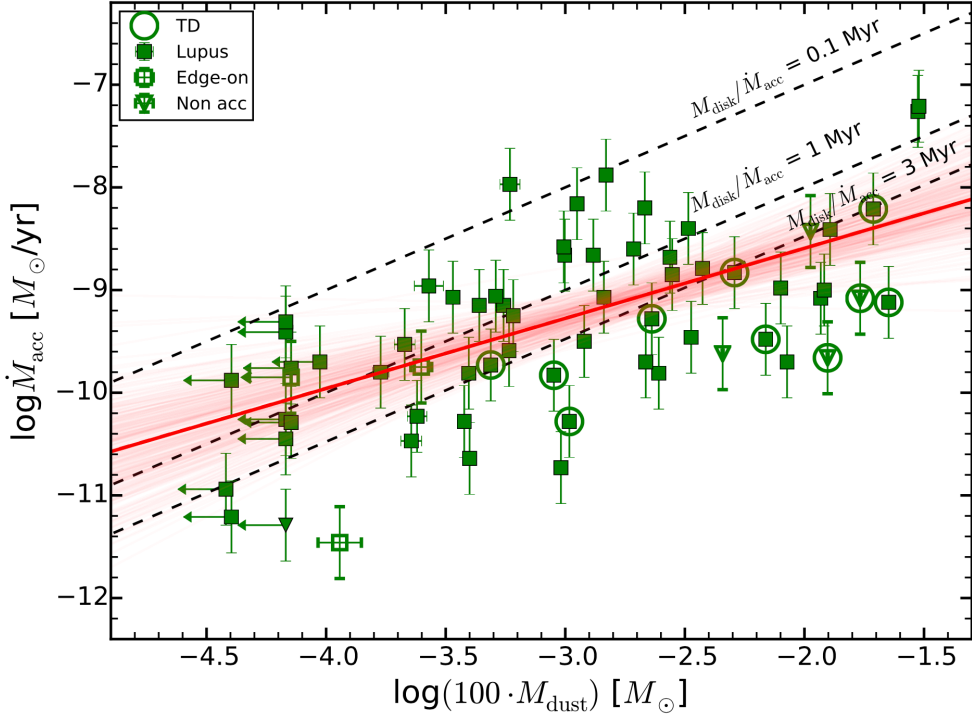
Figure 4.1 $\dot{M}_{\text{acc}}$ vs. M_{dust} for the 66 Lupus disks with both VLT/X-Shooter and ALMA data (taken from Manara et al. 2016). Green filled squares are the 57 disks used to fit the $\dot{M}_{\text{acc}}$-M_{dust} relation (§4.2.1). Open squares are edge-on disks and downward triangles are non-accretors (excluded from the fit). The fit derived using the Bayesian linear regression method of Kelly (2007) is shown by the dark red line; the lighter red lines are a subsample of the MCMC chains. The dashed black lines show different values of the $M_{\text{disk}}/\dot{M}_{\text{acc}}$ ratio.

We also show in Figure 4.1 lines of constant $M_{\text{disk}}/\dot{M}_{\text{acc}}$ ratios, which as discussed above should be comparable to the disk age. The observed distribution generally agrees with theoretical predictions, as ~60% of the targets are lying within or near the ~1–3 Myr age range of Lupus. This agreement is interesting, not only because it provides observational evidence for viscous evolution, but also because of our assumption of an ISM gas-to-dust ratio of 100, which supports the depletion of volatile carbon rather than bulk gas content to explain the weak CO emission found in our ALMA surveys (§3.2). We could not find a significant correlation between $\dot{M}_{\text{acc}}$ and M_{disk} using the gas-to-dust ratios measured by our CO isotopologue measurements (§2.2.5). However, this is likely due to the large gas mass uncertainties as well as the preponderance of gas mass upper limits dominating the sample.

Our derived $\dot{M}_{\rm acc}$–$M_{\rm disk}$ relation can be improved with better constraints on $M_{\rm disk}$, which are still uncertain due to required assumptions of gas-to-dust ratios, dust grain opacities, and disk temperatures—all of which likely depend on stellar mass to various extents. These improved constraints are expected from future ALMA observations that will be conducted at higher sensitivity and multiple wavelengths as well as targeted toward specific molecules. Detailed studies of the $\dot{M}_{\rm acc}$–$M_{\rm disk}$ relation are important for understanding what disk evolutionary processes dominate at different stellar masses, ages, and environments. For example, internal photoevaporation drives inside-out clearing, effectively inhibiting $\dot{M}_{\rm acc}$ and thus producing observed $M_{\rm disk}/\dot{M}_{\rm acc}$ ratios much higher than the disk age. Conversely, external photoevaporation drives outside-in clearing, effectively reducing $M_{\rm disk}$ and thus producing observed $M_{\rm disk}/\dot{M}_{\rm acc}$ ratios much smaller than the disk age. Studying the $\dot{M}_{\rm acc}$–$M_{\rm disk}$ relation in regions of different ages and environments will therefore give insight into when and how these processes dominate disk evolution.

To this end, we also search for the $\dot{M}_{\rm acc}$–$M_{\rm disk}$ relation in σ Orionis. We use $M_{\rm disk}$ values estimated from our ALMA continuum fluxes (§2.3.4) assuming ISM gas-to-dust ratios of 100. We use $\dot{M}_{\rm acc}$ values measured from the U–band survey of Rigliaco et al. (2011), noting that these photometrically derived accretion rates are less accurate than those obtained with spectroscopy for Lupus disks. As shown in Figure 4.2, only 20 sources (the most massive disks in σ Orionis) have both $M_{\rm disk}$ estimates and constraints on $\dot{M}_{\rm acc}$ (the latter of which are mostly upper or lower limits). The sparseness of this sub-sample, combined with the smaller $M_{\rm disk}$ range when compared to the Lupus sample, limits our ability to fit the $\dot{M}_{\rm acc}$–$M_{\rm disk}$ relation for σ Orionis disks. However, we note that, as for Lupus disks, many of the $M_{\rm disk}/\dot{M}_{\rm acc}$ ratios are consistent with the age of σ Orionis when using an ISM gas-to-dust ratio of $\sim$100.

Interestingly, disks with $M_{\rm disk}$ upper limits (i.e., the least massive disks in σ Orionis) span over 2 dex in their $M_{\rm disk}/\dot{M}_{\rm acc}$ ratios (see Figure 4.2). The undetected disks with upper limits on $\dot{M}_{\rm acc}$ may still be consistent with viscous evolution. However, the undetected disks with significant $\dot{M}_{\rm acc}$ values ($\log(\dot{M}_{\rm acc}) > -10$) are unexpected, as they should have
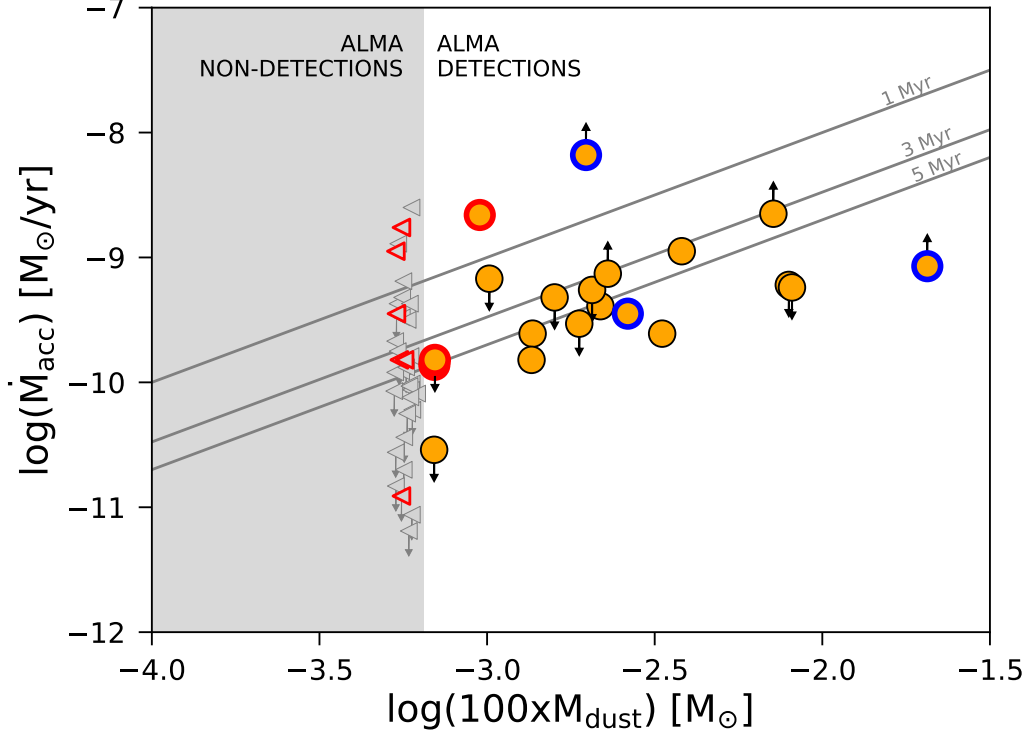
81

Figure 4.2 $\dot{M}_{\rm acc}$ values derived from U–band observations (Rigliaco et al. 2011) versus $M_{\rm disk}$ ($= 100 \times M_{\rm dust}$) values derived from ALMA data (§2.3), for the σ Orionis members included in both surveys (taken from Ansdell et al. 2017). Orange circles are ALMA continuum detections and gray triangles are 3σ upper limits. Up/downward arrows are lower/upper limits on $\dot{M}_{\rm acc}$. Sources outlined in blue are CO detections and sources outlined in red are $\lesssim 0.5$ pc from the central OB system. The diagonal lines show different $M_{\rm disk}/\dot{M}_{\rm acc}$ ratios.

lifetimes shorter than the age of the region. The sources $\lesssim 0.5$ pc from the central OB star (outlined in red in Figure 4.2) are readily explained by external photoevaporation, which reduces $M_{\rm disk}$ by removing mass from the outer disk, thereby decreasing $M_{\rm disk}/\dot{M}_{\rm acc}$ (Rosotti et al. 2017). Although this accounts for only a handful of objects, there is evidence that external photoevaporation is occurring throughout the region (§3.3), thus may apply to more undetected disks. Additionally, the $\dot{M}_{\rm acc}$ values estimated from U-band photometry are uncertain and need to be confirmed with spectroscopy. Nevertheless, there are a sufficient number of sources with low disk masses and significant accretion rates to warrant further investigation. These objects may have strongly variable accretion rates, or the accreting gas may come from evaporating icy dust grains rather than primordial disk gas.

4.2.2 Connecting the Inner and Outer Disk

The ALMA observations presented in this work have resolutions of 40–120 AU, such that they only probe the bulk disk properties and cannot be used to study the inner disk regions, where the vast majority of known exoplanets orbit. The inner regions of protoplanetary disks are notoriously difficult to observe due to small angular scales and faint disk emission compared to the host star. Even in the era of extreme AO imagers (e.g., GPI, SCExAO, SPHERE) and long-baseline (sub-)mm interferometers (e.g., ALMA), we are limited to studying regions $\gtrsim$10 AU for typical disks. Thus there is a need to develop methods for probing the inner regions of protoplanetary disks, so that we can connect the inner and outer regions into a coherent picture of global disk evolution and ultimately planet formation.

Fortunately, the advent of space-based observatories supplying high-precision, high-cadence, and long-duration photometry across large portions of the sky is providing accessible probes of the inner disk for hundreds of young stars. This comes in the form of the so-called "dipper" objects, which are young T Tauri stars hosting protoplanetary disks with optical light curves that exhibit very deep ($\sim$10–90% in flux) and short-duration ($\sim$0.5-3 day) dimming events. Some examples of dipper light curves are shown in Figure 4.3, which also illustrates that the dips can be either quasi-periodic (i.e., appearing at regular intervals, but with varying shapes and depths) or aperiodic (i.e., appearing stochastically and with varying shapes and depths). Dippers were first identified by the CoRoT and *Spitzer* missions while they were surveying the young ($\sim$2–3 Myr) ONC (Morales-Calderón et al. 2011) and NGC 2264 region (Alencar et al. 2010; Cody et al. 2014). These studies found that dippers nearly always host protoplanetary disks, and that the depth, duration, and periodicity of the dips are consistent with large dusty structures orbiting in the inner ($\ll$ 1 AU) disk regions and transiting our line-of-sight to the host star.

McGinnis et al. (2015) proposed that the dips are due to transiting inner disk warps driven by accretion streams onto the star, where the quasi-periodic dippers could be explained by stable accretion regimes and the aperiodic dippers could be explained by unstable accretion regimes (Kurosawa & Romanova 2013). In this scenario, dipper disks
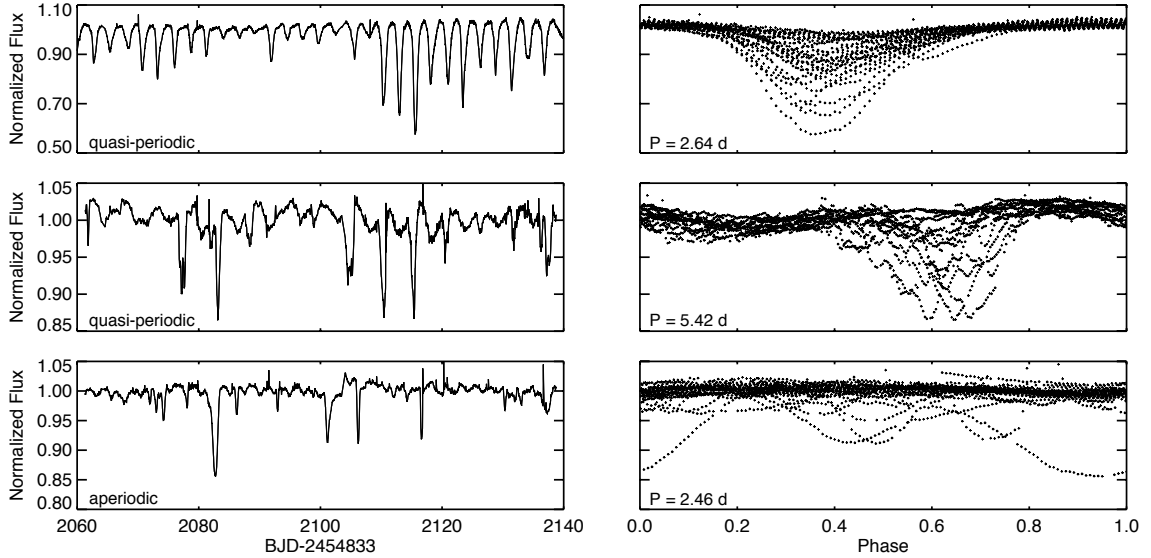
Figure 4.3 *Left:* example light curves of dippers taken by *K2*. Dippers exhibit very deep (~10–90% in flux) and short-duration (~0.5-3 day) dimming events, often super-imposed over other variability commonly seen in the light curves of young stars, namely sinusoidal modulations from star spot rotation and flaring events related to accretion. *Right:* light curves phase-folded to the derived rotational period, illustrating that the dips can be either quasi-periodic (appearing at regular intervals, but with varying shapes and depths) or aperiodic (appearing stochastically and with varying shapes and depths).

are being seen at nearly edge-on orientations ($i \approx 70$–$80°$), with the observed transits occurring because the disk warps lift material above the disk midplane at the co-rotation radius, allowing the dust to cross our line-of-sight (completely edge-on orientations with $i \approx 90°$ are ruled out, as the disk would completely obscure the star). This scenario, however, conflicts with the high occurrence rate of dippers (e.g., ~20–30% of star-disk systems in NGC 2264), if disk inclinations are assumed to be randomly oriented on the sky. Unfortunately, the significant distances to these regions (~400–750 pc) limited follow-up observations needed to confirm the prediction of nearly edge-on disk orientations combined with accretion-driven disk warps.

To this end, we have been identifying and characterizing dippers in nearby star-forming regions using the re-purposed *Kepler* mission, *K2* (Howell et al. 2014). The primary mission of the *Kepler* spacecraft—to provide very high-precision (ppm) optical photometry of solar-

type stars to search for transiting Earth-like planets—ended in 2013 May when the failure of two of its four reaction wheels meant that the spacecraft could no longer maintain the sufficiently accurate pointing needed to meet its original science goals. The re-purposed *K2* mission employs an ecliptic-observing orientation, such that solar radiation pressure is used as an effective third reaction wheel to stabilize pointing. This approach limits observations to regions along the ecliptic, and also limits observing campaigns to 80-days, after which the telescope must alter its pointing in order to continue using solar radiation pressure as a pointing stabilizer. Vanderburg & Johnson (2014) developed a self field flattening (SFF) technique to correct for residual spacecraft motion, restoring the *K2* photometric precision to within a factor of two of the original *Kepler* capabilities. The *K2*/SFF light curves are publicly available on the Mikulski Archive for Space Telescopes (MAST).[1]

During the course of this thesis, *K2* observed the Upper Sco and ρ Oph star-forming regions during its Campaign 2 (*K2*/C2). Both regions are relatively nearby at ∼145 pc (de Zeeuw et al. 1999) and ∼120 pc (Loinard et al. 2008), respectively, but have significantly different ages at ∼5–10 Myr (Pecaut et al. 2012) and ∼1 Myr (Andrews & Williams 2007), respectively. In Ansdell et al. (2016a), we mined the *K2* data to identify dipper objects in these regions. We first normalized the publicly available *K2*/SFF light curves, then applied a high-pass filter with a cut-on frequency of 1 day^{-1}, which highlighted the quasi-periodic and aperiodic dimming events while suppressing the periodic variability from stellar rotation due to their different duty cycles. We then used the normalized and filtered light curves to compute several metrics that efficiently identify bona fide dippers while ignoring noisy sources (see Ansdell et al. 2016a for a detailed description of the selection criteria). We also estimated stellar rotation periods ($P_{\rm rot}$) using the Lomb-Scargle periodogram (Scargle 1987) on the normalized light curves. The derived $P_{\rm rot}$ values are all consistent with the stellar rotation periods of young late-type stars (i.e., $\lesssim$ 10 days; Herbst et al. 2007), although they may also be influenced by the dimming events.

---

[1]https://archive.stsci.edu/prepds/k2sff/

To further investigate the nature of the dippers identified in $K2$/C2, we obtained: optical and near-IR spectra to determine stellar properties and identify accretion signatures; adaptive optics imaging to search for close companions that could cause optical variations and/or influence disk evolution; (sub-)mm observations to constrain disk dust and gas masses; and archival photometry from all-sky surveys such as the Two Micron All-Sky Survey (2MASS; Skrutskie et al. 2006) and the Wide-field Infrared Survey Explorer (WISE; Wright et al. 2010) for modeling SEDs. Ansdell et al. (2016a) provide a full analysis of these data. In short, the spectra reveal Li I absorption and Hα emission consistent with stellar youth (< 50 Myr), but also low accretion rates indicative of weak-line T Tauri stars for many dippers. IR excesses in the SEDs are consistent with the existence of circumstellar disks; however, the (sub-)mm observations imply intermediate disk dust masses of $\sim$4–15 $M_\oplus$, which are an order of magnitude lower than the most massive protoplanetary disks at $\sim 10^2$ $M_\oplus$, although still an order of magnitude higher than typical debris disks at $\sim 10^{-1}$ $M_\oplus$ (see Figure 3 in Wyatt 2008). Although the AO data reveal close companions for some dippers, binarity does not appear to play a key role in producing dipper behavior.

Thus, apart from their optical light curves, dippers appear to be relatively normal T Tauri stars hosting protoplanetary disks. However, the low accretion rates and moderate disk masses found in our follow-up observations of the $K2$ dippers bring into question the universal application of the accretion-driven disk warp scenario proposed by McGinnis et al. (2015). This scenario made sense in the context of the younger ONC and NGC 2264 region, which are dominated by strongly accreting classical T Tauri stars. Yet the existence of dippers among moderately evolved and weakly accreting disks suggests that other mechanisms must also be at play. Below we identify two trends with stellar and disk properties that can give insight into the potential mechanisms driving dipper behavior.

First, the vast majority of the $K2$ dippers are late-K or M dwarf stars (Ansdell et al. 2016a). This is unlikely to be the result of the community-based selection of the $K2$/C2 sample: of the $\sim$13,000 long-cadence targets, only $\sim$55% have $K_\mathrm{p} - J > 1.8$, which is approximately the late-K and M dwarf regime. Thus the probability of picking ten random
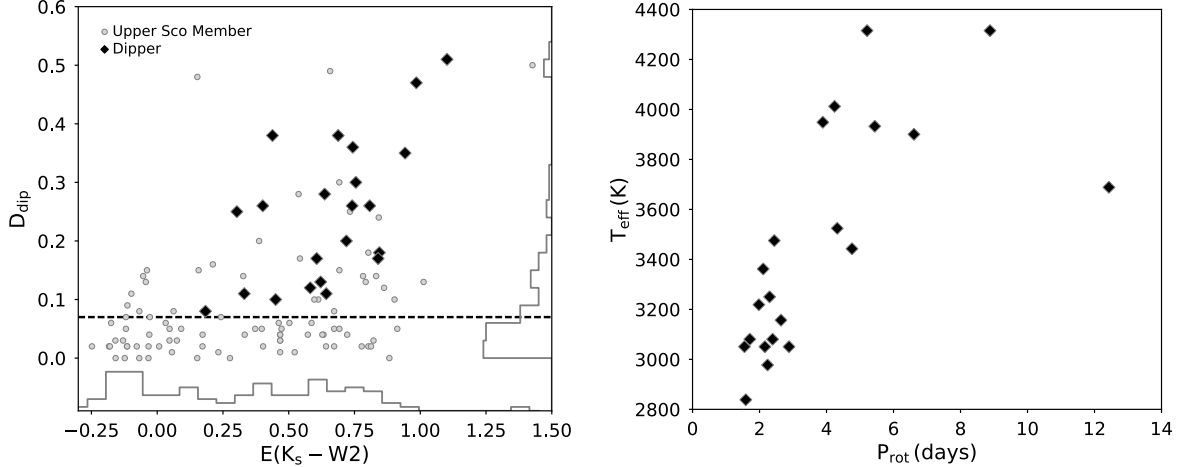
Figure 4.4 Correlations with stellar and disk properties seen among the *K2* dippers identified in Ansdell et al. (2016a). *Left:* Correlation between dip depth (D_{dip}) and W2 excess (E(K_{S}−W2)) seen for dippers (black diamonds). All late-type Upper Sco members that were also observed during *K2*/C2 (gray points and histogram; taken from Luhman & Mamajek 2012) are shown for comparison to illustrate that a similar correlation does not exist for the general population. The dashed line shows our D_{dip} cutoff used as one of the criteria for dipper identification. *Right:* Correlation between stellar effective temperature (T_{eff}) and rotation period (P_{rot}). P_{rot} values were derived from *K2* light curves, while T_{eff} values were estimated from stellar spectral types (Ansdell et al. 2016a; Bodman et al. 2016) using the relations for PMS stars derived in Herczeg & Hillenbrand (2014).

stars and having them all be late-K or M dwarfs is only $\sim 0.1\%$. Moreover, the dippers in NGC 2264 are also dominated by late-type stars (McGinnis et al. 2015), while spectral types were not provided for ONC dippers in Morales-Calderón et al. 2011. Rather, this bias toward late-type stars could result from the dipper phenomenon being related to circumstellar material, as disks persist significantly longer around low-mass stars compared to high-mass stars (e.g. Ribas et al. 2015). The bias toward late-type stars may also imply that the dips are related to circumstellar material located at a specific distance from the star where a given temperature is reached; this is because the lower stellar luminosities of late-type stars mean that such temperature-dependent disk components would exist closer to the star, where transiting orbits are more likely. Indeed, we find a positive correlation between P_{rot} and T_{eff} in our *K2* dipper sample: as shown in Figure 4.4, the cooler systems have $P_{\mathrm{rot}} \sim 2$–3 days, while the hottest systems have $P_{\mathrm{rot}} \sim 4$–10 days (a Spearman rank

test gives a correlation coefficient of $\rho = 0.81$, and a probability of 4×10^{-6} for the null hypothesis of no correlation). Interestingly, dust grains orbiting at the co-rotation radii of these stars would therefore have similar temperatures of $\sim$600–700 K (assuming Keplerian rotation and radiative equilibrium of dust grains around $\sim$10 Myr old YSOs).

We also find a positive correlation between the dip depth (D_{dip}) and WISE-2 (W2) excess emission above the stellar photosphere (E($K_{\mathrm{S}} - $W2)) for the $K2$ dippers. D_{dip} is calculated by averaging the three deepest dips seen in the $K2$ light curve, while E($K_{\mathrm{S}} - $W2 is calculated following the method of Luhman & Mamajek (2012) and is an indicator of warm dusty material in the inner disk. Figure 4.4 shows the positive correlation found for dippers (a Spearman rank test gives $\rho = 0.55$ with a p-value of 0.01) as well as the non-correlation found among the general population of late-type Upper Sco members observed during $K2$/C2. We interpret this as evidence that the dipper phenomenon is related to dusty structures in the inner disk: emission in the W2 band (4.6 μm) corresponds to blackbody temperatures of $\sim$600 K, which is roughly the temperature of dust grains orbiting at the co-rotation radius (i.e., a few stellar radii) around late-K and M dwarfs, as illustrated by the P_{rot}–T_{eff} relation discussed above. We also note that similar correlations with dip depth are *not* found for W3 and W4 excess, as this corresponds to emission from the cooler dust further out in the disk.

In Ansdell et al. (2016a) we used the above information and order-of-magnitude arguments to present three possible mechanisms for explaining the dipper phenomenon: (1) inner disk warps near the co-rotation radius related to magnetospheric accretion; (2) vortices at the inner disk edge produced by the Rossby Wave Instability (RWI); and (3) clumps of circumstellar material related to planetesimal formation at a few AU (see Ansdell et al. 2016a for detailed discussions of each mechanism). Each of these mechanisms are related to dusty circumstellar material passing through our line-of-sight to the star and assume nearly edge-on disk orientations. No single mechanism alone can explain all the known dippers, but collectively these mechanisms can account for the range of observed dipper properties. For the quasi-periodic dippers, the transiting clump scenario is clearly ruled out

as orbits near the co-rotation radius are needed to reproduce the regular dimming events with short periods. Rather, the quasi-periodic dippers are likely explained by occulting inner disk warps or RWI-driven vortices; however, the requirement of accretion in the disk warp scenario may make RWI-driven vortices a more likely explanation for the quasi-periodic dippers with low disk masses and weak accretion signatures. Given the diversity of the dipper light curves, it could be that the dippers are produced by different mechanisms that correspond to different stages of disk evolution.

In an effort to relate these findings to the overall disk structure, Ansdell et al. (2016b) mined the ALMA archive to identify any known dippers with resolved (sub-)mm images that can be used to constrain disk inclinations and sizes. Interestingly, they found that the three dippers with resolved ALMA images spanned the full range of disk inclinations, from a face-on ($i = 6°$) to moderately inclined ($i = 53°$) to nearly edge-on ($i = 73°$). Figure 4.5 shows their *K2* light curves as well as their ALMA images and visibilities. This suggests that nearly edge-on viewing geometries are *not* a defining characteristic of the dippers, and also points to inner disk processes that regularly produce dusty structures far above the outer disk mid-plane in regions relevant to planet formation.

EPIC 204638512 is a particularly interesting case. This star hosts a face-on disk ($i = 6° \pm 1.5°$; Mathews et al. 2012a) with a large sub-mm dust cavity ($\sim$80 AU in radius; Zhang et al. 2014), which seemingly makes it an unlikely dipper. Yet, EPIC 204638512 exhibits some of the deepest flux dips among the known *K2* dippers (up to $\sim$60%; Figure 4.5). The dipper activity for this star may be related to an inclined and variable inner dust disk, as implied from its IR emission: the *Spitzer* IRAC photometry shows no excess (Mathews et al. 2012a), while the *Spitzer* IRS spectrum and WISE photometry reveal excesses consistent with dust at small ($\lesssim$0.1 AU) orbital radii (Dahm 2010; Zhang et al. 2014). A factor of four variability in mid-IR flux was also seen over several weeks, indicating a rapidly changing inner dust disk (Dahm & Carpenter 2009). Moreover, Takami et al. (2014) used near-IR imaging polarimetry to identify intensity nulls in the outer disk annulus, which could be self-shadowing from a misaligned inner disk. An inclined and
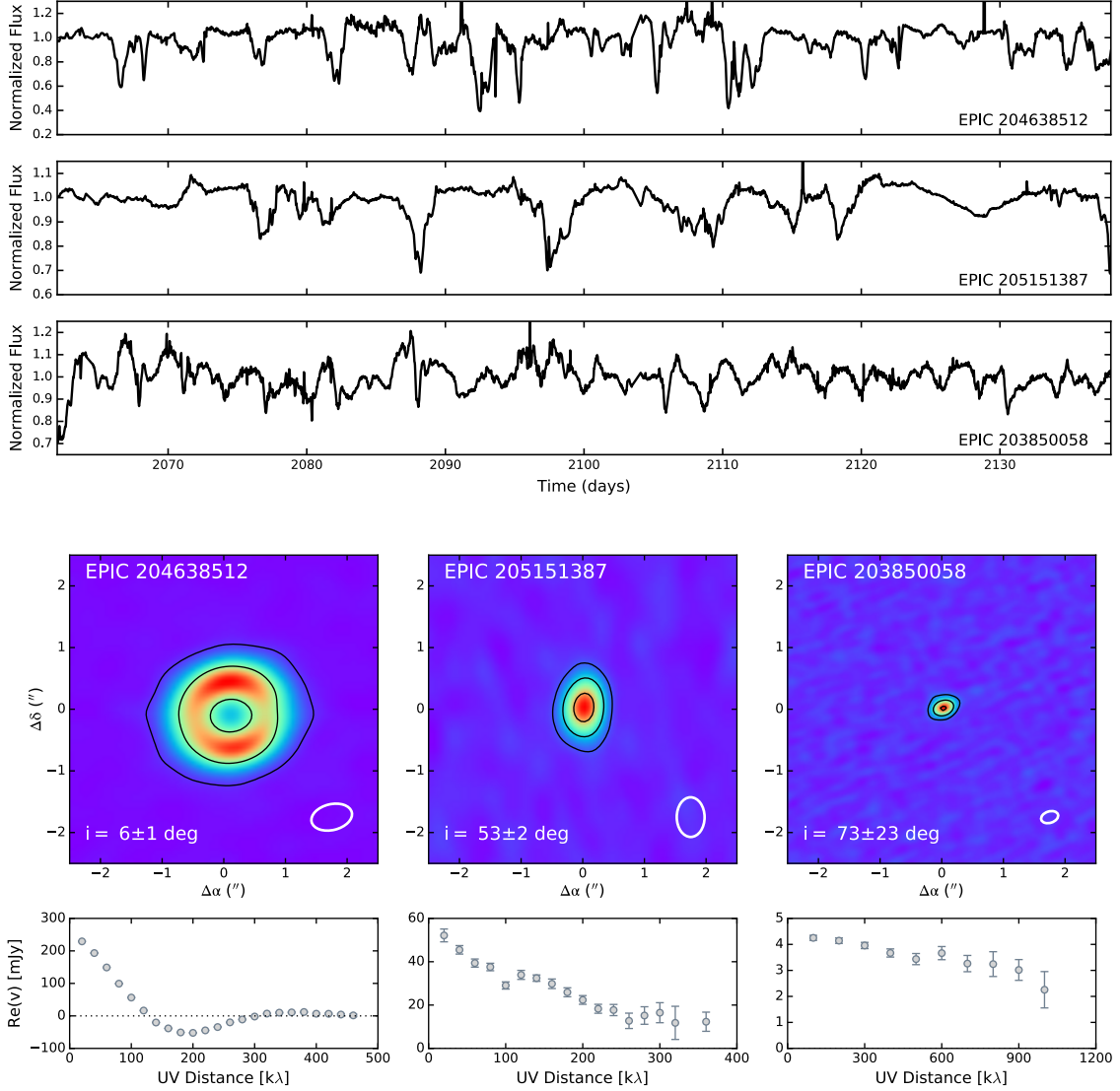
Figure 4.5 Dippers with resolved archival ALMA images. *Top:* normalized *K2* light curves showing $\gtrsim 10\%$ dip depths with ∼0.5–2 day durations typical of dippers. *Middle:* ALMA continuum images ($5'' \times 5''$) with fitted disk inclinations and beam sizes; contours are 10σ and 100σ for EPIC 204638512 and 5σ, 20σ, and 50σ for EPIC 205151387 and EPIC 203850058. *Bottom:* real part of the visibilities as a function of projected baseline length; the decrease in amplitude with projected baseline length is an indicator of a resolved source.

variable inner disk has been proposed for HD 142527, which also hosts a face-on disk with a large inner dust gap (Fukagawa et al. 2006) as well as intensity nulls along the outer disk annulus in its IR scattered light images (Casassus et al. 2012). Marino et al. (2015) modeled the system, finding a relative inclination of ∼ 70° between the inner and outer disks, possibly

due to dynamical interactions with a low-mass stellar companion orbiting inside the dust gap (Biller et al. 2012; Rodigas et al. 2014; Close et al. 2014). Unfortunately HD 142527 does not have a *K2* light curve to check for dipper behavior, although a similar scenario for EPIC 204638512 would reconcile its dips and face-on outer disk. Interestingly, the dust cavity of EPIC 204638512 is thought to have been cleared by giant planet(s) orbiting inside the dust gap (Mathews et al. 2012a; Zhang et al. 2014; van der Marel et al. 2015), and these planet(s) may also be driving an inclined inner disk that is causing the dipper behavior.

In summary, the dippers provide a rare probe into the inner regions of protoplanetary disks. The initial comparisons to the outer disk geometry discussed in this section suggest that the inner disk is a dynamically active region, with material commonly being lifted far above the disk mid-plane, likely by a combination of various mechanisms. Consequently, the geometry of the inner disk may not necessarily follow a smooth extrapolation from the outer disk. Resolving more dipper disks with ALMA, and exploring techniques such as spectro-astrometry that can directly probe the inner disk (e.g. Pontoppidan et al. 2008), will be essential to connecting the inner and outer disk regions in a coherent picture of global disk evolution and planet formation.

4.3   Future Work

4.3.1   Studying External Photoevaporation with λ Orionis

A key result from our ALMA survey of the σ Orionis cluster (§2.3) was the effect of external photoevaporation driven by the central O9V star, σ Ori (§3.3). Specifically, we found that M_{dust} clearly declines with proximity to σ Ori, and that CO gas detections only exist beyond ∼1.5 pc (Figures 3.3 & 3.4). These findings support recent theoretical predictions that even moderate FUV fields can induce significant photoevaporative winds that are more efficient at depleting gas relative to large ($\gtrsim$ 1 mm) dust grains (Facchini et al. 2016). However, our findings were also somewhat unexpected given the earlier ALMA survey of the younger (∼1–2 Myr) ONC, which showed reduced proplyd masses only within ∼0.03 pc of the central

O6V star (Mann et al. 2014). The more significant effects of external photoevaporation in σ Orionis can be explained by its older age (allowing more time for mass loss to occur) as well as its lack of intra-cluster cloud material (which would otherwise shield disks from the UV radiation). However, because the other disk populations surveyed by ALMA are in low-mass star-forming regions, it is critical to survey more OB clusters in order to understand the effects of external photoevaporation on disk evolution.

The λ Orionis cluster is a key target for studying the role of external photoevaporation in disk evolution. At its evolved age ($\sim$5 Myr; Dolan & Mathieu 2001) and relative proximity ($\sim$400 pc; Murdin & Penston 1977), the cluster contains 465 members centered on a core of OB stars, the most massive of which is the λ Ori star of O8III spectral type. There is low reddening towards the cluster (E(B-V)$\sim$0.12; Diplas & Savage 1994), which is currently located in a region devoid of cloud material, possibly cleared by a supernova that occurred $\sim$1 Myr ago near the λ Ori star. The cluster hosts 59 circumstellar disks (Hernández et al. 2009, 2010) for a disk fraction of $\sim$13% (59/465), consistent with its evolved age (see Fig. 1.2). We previously used JCMT/SCUBA-2 to conduct a single-dish survey at 850 μm of the inner $\sim$0°.5 region centered on λ Ori, covering 36 of the 59 disks (Ansdell et al. 2015). Our sensitivity of 3.0 mJy beam^{-1} ($\sim$6 $M_\oplus$) produced only one disk detection, the Herbig Ae star HD 245185, with a flux density of 74$\pm$3 mJy beam^{-1} ($\sim$150 $M_\oplus$). Stacking the undetected sources showed that the average λ Orionis disk has a flux density $\leq$1.4 mJy beam^{-1} ($\sim$3 $M_\oplus$). Thus HD 245185 is a clear outlier in λ Orionis, and its ability to maintain its massive disk may be related to giant planet formation (Ansdell et al. 2015).

These characteristics of the λ Orionis cluster make it a uniquely ideal target for studying the influence of OB stars on disk evolution and thus planet formation. In particular, its evolved age and lack of intra-cluster material mean that external photoevaporation effects will be significant, based on our results from σ Orionis. Moreover, its central O8III star emits an ionizing radiation flux very similar to the O6V star in the ONC ($\Delta log(Q_{\rm H}) \approx 0.2$; Sternberg et al. 2003), which means we can use comparisons of their disk populations to inform external photoevaporation timescales under similar UV radiation

fields. Additionally, if a supernova did occur recently in λ Orionis, the region should be exposed to enhanced cosmic ray ionization rates; this would accelerate carbon processing of CO into other molecules (e.g., Eistrup et al. 2016), thereby adding to the gas depletion from external photoevaporation.

ALMA can be used to survey the 59 disks in λ Orionis, in both dust and gas, at sensitivities comparable to what we achieved for Lupus disks (§2.2). If a similar distance-dependent trend is found in λ Orionis, then the effects of external photoevaporation in OB clusters may be universal, with the corresponding implications for planet formation described above. If much lower dust masses and/or no gas detections are found, then this may indicate additional disk depletion from the recent supernova—opening a new parameter space that has not yet been explored by previous disk surveys. Moreover, these deeper observations in λ Orionis will be particularly important for constraining gas depletion due to external photoevaporation, as our sample of CO detections in σ Orionis was small and cloud confusion in the ONC (and similarly young regions) prohibits measurements of disk CO. If external photoevaporation does have a more significant effect on gas relative to dust, this would impact the types of planets that can form in OB associations.

4.3.2 Disentangling Gas and CO Depletion

Measuring the amount of gaseous material in protoplanetary disks as a function of age will provide fundamental constraints on disk evolution and planet formation timescales. However, deriving disk gas masses is proving to be more complicated than originally assumed as more detailed chemical observations are enabled by ALMA. Traditional estimates of disk gas mass extrapolate from the disk dust mass (as probed by (sub-)mm continuum emission) using the ISM gas-to-dust ratio of $\sim$100. This method is efficient, but requires an extrapolation that is not only large (two orders of magnitude) but also highly uncertain, as disks evolve quickly from gas-rich disks to dusty debris disks over $\sim$10 Myr timescales. In this work, we estimate disk gas mass from CO isotopologue emission (§2.1.2), as it is the best available probe of bulk disk gas content (since the most abundant gas-phase molecule,

H$_2$, cannot be observed due its lack of dipole moment). However, using CO to estimate disk gas mass is still complicated by the need to make a fundamental assumption on the abundance of volatile carbon; the WB14 models used in this work assume the ISM volatile carbon abundance, such that our low estimated disk gas masses could be due to carbon depletion mechanisms that are not yet well understood (§3.2).

Carbon depletion has been observationally explored for the handful of disks (TW Hydrae, DM Tau, GM Aur) where gas masses could be estimated from HD line fluxes prior to *Herschel* being decommissioned (Bergin et al. 2013; McClure et al. 2016). These studies have shown that volatile carbon may be depleted by up to two orders of magnitude with respect to ISM values, and a variety of chemical and physical mechanisms have been invoked to explain the depletion (§3.2). However, these studies are extremely biased towards the very brightest disks where HD could be detected with *Herschel*/PACS, and the derived gas masses depend strongly on fundamental model inputs such as the vertical disk structure (Trapman et al. 2017). With the next far-IR space mission several decades off, alternative diagnostics are needed to test for carbon depletion in a wider variety of disks that are better representations of the typical pathways to planet formation.

There are two clear methods for testing carbon depletion via ALMA observations. The first is to measure the atomic carbon [C I] $J = 1$–0 line at 610 μm, which arises from the upper layers of protoplanetary disk atmospheres due to irradiation from UV and X-ray photons from the host star. Since the turbulent vertical mixing time is much shorter than the chemical timescales for sequestering volatile carbon (Kama et al. 2016b), the upper disk layers (where we detect [C I]) are expected to show the same overall volatile carbon depletion as the lower warm molecular layers (where we detect CO). Predictions of [C I] emission indicate that the total flux is highly sensitive to the total volatile carbon abundance, with a much shallower dependence on disk mass (e.g., Figure 8 in Miotello et al. 2016). Thus observed [C I] line fluxes can be used to distinguish between gas and carbon depletion (e.g., Kama et al. 2016b). Lupus disks provide the best available sample for such observations because these targets already have well-constrained stellar properties (masses,

luminosities, accretion rates; Alcalá et al. 2014, 2017) and disk properties (dust mass and size, scale height; Ansdell et al. 2016c, Tazzari et al. submitted), which are needed to correctly interpret the [C I] observations. ALMA can be used to measure C I line fluxes for all 36 Lupus disks in our ALMA survey detected in ^{13}CO (§2.2.5), allowing us to study the volatile carbon budget in a statistically significant sample. In particular, we can test whether the large range of gas-to-dust ratios derived based on CO isotopologue emission (from 0.1 to 100; §2.2.5) correlates with [C I] line fluxes and thus is likely due to different volatile carbon abundances rather than gas depletion.

The second method is to observe more complex carbon-bearing molecules, such as C_2H and C_3H_2, whose abundances are particularly sensitive to carbon abundance and the [C]/[O] ratio. This is because one method of volatile carbon depletion is thought to be X-ray and cosmic ray ionization of He, which produces He^+ atoms that react with gaseous CO to extract carbon, processing it into more complex molecules that freeze out onto dust grains at higher temperatures than CO (e.g., Aikawa et al. 1997; Bergin et al. 2014). This mechanism also removes volatile oxygen more efficiently than volatile carbon due to freeze out of H_2O, CO_2, and CO resulting in atomic ratios of [C]/[O]> 1 (Öberg & Bergin 2016). Thus carbon depletion can be tested by comparing our observations of CO isotopologues to species like C_2H and C_3H_2, whose line emission will be brighter for disks with lower-than-ISM volatile carbon abundances and [C]/[O]> 1 ratios; indeed, C_2H has been found to be strong in the TW Hydrae disk (Bergin et al. 2016). ALMA can be used to measure C_2H and C_3H_2 line fluxes for the 36 Lupus disks with ^{13}CO detections (§2.2.5). Anti-correlations with ^{13}CO line fluxes or continuum fluxes would suggest carbon depletion is indeed the basis for the low CO emission seen in our ALMA surveys.

4.4   Conclusions

Prior to ALMA, (sub-)mm observers were restricted to studying only the brightest disks in the sky, which likely do not represent the most common pathways to planet formation. This

work has shown the power of large-scale ALMA surveys for constraining the properties of "typical" protoplanetary disks, thereby improving our understanding of disk evolution and ultimately planet formation. Future ALMA surveys at higher resolution and sensitivity, as well as more detailed modeling of the observed disks, will be important for providing insight into the many open questions that still remain with respect to how protoplanetary disks evolve into the observed exoplanet population.

References

Adams, F. C. 2010, ARA&A, 48, 47 4.1.1

Adams, F. C., Hollenbach, D., Laughlin, G., & Gorti, U. 2004, ApJ, 611, 360 3.3

Aikawa, Y., Umebayashi, T., Nakano, T., & Miyama, S. M. 1997, ApJ, 486, L51 3.2, 4.3.2

Aikawa, Y., van Zadelhoff, G. J., van Dishoeck, E. F., & Herbst, E. 2002, A&A, 386, 622 2.1.2

Alcalá, J. M., Manara, C. F., Natta, A., Frasca, A., Testi, L., Nisini, B., Stelzer, B., Williams, J. P., Antoniucci, S., Biazzo, K., Covino, E., Esposito, M., Getman, F., & Rigliaco, E. 2017, A&A, 600, A20 2.2.1, 2.2.2, 4.2.1, 4.3.2

Alcalá, J. M., Natta, A., Manara, C. F., Spezzi, L., Stelzer, B., Frasca, A., Biazzo, K., Covino, E., Randich, S., Rigliaco, E., Testi, L., Comerón, F., Cupani, G., & D'Elia, V. 2014, A&A, 561, A2 2.2.1, 2.2.2, 4.2.1, 4.3.2

Alencar, S. H. P., Teixeira, P. S., Guimarães, M. M., McGinnis, P. T., Gameiro, J. F., Bouvier, J., Aigrain, S., Flaccomio, E., & Favata, F. 2010, A&A, 519, A88 4.2.2

Alexander, R., Pascucci, I., Andrews, S., Armitage, P., & Cieza, L. 2014, Protostars and Planets VI, 475 2.2.6, 2.3.6, 3.2

Alexander, R. D., Clarke, C. J., & Pringle, J. E. 2006, MNRAS, 369, 229 4.1.1

Alibert, Y., Mordasini, C., & Benz, W. 2011, A&A, 526, A63 1.1.3

Anderson, K. R., Adams, F. C., & Calvet, N. 2013, ApJ, 774, 9 3.3

Andrews, S. M., Rosenfeld, K. A., Kraus, A. L., & Wilner, D. J. 2013, ApJ, 771, 129 1.1.3, 2.1.1, 2.4.1, 3, 3.1, 3.1.1, 3.1.2, 4.1.2

Andrews, S. M. & Williams, J. P. 2005, ApJ, 631, 1134 (document), 1.3, 1.1.2, 2.1.1, 2.4.1, 3

—. 2007, ApJ, 671, 1800 (document), 1.3, 1.1.2, 4.2.2

Andrews, S. M., Wilner, D. J., Espaillat, C., Hughes, A. M., Dullemond, C. P., McClure, M. K., Qi, C., & Brown, J. M. 2011, ApJ, 732, 42 2.2.2

Andrews, S. M., Wilner, D. J., Hughes, A. M., Qi, C., & Dullemond, C. P. 2010, ApJ, 723, 1241 4.2.1

Ansdell, M., Gaidos, E., Rappaport, S. A., Jacobs, T. L., LaCourse, D. M., Jek, K. J., Mann, A. W., Wyatt, M. C., Kennedy, G., Williams, J. P., & Boyajian, T. S. 2016a, ApJ, 816, 69 (document), 4.2.2, 4.2.2, 4.4

Ansdell, M., Gaidos, E., Williams, J. P., Kennedy, G., Wyatt, M. C., LaCourse, D. M., Jacobs, T. L., & Mann, A. W. 2016b, MNRAS, 462, L101 4.2.2

Ansdell, M., Williams, J. P., & Cieza, L. A. 2015, ApJ, 806, 221 (document), 1.3, 1.1.2, 3, 4.3.1

Ansdell, M., Williams, J. P., Manara, C. F., Miotello, A., Facchini, S., van der Marel, N., Testi, L., & van Dishoeck, E. F. 2017, AJ, 153, 240 (document), 3.1.1, 3.1.2, 4.2

Ansdell, M., Williams, J. P., van der Marel, N., Carpenter, J. M., Guidi, G., Hogerheijde, M., Mathews, G. S., Manara, C. F., Miotello, A., Natta, A., Oliveira, I., Tazzari, M., Testi, L., van Dishoeck, E. F., & van Terwisga, S. E. 2016c, ApJ, 828, 46 (document), 2.2.3, 3.1.1, 3.2, 3.1.2, 3.1, 4.3.2

Bai, X.-N. 2016, ApJ, 821, 80 3.2

Baraffe, I., Homeier, D., Allard, F., & Chabrier, G. 2015, A&A, 577, A42 3.1

Barenfeld, S. A., Carpenter, J. M., Ricci, L., & Isella, A. 2016, ApJ, 827, 142 2.1.1, 2.4.2, 3.1, 3.1.1, 3.1.2

Beckwith, S. V. W., Sargent, A. I., Chini, R. S., & Guesten, R. 1990, AJ, 99, 924 1.1.2, 2.1.1, 3

Bell, C. P. M., Naylor, T., Mayne, N. J., Jeffries, R. D., & Littlefair, S. P. 2013, MNRAS, 434, 806 1.1.1, 3.1

Bergin, E. A., Cleeves, L. I., Crockett, N., & Blake, G. A. 2014, Faraday Discussions, 168 3.2, 4.3.2

Bergin, E. A., Cleeves, L. I., Gorti, U., Zhang, K., Blake, G. A., Green, J. D., Andrews, S. M., Evans, II, N. J., Henning, T., Öberg, K., Pontoppidan, K., Qi, C., Salyk, C., & van Dishoeck, E. F. 2013, Nature, 493, 644 2.1.2, 3.2, 4.3.2

Bergin, E. A., Du, F., Cleeves, L. I., Blake, G. A., Schwarz, K., Visser, R., & Zhang, K. 2016, ApJ, 831, 101 4.3.2

Bergin, E. A., Hogerheijde, M. R., Brinch, C., Fogel, J., Yıldız, U. A., Kristensen, L. E., van Dishoeck, E. F., Bell, T. A., Blake, G. A., Cernicharo, J., Dominik, C., Lis, D., Melnick, G., Neufeld, D., Panić, O., Pearson, J. C., Bachiller, R., Baudry, A., Benedettini, M., Benz, A. O., Bjerkeli, P., Bontemps, S., Braine, J., Bruderer, S., Caselli, P., Codella, C., Daniel, F., di Giorgio, A. M., Doty, S. D., Encrenaz, P., Fich, M., Fuente, A., Giannini, T., Goicoechea, J. R., de Graauw, T., Helmich, F., Herczeg, G. J., Herpin, F., Jacq, T., Johnstone, D., Jørgensen, J. K., Larsson, B., Liseau, R., Marseille, M., McCoey, C., Nisini, B., Olberg, M., Parise, B., Plume, R., Risacher, C., Santiago-García, J., Saraceno, P., Shipman, R., Tafalla, M., van Kempen, T. A., Visser, R., Wampfler, S. F., Wyrowski, F., van der Tak, F., Jellema, W., Tielens, A. G. G. M., Hartogh, P., Stützki, J., & Szczerba, R. 2010, A&A, 521, L33 3.2

Bik, A., Lenorzer, A., Kaper, L., Comerón, F., Waters, L. B. F. M., de Koter, A., & Hanson, M. M. 2003, A&A, 404, 249 3.3

Biller, B., Lacour, S., Juhász, A., Benisty, M., Chauvin, G., Olofsson, J., Pott, J.-U., Müller, A., Sicilia-Aguilar, A., Bonnefoy, M., Tuthill, P., Thebault, P., Henning, T., & Crida, A. 2012, ApJ, 753, L38 4.2.2

Birnstiel, T., Klahr, H., & Ercolano, B. 2012, A&A, 539, A148 3.1.2, 4.1.1

Bitsch, B., Johansen, A., Lambrechts, M., & Morbidelli, A. 2015, A&A, 575, A28 1.1.3

Bodman, E. H. L., Quillen, A. C., Ansdell, M., Hippke, M., Boyajian, T. S., Mamajek, E. E., Blackman, E. G., Rizzuto, A., & Kastner, J. H. 2016, ArXiv e-prints (document), 4.4

Bohlin, R. C., Savage, B. D., & Drake, J. F. 1978, ApJ, 224, 132 1.1.2, 3.2

Bonfils, X., Delfosse, X., Udry, S., Forveille, T., Mayor, M., Perrier, C., Bouchy, F., Gillon, M., Lovis, C., Pepe, F., Queloz, D., Santos, N. C., Ségransan, D., & Bertaux, J.-L. 2013, A&A, 549, A109 3.1.2

Borucki, W. J., Koch, D., Basri, G., Batalha, N., Brown, T., Caldwell, D., Caldwell, J., Christensen-Dalsgaard, J., Cochran, W. D., DeVore, E., Dunham, E. W., Dupree, A. K., Gautier, T. N., Geary, J. C., Gilliland, R., Gould, A., Howell, S. B., Jenkins, J. M., Kondo, Y., Latham, D. W., Marcy, G. W., Meibom, S., Kjeldsen, H., Lissauer, J. J., Monet, D. G., Morrison, D., Sasselov, D., Tarter, J., Boss, A., Brownlee, D., Owen, T., Buzasi, D., Charbonneau, D., Doyle, L., Fortney, J., Ford, E. B., Holman, M. J., Seager, S., Steffen, J. H., Welsh, W. F., Rowe, J., Anderson, H., Buchhave, L., Ciardi, D., Walkowicz, L., Sherry, W., Horch, E., Isaacson, H., Everett, M. E., Fischer, D., Torres, G., Johnson, J. A., Endl, M., MacQueen, P., Bryson, S. T., Dotson, J., Haas, M., Kolodziejczak, J., Van Cleve, J., Chandrasekaran, H., Twicken, J. D., Quintana, E. V., Clarke, B. D., Allen, C., Li, J., Wu, H., Tenenbaum, P., Verner, E., Bruhweiler, F., Barnes, J., & Prsa, A. 2010, Science, 327, 977 1.1.3, 4.1.2

Bowler, B. P., Johnson, J. A., Marcy, G. W., Henry, G. W., Peek, K. M. G., Fischer, D. A., Clubb, K. I., Liu, M. C., Reffert, S., Schwab, C., & Lowe, T. B. 2010, ApJ, 709, 396 1.1.3, 3.1.2, 4.1.2

Bowler, B. P., Liu, M. C., Shkolnik, E. L., & Tamura, M. 2015, ApJS, 216, 7 4.1.1

Bruderer, S., van Dishoeck, E. F., Doty, S. D., & Herczeg, G. J. 2012, A&A, 541, A91 3.2

Bustamante, I., Merín, B., Ribas, Á., Bouy, H., Prusti, T., Pilbratt, G. L., & André, P. 2015, A&A, 578, A23 2.2.2

Caballero, J. A. 2008, A&A, 478, 667 2.3.1, 2.3.2

Cambrésy, L. 1999, A&A, 345, 965 2.2.2

Carmona, A., van den Ancker, M. E., Henning, T., Pavlyuchenkov, Y., Dullemond, C. P., Goto, M., Thi, W. F., Bouwman, J., & Waters, L. B. F. M. 2008, A&A, 477, 839 2.1.2

Carpenter, J. M., Ricci, L., & Isella, A. 2014, ApJ, 787, 42 2.4.2

Casassus, S., Perez M., S., Jordán, A., Ménard, F., Cuadra, J., Schreiber, M. R., Hales, A. S., & Ercolano, B. 2012, ApJ, 754, L31 4.2.2

Cassan, A., Kubas, D., Beaulieu, J.-P., Dominik, M., Horne, K., Greenhill, J., Wambsganss, J., Menzies, J., Williams, A., Jørgensen, U. G., Udalski, A., Bennett, D. P., Albrow, M. D., Batista, V., Brillant, S., Caldwell, J. A. R., Cole, A., Coutures, C., Cook, K. H., Dieters, S., Prester, D. D., Donatowicz, J., Fouqué, P., Hill, K., Kains, N., Kane, S., Marquette, J.-B., Martin, R., Pollard, K. R., Sahu, K. C., Vinter, C., Warren, D., Watson, B., Zub, M., Sumi, T., Szymański, M. K., Kubiak, M., Poleski, R., Soszynski, I., Ulaczyk, K., Pietrzyński, G., & Wyrzykowski, Ł. 2012, Nature, 481, 167 4.1.1

Cieza, L. A., Olofsson, J., Harvey, P. M., Evans, II, N. J., Najita, J., Henning, T., Merín, B., Liebhart, A., Güdel, M., Augereau, J.-C., & Pinte, C. 2013, ApJ, 762, 100 4.1.1

Clarke, C. J. 2007, MNRAS, 376, 1350 3.3

Clarke, C. J., Gendrin, A., & Sotomayor, M. 2001, MNRAS, 328, 485 4.1.1

Cleeves, L. I., Öberg, K. I., Wilner, D. J., Huang, J., Loomis, R. A., Andrews, S. M., & Czekala, I. 2016, ApJ, 832, 110 (document), 2.2.3, 2.2.4, 2.2.5, 2.3, 3.3

Close, L. M., Follette, K. B., Males, J. R., Puglisi, A., Xompero, M., Apai, D., Najita, J., Weinberger, A. J., Morzinski, K., Rodigas, T. J., Hinz, P., Bailey, V., & Briguglio, R. 2014, ApJ, 781, L30 4.2.2

Cody, A. M., Stauffer, J., Baglin, A., Micela, G., Rebull, L. M., Flaccomio, E., Morales-Calderón, M., Aigrain, S., Bouvier, J., Hillenbrand, L. A., Gutermuth, R., Song, I., Turner, N., Alencar, S. H. P., Zwintz, K., Plavchan, P., Carpenter, J., Findeisen, K., Carey, S., Terebey, S., Hartmann, L., Calvet, N., Teixeira, P., Vrba, F. J., Wolk, S., Covey, K., Poppenhaeger, K., Günther, H. M., Forbrich, J., Whitney, B., Affer, L., Herbst, W., Hora, J., Barrado, D., Holtzman, J., Marchis, F., Wood, K., Medeiros Guimarães, M., Lillo Box, J., Gillen, E., McQuillan, A., Espaillat, C., Allen, L., D'Alessio, P., & Favata, F. 2014, AJ, 147, 82 4.2.2

Comerón, F. 2008, The Lupus Clouds (Astronomical Society of the Pacific), 295 2.2.1, 2.2.2

Comerón, F., Fernández, M., Baraffe, I., Neuhäuser, R., & Kaas, A. A. 2003, A&A, 406, 1001 2.2.1

Connelly, J. N., Amelin, Y., Krot, A. N., & Bizzarro, M. 2008, ApJ, 675, L121 1.1.2

Dahm, S. E. 2010, AJ, 140, 1444 4.2.2

Dahm, S. E. & Carpenter, J. M. 2009, AJ, 137, 4024 4.2.2

D'Alessio, P., Calvet, N., Hartmann, L., Franco-Hernández, R., & Servín, H. 2006, ApJ, 638, 314 3.2

Dauphas, N. & Chaussidon, M. 2011, Annual Review of Earth and Planetary Sciences, 39, 351 (document), 1.1

de Zeeuw, P. T., Hoogerwerf, R., de Bruijne, J. H. J., Brown, A. G. A., & Blaauw, A. 1999, AJ, 117, 354 2.4.2, 4.2.2

Diplas, A. & Savage, B. D. 1994, ApJS, 93, 211 4.3.1

Dolan, C. J. & Mathieu, R. D. 2001, AJ, 121, 2124 4.3.1

Draine, B. T. 2006, ApJ, 636, 1114 1.1.2, 1.1.2, 3.1.2

—. 2011, Physics of the Interstellar and Intergalactic Medium (Princeton University Press) 2.1.1

Dressing, C. D. & Charbonneau, D. 2013, apj, 767, 95 1.1.3

—. 2015, ApJ, 807, 45 4.1.2

Du, F., Bergin, E. A., & Hogerheijde, M. R. 2015, ApJ, 807, L32 3.2

Dullemond, C. P. & Dominik, C. 2005, A&A, 434, 971 4.1.1

Dunham, M. M., Allen, L. E., Evans, II, N. J., Broekhoven-Fiene, H., Cieza, L. A., Di Francesco, J., Gutermuth, R. A., Harvey, P. M., Hatchell, J., Heiderman, A., Huard, T. L., Johnstone, D., Kirk, J. M., Matthews, B. C., Miller, J. F., Peterson, D. E., & Young, K. E. 2015, ApJS, 220, 11 2.2.2

Eistrup, C., Walsh, C., & van Dishoeck, E. F. 2016, A&A, 595, A83 3.2, 4.3.1

Endl, M., Cochran, W. D., Kürster, M., Paulson, D. B., Wittenmyer, R. A., MacQueen, P. J., & Tull, R. G. 2006, ApJ, 649, 436 1.1.3, 3.1.2, 4.1.2

Espaillat, C., Muzerolle, J., Najita, J., Andrews, S., Zhu, Z., Calvet, N., Kraus, S., Hashimoto, J., Kraus, A., & D'Alessio, P. 2014, in Protostars and Planets VI (University of Arizona Press), 497–520 1.1.1

Evans, II, N. J., Dunham, M. M., Jørgensen, J. K., Enoch, M. L., Merín, B., van Dishoeck, E. F., Alcalá, J. M., Myers, P. C., Stapelfeldt, K. R., Huard, T. L., Allen, L. E., Harvey,

P. M., van Kempen, T., Blake, G. A., Koerner, D. W., Mundy, L. G., Padgett, D. L., & Sargent, A. I. 2009, ApJS, 181, 321 1.1.1

Facchini, S., Clarke, C. J., & Bisbas, T. G. 2016, MNRAS, 457, 3593 3.3, 4.3.1

Fatuzzo, M. & Adams, F. C. 2008, ApJ, 675, 1361 3.3

Favre, C., Cleeves, L. I., Bergin, E. A., Qi, C., & Blake, G. A. 2013, ApJ, 776, L38 3.2

Fedele, D., van den Ancker, M. E., Henning, T., Jayawardhana, R., & Oliveira, J. M. 2010, A&A, 510, A72 3.2

Feigelson, E. D. & Babu, G. J. 2012, Modern Statistical Methods for Astronomy (Cambridge University Press) 3.1.2

Fischer, D. A. & Valenti, J. 2005, apj, 622, 1102 1.1.3

France, K., Herczeg, G. J., McJunkin, M., & Penton, S. V. 2014, ApJ, 794, 160 3.2

Frerking, M. A., Langer, W. D., & Wilson, R. W. 1982, ApJ, 262, 590 3.2

Fressin, F., Torres, G., Charbonneau, D., Bryson, S. T., Christiansen, J., Dressing, C. D., Jenkins, J. M., Walkowicz, L. M., & Batalha, N. M. 2013, apj, 766, 81 1.1.3

Fukagawa, M., Tamura, M., Itoh, Y., Kudo, T., Imaeda, Y., Oasa, Y., Hayashi, S. S., & Hayashi, M. 2006, ApJ, 636, L153 4.2.2

Gaidos, E., Mann, A. W., Kraus, A. L., & Ireland, M. 2016, MNRAS, 457, 2877 1.1.3

Galli, P. A. B., Bertout, C., Teixeira, R., & Ducourant, C. 2013, A&A, 558, A77 2.2.3

Gammie, C. F. 1996, ApJ, 457, 355 3.2

Goldsmith, P. F., Bergin, E. A., & Lis, D. C. 1997, ApJ, 491, 615 2.1.2

Gorti, U., Liseau, R., Sándor, Z., & Clarke, C. 2016, Space Sci. Rev., 205, 125 3.3

Guarcello, M. G., Drake, J. J., Wright, N. J., Albacete-Colombo, J. F., Clarke, C., Ercolano, B., Flaccomio, E., Kashyap, V., Micela, G., Naylor, T., Schneider, N., Sciortino, S., & Vink, J. S. 2016, ArXiv e-prints 3.3

Guidi, G., Tazzari, M., Testi, L., de Gregorio-Monsalvo, I., Chandler, C. J., Pérez, L., Isella, A., Natta, A., Ortolani, S., Henning, T., Corder, S., Linz, H., Andrews, S., Wilner, D., Ricci, L., Carpenter, J., Sargent, A., Mundy, L., Storm, S., Calvet, N., Dullemond, C., Greaves, J., Lazio, J., Deller, A., & Kwon, W. 2016, A&A, 588, A112 3.2

Guillot, T. 1999, Planet. Space Sci., 47, 1183 4.1.1

Habing, H. J. 1968, Bull. Astron. Inst. Netherlands, 19, 421 3.3

Haisch, Jr., K. E., Lada, E. A., & Lada, C. J. 2001, ApJ, 553, L153 1.1.1

Hand, E. 2011, Nature, 480, 302 4.1.1

Hardy, A., Caceres, C., Schreiber, M. R., Cieza, L., Alexander, R. D., Canovas, H., Williams, J. P., Wahhaj, Z., & Menard, F. 2015, A&A, 583, A66 4.1.1

Hartmann, L., Calvet, N., Gullbring, E., & D'Alessio, P. 1998, ApJ, 495, 385 4.1.2, 4.2.1

Haworth, T. J., Boubert, D., Facchini, S., Bisbas, T. G., & Clarke, C. J. 2016, MNRAS, 463, 3616 3.3

Haworth, T. J., Facchini, S., Clarke, C. J., & Cleeves, L. I. 2017, MNRAS accepted 3.3

Herbst, W., Eislöffel, J., Mundt, R., & Scholz, A. 2007, Protostars and Planets V, 297 4.2.2

Herczeg, G. J. & Hillenbrand, L. A. 2014, ApJ, 786, 97 (document), 4.4

—. 2015, ApJ, 808, 23 2.3.2

Hernández, J., Calvet, N., Hartmann, L., Muzerolle, J., Gutermuth, R., & Stauffer, J. 2009, ApJ, 707, 705 1.1.1, 4.3.1

Hernández, J., Calvet, N., Perez, A., Briceño, C., Olguin, L., Contreras, M. E., Hartmann, L., Allen, L., Espaillat, C., & Hernan, R. 2014, ApJ, 794, 36 2.3.1, 2.3.2

Hernández, J., Hartmann, L., Megeath, T., Gutermuth, R., Muzerolle, J., Calvet, N., Vivas, A. K., Briceño, C., Allen, L., Stauffer, J., Young, E., & Fazio, G. 2007, ApJ, 662, 1067 1.1.1, 2.3.1, 2.3.2, 3.3

Hernández, J., Morales-Calderon, M., Calvet, N., Hartmann, L., Muzerolle, J., Gutermuth, R., Luhman, K. L., & Stauffer, J. 2010, ApJ, 722, 1226 4.3.1

Hildebrand, R. H. 1983, QJRAS, 24, 267 1.1.2, 1.2, 2, 2.1.1

Hillenbrand, L. A., Bauermeister, A., & White, R. J. 2008, in Astronomical Society of the Pacific Conference Series, Vol. 384, 14th Cambridge Workshop on Cool Stars, Stellar Systems, and the Sun, ed. G. van Belle, 200 1.1.1

Hogerheijde, M. R., Bergin, E. A., Brinch, C., Cleeves, L. I., Fogel, J. K. J., Blake, G. A., Dominik, C., Lis, D. C., Melnick, G., Neufeld, D., Panić, O., Pearson, J. C., Kristensen, L., Yıldız, U. A., & van Dishoeck, E. F. 2011, Science, 334, 338 3.2

Holden, L., Landis, E., Spitzig, J., & Adams, F. C. 2011, PASP, 123, 14 3.3

Howard, A. W., Marcy, G. W., Bryson, S. T., Jenkins, J. M., Rowe, J. F., Batalha, N. M., Borucki, W. J., Koch, D. G., Dunham, E. W., Gautier, III, T. N., Van Cleve, J., Cochran, W. D., Latham, D. W., Lissauer, J. J., Torres, G., Brown, T. M., Gilliland, R. L., Buchhave, L. A., Caldwell, D. A., Christensen-Dalsgaard, J., Ciardi, D., Fressin, F., Haas, M. R., Howell, S. B., Kjeldsen, H., Seager, S., Rogers, L., Sasselov, D. D., Steffen, J. H., Basri, G. S., Charbonneau, D., Christiansen, J., Clarke, B., Dupree, A., Fabrycky, D. C., Fischer, D. A., Ford, E. B., Fortney, J. J., Tarter, J., Girouard, F. R., Holman, M. J., Johnson, J. A., Klaus, T. C., Machalek, P., Moorhead, A. V., Morehead, R. C., Ragozzine, D., Tenenbaum, P., Twicken, J. D., Quinn, S. N., Isaacson, H., Shporer, A., Lucas, P. W., Walkowicz, L. M., Welsh, W. F., Boss, A., Devore, E., Gould, A., Smith,

J. C., Morris, R. L., Prsa, A., Morton, T. D., Still, M., Thompson, S. E., Mullally, F., Endl, M., & MacQueen, P. J. 2012, ApJS, 201, 15 1.1.3, 4.1.1

Howard, A. W., Marcy, G. W., Johnson, J. A., Fischer, D. A., Wright, J. T., Isaacson, H., Valenti, J. A., Anderson, J., Lin, D. N. C., & Ida, S. 2010, Science, 330, 653 1.1.3, 4.1.2

Howell, S. B., Sobeck, C., Haas, M., Still, M., Barclay, T., Mullally, F., Troeltzsch, J., Aigrain, S., Bryson, S. T., Caldwell, D., Chaplin, W. J., Cochran, W. D., Huber, D., Marcy, G. W., Miglio, A., Najita, J. R., Smith, M., Twicken, J. D., & Fortney, J. J. 2014, PASP, 126, 398 4.2.2

Hughes, J., Hartigan, P., Krautter, J., & Kelemen, J. 1994, AJ, 108, 1071 2.2.1, 2.2.2

Ida, S. & Lin, D. N. C. 2004, ApJ, 604, 388 1.1.3, 4.1.1

—. 2005, ApJ, 626, 1045 4.1.2

Ikoma, M., Nakazawa, K., & Emori, H. 2000, ApJ, 537, 1013 4.1.2

Jeffries, R. D., Maxted, P. F. L., Oliveira, J. M., & Naylor, T. 2006, MNRAS, 371, L6 2.3.1, 2.3.5

Johansen, A., Blum, J., Tanaka, H., Ormel, C., Bizzarro, M., & Rickman, H. 2014, Protostars and Planets VI, 547 4.1.1

Johnson, J. A., Aller, K. M., Howard, A. W., & Crepp, J. R. 2010, PASP, 122, 905 1.1.3

Johnson, J. A., Butler, R. P., Marcy, G. W., Fischer, D. A., Vogt, S. S., Wright, J. T., & Peek, K. M. G. 2007, ApJ, 670, 833 3.1.2, 4.1.2

Johnstone, D., Hollenbach, D., & Bally, J. 1998, ApJ, 499, 758 3.3, 3.3

Jones, M. G., Pringle, J. E., & Alexander, R. D. 2012, MNRAS, 419, 925 4.2.1

Jørgensen, J. K., Schöier, F. L., & van Dishoeck, E. F. 2002, A&A, 389, 908 2.1.2

Joy, A. H. 1945, ApJ, 102, 168 2.4.1

Kama, M., Bruderer, S., Carney, M., Hogerheijde, M., van Dishoeck, E. F., Fedele, D., Baryshev, A., Boland, W., Güsten, R., Aikutalp, A., Choi, Y., Endo, A., Frieswijk, W., Karska, A., Klaassen, P., Koumpia, E., Kristensen, L., Leurini, S., Nagy, Z., Perez Beaupuits, J.-P., Risacher, C., van der Marel, N., van Kempen, T. A., van Weeren, R. J., Wyrowski, F., & Yıldız, U. A. 2016a, A&A, 588, A108 3.2

Kama, M., Bruderer, S., van Dishoeck, E. F., Hogerheijde, M., Folsom, C. P., Miotello, A., Fedele, D., Belloche, A., Güsten, R., & Wyrowski, F. 2016b, A&A, 592, A83 3.2, 4.3.2

Kelly, B. C. 2007, ApJ, 665, 1489 (document), 3.1.2, 3.2, 3.1.2, 3.1, 3.1.2, 4.2.1, 4.1

Kennedy, G. M. & Kenyon, S. J. 2008, ApJ, 673, 502 3.1.2, 4.1.2

Kenyon, S. J., Gómez, M., & Whitney, B. A. 2008, in Handbook of Star Forming Regions, Volume I (University of Arizona Press), 405 2.4.1

Kim, J. S., Clarke, C. J., Fang, M., & Facchini, S. 2016, ApJ, 826, L15 3.3

Kokubo, E., Kominami, J., & Ida, S. 2006, ApJ, 642, 1131 4.1.2

Krijt, S., Ormel, C. W., Dominik, C., & Tielens, A. G. G. M. 2016, A&A, 586, A20 3.1.2

Kurosawa, R. & Romanova, M. M. 2013, MNRAS, 431, 2673 4.2.2

Lacy, J. H., Knacke, R., Geballe, T. R., & Tokunaga, A. T. 1994, ApJ, 428, L69 3.2

Lada, C. J. 1987, in IAU Symposium, Vol. 115, Star Forming Regions, ed. M. Peimbert & J. Jugaku, 1–17 1.1.1

Lada, C. J., Muench, A. A., Luhman, K. L., Allen, L., Hartmann, L., Megeath, T., Myers, P., Fazio, G., Wood, K., Muzerolle, J., Rieke, G., Siegler, N., & Young, E. 2006, AJ, 131, 1574 1.1.1, 1.1.1

Laughlin, G., Bodenheimer, P., & Adams, F. C. 2004, ApJ, 612, L73 4.1.1

Lavalley, M., Isobe, T., & Feigelson, E. 1992, in Astronomical Society of the Pacific Conference Series, Vol. 25, Astronomical Data Analysis Software and Systems I, ed. D. M. Worrall, C. Biemesderfer, & J. Barnes, 245 (document), 3.1, 3.1.1

Lee, E. J. & Chiang, E. 2016, ApJ, 817, 90 4.1.1

Lee, N., Williams, J. P., & Cieza, L. A. 2011, ApJ, 736, 135 1.1.2

Levine, J. L., Steinhauer, A., Elston, R. J., & Lada, E. A. 2006, ApJ, 646, 1215 3.3

Loinard, L., Torres, R. M., Mioduszewski, A. J., & Rodríguez, L. F. 2008, ApJ, 675, L29 4.2.2

Luhman, K. L. 2008, Chamaeleon (Astronomical Society of the Pacific), 169 2.4.3

Luhman, K. L. & Mamajek, E. E. 2012, ApJ, 758, 31 (document), 2.4.2, 4.4, 4.2.2

Lynden-Bell, D. & Pringle, J. E. 1974, MNRAS, 168, 603 4.2.1

Mamajek, E. E. 2009, in American Institute of Physics Conference Series, Vol. 1158, American Institute of Physics Conference Series, ed. T. Usuda, M. Tamura, & M. Ishii, 3–10 1.1.1, 1.1.1

Manara, C. F., Frasca, A., Alcala, J. M., Natta, A., Stelzer, B., & Testi, L. 2017, ArXiv e-prints 2.3.2

Manara, C. F., Rosotti, G., Testi, L., Natta, A., Alcalá, J. M., Williams, J. P., Ansdell, M., Miotello, A., van der Marel, N., Tazzari, M., Carpenter, J., Guidi, G., Mathews, G. S., Oliveira, I., Prusti, T., & van Dishoeck, E. F. 2016, A&A, 591, L3 (document), 4.2.1, 4.1

Mann, R. K., Andrews, S. M., Eisner, J. A., Williams, J. P., Meyer, M. R., Di Francesco, J., Carpenter, J. M., & Johnstone, D. 2015, ApJ, 802, 77 3.3

Mann, R. K., Di Francesco, J., Johnstone, D., Andrews, S. M., Williams, J. P., Bally, J., Ricci, L., Hughes, A. M., & Matthews, B. C. 2014, ApJ, 784, 82 1.1.2, 3.3, 3.3, 3.3

Mann, R. K. & Williams, J. P. 2009, ApJ, 694, L36 1.1.2, 3

—. 2010, ApJ, 725, 430 (document), 1.3, 1.1.2

Marcy, G. W., Weiss, L. M., Petigura, E. A., Isaacson, H., Howard, A. W., & Buchhave, L. A. 2014, Proceedings of the National Academy of Science, 111, 12655 4.1.1

Marino, S., Perez, S., & Casassus, S. 2015, ApJ, 798, L44 4.2.2

Mathews, G. S., Williams, J. P., & Ménard, F. 2012a, ApJ, 753, 59 1.1.2, 4.2.2

Mathews, G. S., Williams, J. P., Ménard, F., Phillips, N., Duchêne, G., & Pinte, C. 2012b, ApJ, 745, 23 (document), 1.3, 2.1.1

Mathis, J. S., Rumpl, W., & Nordsieck, K. H. 1977, ApJ, 217, 425 2.1.1

Maucó, K., Hernández, J., Calvet, N., Ballesteros-Paredes, J., Briceño, C., McClure, M., D'Alessio, P., Anderson, K., & Ali, B. 2016, ApJ, 829, 38 3.3

Maxted, P. F. L., Jeffries, R. D., Oliveira, J. M., Naylor, T., & Jackson, R. J. 2008, MNRAS, 385, 2210 2.3.1, 2.3.5

McClure, M. K., Bergin, E. A., Cleeves, L. I., van Dishoeck, E. F., Blake, G. A., Evans, II, N. J., Green, J. D., Henning, T., Öberg, K. I., Pontoppidan, K. M., & Salyk, C. 2016, ApJ, 831, 167 2.1.2, 4.3.2

McGinnis, P. T., Alencar, S. H. P., Guimarães, M. M., Sousa, A. P., Stauffer, J., Bouvier, J., Rebull, L., Fonseca, N. N. J., Venuti, L., Hillenbrand, L., Cody, A. M., Teixeira, P. S., Aigrain, S., Favata, F., Fűrész, G., Vrba, F. J., Flaccomio, E., Turner, N. J., Gameiro, J. F., Dougados, C., Herbst, W., Morales-Calderón, M., & Micela, G. 2015, A&A, 577, A11 4.2.2, 4.2.2, 4.2.2

Merín, B., Jørgensen, J., Spezzi, L., Alcalá, J. M., Evans, II, N. J., Harvey, P. M., Prusti, T., Chapman, N., Huard, T., van Dishoeck, E. F., & Comerón, F. 2008, ApJS, 177, 551 2.2.1, 2.2.2

Miotello, A., Bruderer, S., & van Dishoeck, E. F. 2014, A&A, 572, A96 2.2.5

Miotello, A., van Dishoeck, E. F., Kama, M., & Bruderer, S. 2016, A&A, 594, A85 4.3.2

Miotello, A., van Dishoeck, E. F., Williams, J. P., Ansdell, M., Guidi, G., Hogerheijde, M.,
Manara, C. F., Tazzari, M., Testi, L., van der Marel, N., & van Terwisga, S. 2017, A&A,
599, A113 2.2.5, 2.2.5, 2.3.5

Montet, B. T., Crepp, J. R., Johnson, J. A., Howard, A. W., & Marcy, G. W. 2014, ApJ,
781, 28 4.1.1

Morales-Calderón, M., Stauffer, J. R., Hillenbrand, L. A., Gutermuth, R., Song, I., Rebull,
L. M., Plavchan, P., Carpenter, J. M., Whitney, B. A., Covey, K., Alves de Oliveira,
C., Winston, E., McCaughrean, M. J., Bouvier, J., Guieu, S., Vrba, F. J., Holtzman,
J., Marchis, F., Hora, J. L., Wasserman, L. H., Terebey, S., Megeath, T., Guinan,
E., Forbrich, J., Huélamo, N., Riviere-Marichalar, P., Barrado, D., Stapelfeldt, K.,
Hernández, J., Allen, L. E., Ardila, D. R., Bayo, A., Favata, F., James, D., Werner,
M., & Wood, K. 2011, ApJ, 733, 50 4.2.2, 4.2.2

Mordasini, C., Alibert, Y., Benz, W., Klahr, H., & Henning, T. 2012, A&A, 541, A97 1.1.3,
3.1.2, 4.1.2

Mortier, A., Oliveira, I., & van Dishoeck, E. F. 2011, MNRAS, 418, 1194 2.2.2

Mulders, G. D., Pascucci, I., & Apai, D. 2015, ApJ, 798, 112 1.1.3, 4.1.2

Murdin, P. & Penston, M. V. 1977, MNRAS, 181, 657 4.3.1

Natta, A., Grinin, V., & Mannings, V. 2000, Protostars and Planets IV, 559 1.1.3, 3, 3.1.2

Öberg, K. I. & Bergin, E. A. 2016, ApJ, 831, L19 4.3.2

Oliveira, J. M., Jeffries, R. D., Kenyon, M. J., Thompson, S. A., & Naylor, T. 2002, A&A,
382, L22 2.3.1

Oliveira, J. M., Jeffries, R. D., & van Loon, J. T. 2004, MNRAS, 347, 1327 2.3.1

Ossenkopf, V. & Henning, T. 1994, A&A, 291, 943 3.2

Pascucci, I., Testi, L., Herczeg, G. J., Long, F., Manara, C. F., Hendler, N., Mulders, G. D., Krijt, S., Ciesla, F., Henning, T., Mohanty, S., Drabek-Maunder, E., Apai, D., Szűcs, L., Sacco, G., & Olofsson, J. 2016, ApJ, 831, 125 2.1.1, 2.4.3, 3.1, 3.1.2, 3.1.2, 3.1, 3.1.2, 4.1.2

Pecaut, M. J., Mamajek, E. E., & Bubar, E. J. 2012, ApJ, 746, 154 2.4.2, 4.2.2

Petigura, E. A., Marcy, G. W., & Howard, A. W. 2013, ApJ, 770, 69 1.1.3, 4.1.1

Pollack, J. B., Hubickyj, O., Bodenheimer, P., Lissauer, J. J., Podolak, M., & Greenzweig, Y. 1996, Icarus, 124, 62 1.1.3, 4.1.1

Pontoppidan, K. M., Blake, G. A., van Dishoeck, E. F., Smette, A., Ireland, M. J., & Brown, J. 2008, ApJ, 684, 1323 4.2.2

Preibisch, T., Brown, A. G. A., Bridges, T., Guenther, E., & Zinnecker, H. 2002, AJ, 124, 404 2.4.2

Raymond, S. N., Quinn, T., & Lunine, J. I. 2005, ApJ, 632, 670 4.1.2

Ribas, Á., Bouy, H., & Merín, B. 2015, A&A, 576, A52 4.2.2

Ricci, L., Testi, L., Natta, A., Neri, R., Cabrit, S., & Herczeg, G. J. 2010, A&A, 512, A15 4.2.1

Rigliaco, E., Natta, A., Randich, S., & Sacco, G. 2009, A&A, 495, L13 3.3

Rigliaco, E., Natta, A., Randich, S., Testi, L., & Biazzo, K. 2011, A&A, 525, A47 (document), 4.2.1, 4.2

Rigliaco, E., Natta, A., Testi, L., Randich, S., Alcalà, J. M., Covino, E., & Stelzer, B. 2012, A&A, 548, A56 2.3.2

Ripple, F., Heyer, M. H., Gutermuth, R., Snell, R. L., & Brunt, C. M. 2013, MNRAS, 431, 1296 3.2

Rodigas, T. J., Follette, K. B., Weinberger, A., Close, L., & Hines, D. C. 2014, ApJ, 791, L37 4.2.2

Ros, K. & Johansen, A. 2013, A&A, 552, A137 3.2

Rosotti, G. P., Clarke, C. J., Manara, C. F., & Facchini, S. 2017, ArXiv e-prints 4.2.1

Rygl, K. L. J., Benedettini, M., Schisano, E., Elia, D., Molinari, S., Pezzuto, S., André, P., Bernard, J. P., White, G. J., Polychroni, D., Bontemps, S., Cox, N. L. J., Di Francesco, J., Facchini, A., Fallscheer, C., di Giorgio, A. M., Hennemann, M., Hill, T., Könyves, V., Minier, V., Motte, F., Nguyen-Luong, Q., Peretto, N., Pestalozzi, M., Sadavoy, S., Schneider, N., Spinoglio, L., Testi, L., & Ward-Thompson, D. 2013, A&A, 549, L1 2.2.1

Sacco, G. G., Franciosini, E., Randich, S., & Pallavicini, R. 2008, A&A, 488, 167 2.3.1, 2.3.5

Scargle, J. 1987, in Bulletin of the American Astronomical Society, Vol. 19, Bulletin of the American Astronomical Society, 829 4.2.2

Schaefer, G. H., Hummel, C. A., Gies, D. R., Zavala, R. T., Monnier, J. D., Walter, F. M., Turner, N. H., Baron, F., ten Brummelaar, T., Che, X., Farrington, C. D., Kraus, S., Sturmann, J., & Sturmann, L. 2016, AJ, 152, 213 2.3.1

Schwartz, R. D. 1977, ApJS, 35, 161 2.2.1

Schwarz, K. R., Bergin, E. A., Cleeves, L. I., Blake, G. A., Zhang, K., Öberg, K. I., van Dishoeck, E. F., & Qi, C. 2016, ApJ, 823, 91 3.2

Sherry, W. H., Walter, F. M., Wolk, S. J., & Adams, N. R. 2008, AJ, 135, 1616 2.3.1

Shimajiri, Y., Kitamura, Y., Saito, M., Momose, M., Nakamura, F., Dobashi, K., Shimoikura, T., Nishitani, H., Yamabi, A., Hara, C., Katakura, S., Tsukagoshi, T., Tanaka, T., & Kawabe, R. 2014, A&A, 564, A68 3.2

Siess, L., Dufour, E., & Forestini, M. 2000, A&A, 358, 593 2.2.2, 2.3.2, 3.1

Simón-Díaz, S., Caballero, J. A., Lorenzo, J., Maíz Apellániz, J., Schneider, F. R. N., Negueruela, I., Barbá, R. H., Dorda, R., Marco, A., Montes, D., Pellerin, A., Sanchez-Bermudez, J., Sódor, Á., & Sota, A. 2015, ApJ, 799, 169 3.3

Sinukoff, E., Howard, A. W., Petigura, E. A., Schlieder, J. E., Crossfield, I. J. M., Ciardi, D. R., Fulton, B. J., Isaacson, H., Aller, K. M., Baranec, C., Beichman, C. A., Hansen, B. M. S., Knutson, H. A., Law, N. M., Liu, M. C., Riddle, R., & Dressing, C. D. 2016, ApJ, 827, 78 1.1.3

Skrutskie, M. F., Cutri, R. M., Stiening, R., Weinberg, M. D., Schneider, S., Carpenter, J. M., Beichman, C., Capps, R., Chester, T., Elias, J., Huchra, J., Liebert, J., Lonsdale, C., Monet, D. G., Price, S., Seitzer, P., Jarrett, T., Kirkpatrick, J. D., Gizis, J. E., Howard, E., Evans, T., Fowler, J., Fullmer, L., Hurt, R., Light, R., Kopan, E. L., Marsh, K. A., McCallon, H. L., Tam, R., Van Dyk, S., & Wheelock, S. 2006, AJ, 131, 1163 4.2.2

Sternberg, A., Hoffmann, T. L., & Pauldrach, A. W. A. 2003, ApJ, 599, 1333 4.3.1

Störzer, H. & Hollenbach, D. 1999, ApJ, 515, 669 3.3, 3.3

Takami, M., Hasegawa, Y., Muto, T., Gu, P.-G., Dong, R., Karr, J. L., Hashimoto, J., Kusakabe, N., Chapillon, E., Tang, Y.-W., Itoh, Y., Carson, J., Follette, K. B., Mayama, S., Sitko, M., Janson, M., Grady, C. A., Kudo, T., Akiyama, E., Kwon, J., Takahashi, Y., Suenaga, T., Abe, L., Brandner, W., Brandt, T. D., Currie, T., Egner, S. E., Feldt, M., Guyon, O., Hayano, Y., Hayashi, M., Hayashi, S., Henning, T., Hodapp, K. W., Honda, M., Ishii, M., Iye, M., Kandori, R., Knapp, G. R., Kuzuhara, M., McElwain, M. W., Matsuo, T., Miyama, S., Morino, J.-I., Moro-Martin, A., Nishimura, T., Pyo,

T.-S., Serabyn, E., Suto, H., Suzuki, R., Takato, N., Terada, H., Thalmann, C., Tomono, D., Turner, E. L., Wisniewski, J. P., Watanabe, M., Yamada, T., Takami, H., Usuda, T., & Tamura, M. 2014, ApJ, 795, 71 4.2.2

Tazzari, M., Testi, L., Natta, A., Ansdell, M., Carpenter, J., Guidi, G., Hogerheijde, M., Manara, C. F., Miotello, A., van der Marel, N., van Dishoeck, E. F., & Williams, J. P. 2017, ArXiv e-prints 2.1.1

Thommes, E. W., Matsumura, S., & Rasio, F. A. 2008, Science, 321, 814 3.1.2

Trapman, L., Miotello, A., Kama, M., van Dishoeck, E. F., & Bruderer, S. 2017, ArXiv e-prints 3.2, 4.3.2

van der Marel, N., van Dishoeck, E. F., Bruderer, S., Pérez, L., & Isella, A. 2015, A&A, 579, A106 4.2.2

van Dishoeck, E. F. & Black, J. H. 1988, ApJ, 334, 771 2.1.2, 2.2.5

Vanderburg, A. & Johnson, J. A. 2014, PASP, 126, 948 4.2.2

Visser, R., van Dishoeck, E. F., & Black, J. H. 2009, A&A, 503, 323 2.1.2

Wahhaj, Z., Cieza, L., Koerner, D. W., Stapelfeldt, K. R., Padgett, D. L., Case, A., Keller, J. R., Merín, B., Evans, II, N. J., Harvey, P., Sargent, A., van Dishoeck, E. F., Allen, L., Blake, G., Brooke, T., Chapman, N., Mundy, L., & Myers, P. C. 2010, ApJ, 724, 835 2.2.2

Walter, F. M., Sherry, W. H., Wolk, S. J., & Adams, N. R. 2008, The σ Orionis Cluster (Astronomical Society of the Pacific), 732 2.3.1, 3.3

Weidenschilling, S. J. 1977, Ap&SS, 51, 153 2.3.4

Williams, J. P. 2012, Meteoritics and Planetary Science, 47, 1915 3

Williams, J. P., Andrews, S. M., & Wilner, D. J. 2005, ApJ, 634, 495 1.1.2

Williams, J. P. & Best, W. M. J. 2014, ApJ, 788, 59 (document), 1.1.2, 1.2, 2, 2.1.2, 2.1.2, 2.1, 2.2.5, 2.2.5, 2.4, 2.3.5, 2.11, 2.3.6, 3.2, 4.3.2

Williams, J. P. & Cieza, L. A. 2011, ARA&A, 49, 67 1.1.1, 3.2

Williams, J. P., Cieza, L. A., Andrews, S. M., Coulson, I. M., Barger, A. J., Casey, C. M., Chen, C.-C., Cowie, L. L., Koss, M., Lee, N., & Sanders, D. B. 2013, MNRAS, 435, 1671 (document), 1.3, 1.1.2, 2.1.1, 2.3.1, 2.3.3, 3, 3.1.1

Winn, J. N. & Fabrycky, D. C. 2015, ARA&A, 53, 409 1.1.3

Wright, E. L., Eisenhardt, P. R. M., Mainzer, A. K., Ressler, M. E., Cutri, R. M., Jarrett, T., Kirkpatrick, J. D., Padgett, D., McMillan, R. S., Skrutskie, M., Stanford, S. A., Cohen, M., Walker, R. G., Mather, J. C., Leisawitz, D., Gautier, III, T. N., McLean, I., Benford, D., Lonsdale, C. J., Blain, A., Mendez, B., Irace, W. R., Duval, V., Liu, F., Royer, D., Heinrichsen, I., Howard, J., Shannon, M., Kendall, M., Walsh, A. L., Larsen, M., Cardon, J. G., Schick, S., Schwalm, M., Abid, M., Fabinsky, B., Naes, L., & Tsai, C.-W. 2010, AJ, 140, 1868 4.2.2

Wyatt, M. C. 2008, ARA&A, 46, 339 2.2.6, 4.1.1, 4.2.2

Wyatt, M. C. & Dent, W. R. F. 2002, MNRAS, 334, 589 1.1.2, 2.1.1

Youdin, A. N. & Goodman, J. 2005, ApJ, 620, 459 4.1.1

Yu, M., Evans, II, N. J., Dodson-Robinson, S. E., Willacy, K., & Turner, N. J. 2017, ApJ, 841, 39 3.2

Yu, M., Willacy, K., Dodson-Robinson, S. E., Turner, N. J., & Evans, II, N. J. 2016, ApJ, 822, 53 3.2

Zhang, K., Isella, A., Carpenter, J. M., & Blake, G. A. 2014, ApJ, 791, 42 4.2.2